Study of $\nu_\mu \to \nu_\tau$ and $\nu_\mu \to \nu_{sterile}$ Neutrino Oscillations with the Atmospheric Neutrino Data in Super-Kamiokande

Kenji Ishihara

December 1999

Doctor Thesis, University of Tokyo

Abstract

A study of the atmospheric neutrino interactions was carried out using the data from a 50 kton·water Cherenkov detector, Super-Kamiokande. We observed 6982 fully-contained and 470 partially-contained events with an exposure of 52 kton year.

We studied the (μ-like/e-like) ratio of the single-ring events and compared it with a theoretcal prediction. We found that the ratio was significantly smaller than the theoretical prediction in both sub- and multi-GeV energy ranges. In addition, we studied the zenith angle distribution of these events. We found that the zenith angle distribution of e-like events were in good agreement with the theoretical prediction. On the other hand, the zenith-angle distribution of the μ-like events showed a significant deficit of the upward-going events. These data are explained by neutrino oscillation between ν_μ and ν_τ or between ν_μ and $\nu_{sterile}$, where $\nu_{sterile}$ is a new, hypothetical particle which does not interact with matter via charged current nor neutral current interactions. From these data, we estimated the allowed region of neutrino oscillation parameters, Δm^2 and $\sin^2 2\theta$. The 90% C.L. allowed region was found to be within $1.5 \times 10^{-3} < \Delta m^2 < 7 \times 10^{-3} eV^2$ and $\sin^2 2\theta > 0.83$ for both hypothesis. These observations reconfirmed, with a higher statistics, the atmospheric neutrino oscillation reported by the same experiment in 1998.

We have also studied partially-contained events and fully-contained multi-ring events. These events were used to distinguish the $\nu_\mu \to \nu_\tau$ and $\nu_\mu \to \nu_{sterile}$ oscillations. In the case of $\nu_\mu \to \nu_{sterile}$ oscillation, matter effect must be taken into account in the neutrino oscillation analysis. Since the matter effect suppress the oscillation for high energy neutrinos, zenith angle distribution of the partially-contained events was studied to distinguish the two neutrino oscillation modes. Fully-contained multi-ring events contain a large number of neutral current events. Since $\nu_{sterile}$ does not interact with matter, we should observe a deficit of upward-going neutral current events for $\nu_\mu \to \nu_{sterile}$ oscillation. The $Up/Down$ ratios of these two data sets and the corresponding predictions based on the $\nu_\mu \to \nu_\tau$ hypothesis agreed. On the other hand, the predictions based on the

$\nu_\mu \to \nu_{sterile}$ hypothesis had poorer agreements with the data. By combining studies of partially-contained events and fully-contained multi-ring events, we concluded that the $\nu_\mu \to \nu_{sterile}$ oscillation hypothesis as the solution of the atmospheric neutrino oscillation was disfavored at 99% C.L. for most of the region indicated by the fully-contained single-ring analysis. We also found that this conclusion was supported by the upward-going muon data.

Acknowledgments

First of all, I would like to express my great appreciation to my advisor, Prof. T.Kajita. He gave me the chance to participate in this great experiment from the first stage of the analysis on the atmospheric neutrino. He introduced me to high energy physics, and supported me during graduate studies. His excellent guidance and continues encouragement were very valuable to me.

I would like to be thankful to Prof. Y.Totsuka, the spokesman of the Super-Kamiokande experiment, Prof. K.Nakamura, Prof Y.Suzuki and Prof. M.Nakahata. They gave me many valuable advice about my work on various occasions.

I am grateful specially to the members of the atmospheric neutrino and proton decay analysis group. T.Hayakawa taught me the art of the physics from the basics. Dr. K.Okumura gave me many support for my work. I am indebted to Dr. Y.Itow, Dr. M.Miura, M.Shiozawa, Dr. Y.Obayashi, Dr. S.Kasuga, J.Kameda, K.Kobayashi from ICRR, Dr. K.Kaneyuki, Dr. Y.Hayato, Y.Kanaya, T.Futagami from TIT, K.Fujita and M.Etoh from Tohoku University, and the members in USA, especially, Dr. Ed. Kearns, Dr. C. Walter, Dr. K.Scholberg, Dr. M. Messier, M. Earl, Dr. C. McGrew, C. Mauger, B. Viren, Dr. D. Casper, T. Barszczak, Dr. L. Wai, Dr. J.George, and A. Kibayashi.

I should also thank the Upward-going muon analysis group, Dr. M.Takita, K.Nitta. They gave me the chance to analyze the upward-going muon data.

I am thankful to all the collaborators of Super-Kamiokande for very useful suggestions. Especially, Dr. K.Inoue, Dr. Y.Fukuda, Dr. Y.Takeuchi, Dr. Y.Koshio, Dr. H.Ishino, M.Oketa, M.Ohta, N.Sakurai, S.Nakayama, S.Yamada, U.Kobayashi and T.Takeuchi, who are all members of ICRR at Kamioka and with whom I often had useful discussions about the experiment, physics and so on.

Finally, I gratefully acknowledge the cooperation of Kamioka Mining and Smelting Company and financial support of the Japan Society of the Promotion of Science.

Contents

Chapter 1

Introduction

Since its first postulation in 1930 by Pauli [1], the neutrino has played a crucial role in the understanding of particle physics. The existence of the neutrino was confirmed in 1956 by Reines and Cowan [2] detecting anti-neutrinos from a nuclear power reactor by the reaction, $\overline{\nu}+p \rightarrow e^{+}+n$. In this experiment, anti-electron-neutrinos were detected. Then, in 1962, the muon-neutrino was observed [3] by an accelerator experiment via $\nu_{\mu}N \rightarrow \mu N'$, where N and N' are nucleons.

Another important step was taken by Lee and Yang who proposed parity violation in beta decay [4]. Parity violation was discovered by measurements of the angular distributions of beta-decay electrons from polarized ^{60}Co atoms by Wu *et al.* [5]. It was recognized that parity violation in weak interactions could be explained by a vanishing neutrino mass.

From these developments, it became natural to consider a theory of two component neutrino in which the neutrino was exactly massless. The massless neutrino was one of the key features of the present "Standard Model"[6, 7, 8] of particle physics.

However, there is no fundamental reason that the neutrino must be exactly massless. Indeed, the smallness of the neutrino mass was naturally explained by the seesaw mechanism [9, 10]. Experimentally, there were lots of works to detect the small neutrino mass. Last year, the evidence for neutrino mass was reported by the observation of atmospheric neutrinos in a 50 kton water Cherenkov detector, Super-Kamiokande [11].

1.1 Atmospheric neutrino

Atmospheric neutrinos are the decay products of mesons produced from the collisions between primary cosmic-rays (mainly protons and α-particles) and nuclei (mainly nitrogen and oxygen) in the atmosphere.

They are composed of $\overset{(-)}{\nu}_\mu$ and $\overset{(-)}{\nu}_e$, and originate principally from the following decays:

- $\overset{(-)}{\nu}_\mu$ from
  - $\pi^\pm \to \mu^\pm \overset{(-)}{\nu}_\mu$
  - $\mathrm{K}^\pm \to \mu^\pm \overset{(-)}{\nu}_\mu$
  - $\mathrm{K}^0_L \to \pi^\mp \mu^\pm \overset{(-)}{\nu}_\mu$
  - $\mu^\pm \to e^\pm \overset{(-)}{\nu}_\mu \overset{(-)}{\nu}_e$
- $\overset{(-)}{\nu}_e$ from
  - $\mathrm{K}^0_L \to \pi^\mp e^\pm \overset{(-)}{\nu}_e$
  - $\mu^\pm \to e^\pm \overset{(-)}{\nu}_\mu \overset{(-)}{\nu}_e$

Figure 1.1 shows a compilation of the cosmic ray spectra by Webber and Leziak [12] for hydrogen, helium, and CNO nuclei. Based on this primary cosmic ray fluxes, Honda *et al.* [13] calculated the atmospheric neutrino flux. The spectrum of the atmospheric neutrino is approximately proportional to $E^{-\gamma}$ at multi-GeV region; γ is about 3.0 and 3.5 for ν_μ and ν_e, respectively. Figure 1.2 shows the energy distribution of the expected atmospheric neutrino fluxes.

The uncertainty in the absolute flux of the atmospheric neutrino is estimated to be $\sim 30\%$ due to the uncertainty in the absolute flux of the primary cosmic-rays and the cross sections in the collision. However, $(\nu_\mu + \bar{\nu_\mu})/(\nu_e + \bar{\nu_e})$ ratio can be calculated with the uncertainty of less than 5 % over a broad range of energies from 0.1 GeV to 10 GeV [13, 14], because the production of ν_μ and ν_e is dominated by the pion decay chain at this energy range.

Figure 1.3 shows the expected atmospheric neutrino flavor ratios calculated by two independent groups. Figure 1.3 (a) demonstrates the uncertainty of $(\nu_\mu + \bar{\nu_\mu})/(\nu_e + \bar{\nu_e})$ prediction is small at $E_\nu \lesssim 30GeV$.

Moreover the zenith angle distribution of the atmospheric neutrino fluxes play very important role in this thesis. Since the primary cosmic ray particles enter into the Earth isotropically, the atmospheric neutrino fluxes are expected to be up-down symmetric. Figure 1.4 shows the calculated zenith angle distributions. Actually, the geo-magnetic

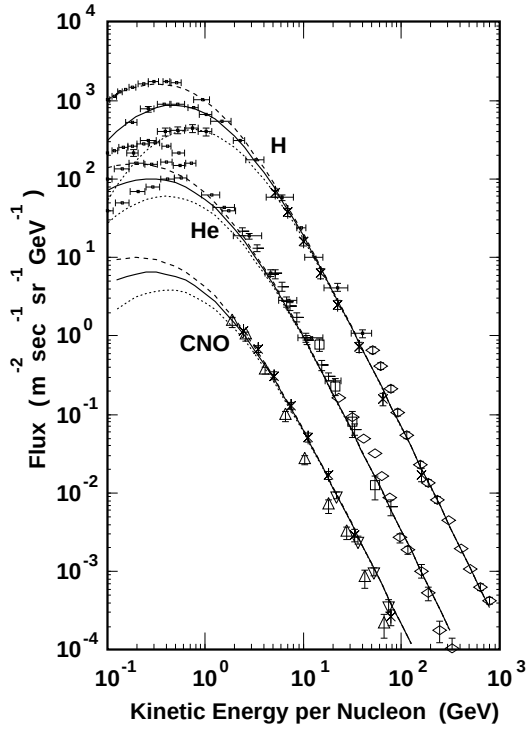

Figure 1.1: Observed primary cosmic ray fluxes [12]. The solid lines show a parameterization for solar mid, the dash lines for solar min, and the dotted lines for solar max.

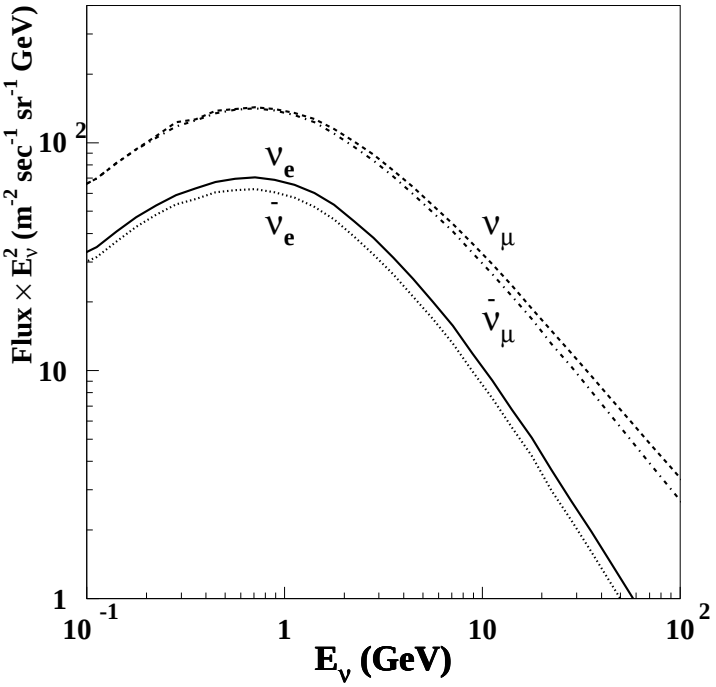

Figure 1.2: Expected atmospheric neutrino fluxes at the Kamioka site [13]. These fluxes are calculated for the mean solar activity.

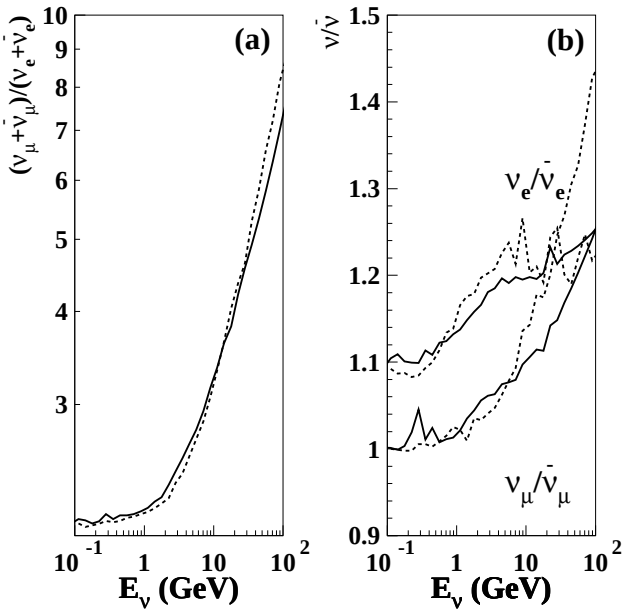

Figure 1.3: Expected atmospheric neutrino flavor ratios. (a) shows $(\nu_\mu + \bar{\nu_\mu})/(\nu_e + \bar{\nu_e})$; (b) shows $\nu_e/\bar{\nu_e}$ and $\nu_\mu/\bar{\nu_\mu}$. The solid (broken) line shows the prediction by Honda *et al*[13] (Bartol [14]).

field effect breaks this symmetry at low E_ν region. However this asymmetry decreases with increasing E_ν, and is negligible at $E_\nu > 5GeV$.

1.2 Observation of the atmospheric neutrinos

In the 1980's, massive underground experiments started to search for nucleon decay. These experiments were able to detect the atmospheric neutrinos, but the study on the atmospheric neutrino was carried out only to estimate a background to the nucleon decay search.

However, the Kamiokande experiment [15, 16, 17, 18, 19], which was the immediate predecessor to the Super-Kamiokande detector, carefully studied them, and consequently discovered the existence of the so-called "atmospheric neutrino anomaly". In 1988, the group reported that the observed μ/e ratio, which is expected to be $\sim$2 at $E_\nu \sim 1GeV$ with 5 % uncertainty, was close to one. This report made the study of the atmospheric neutrinos be an important measurement on its own, and motivated other underground experiments to study the atmospheric neutrinos carefully.

The observed μ/e ratios were reported as $R \equiv (\mu/e)_{data}/(\mu/e)_{MC}$, where μ and e are the number of muon like (μ-like) and electron like (e-like) events observed in the detector for both real data and Monte Carlo simulation. If the observed value of $(\nu_\mu+\bar{\nu_\mu})/(\nu_e+\bar{\nu_e})$ is

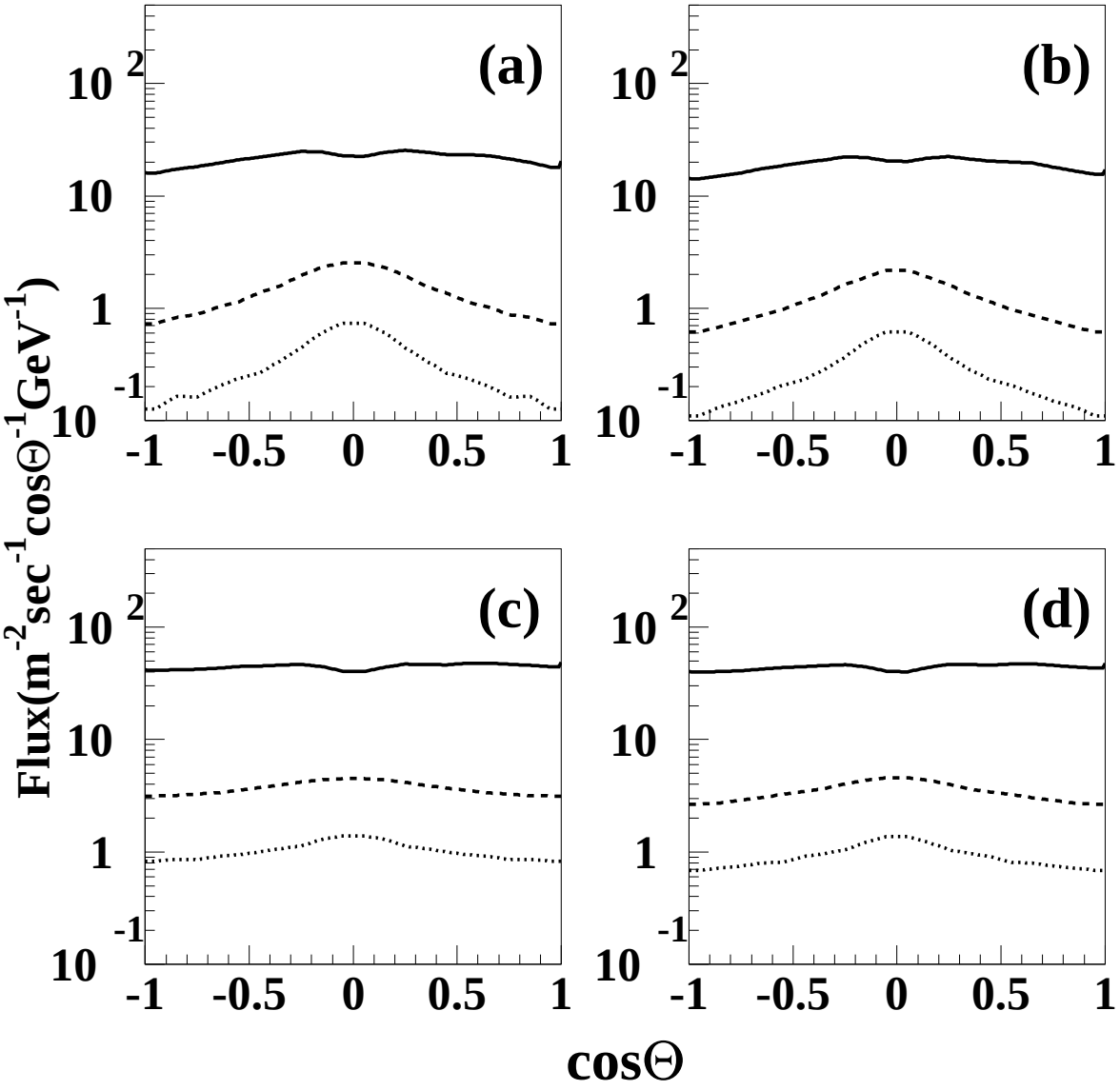

Figure 1.4: Expected zenith angle distributions of the atmospheric neutrino fluxes [13]; (a) for ν_e, (b) for $\bar{\nu_e}$, (c) for ν_μ, and (d) for $\bar{\nu_\mu}$. The solid, broken, and dashed lines are for $E_\nu = 1, 5$, and $10GeV$, respectively.

consistent with the Monte Carlo prediction, R should be unity. Table 1.1 summarizes the atmospheric neutrino measurements. The R obtained by the water Cherenkov detectors, Kamiokande and IMB(Sub-GeV), were significantly smaller than unity, and indicated the existence of the atmospheric neutrino anomaly. On the other hand, Nusex and Frejus, which were iron calorimeter detectors, reported that their results were in agreement with the Monte Carlo prediction. Therefore the atmospheric neutrino anomaly was sometimes supposed to be a particular problem to the water Cherenkov detectors. However, the other iron calorimeter, Soudan II, observed small R and showed the anomaly was not the issue due to the water Cherenkov detectors. The results of these experiments had large spread in the central values and relatively large uncertainties, so that the more precise experiments were required to confirm the existence of the atmospheric neutrino anomaly and to find out what is the solution of this anomaly. Therefore we constructed 50 kton water Cherenkov detector, Super-Kamiokande, which enables us to carry out a high-statistics atmospheric neutrino measurement.

Experiment		R
Kamiokande(*)	sub-GeV [18]	$0.60\ ^{+0.07}_{-0.06}\ \pm 0.05$
	multi-GeV [18]	$0.57\ ^{+0.08}_{-0.07}\ \pm 0.07$
IMB	sub-GeV [20]	$0.54 \pm 0.05 \pm 0.12$
	multi-GeV [21]	$1.4\ ^{+0.4}_{-0.3}\ \pm 0.3$
Soudan II [22]		$0.72 \pm 0.19 \pm 0.06$
Nusex [23]		$0.99\ ^{+0.35}_{-0.25}$
Frejus [24]		$1.00 \pm 0.15 \pm 0.08$

Table 1.1: Summary of the obtained $R \equiv= (\mu/e)_{data}/(\mu/e)_{MC}$ from the experiments before Super-Kamiokande. (*) sub-GeV (multi-GeV) indicates $E_{vis} < 1.33GeV (E_{vis} > 1.33GeV)$, where E_{vis} is the energy of an electron that would produce the observed amount of Cherenkov light.

Recently, the Super-Kamiokande experiment reported the results based on 33 kton-

year's atmospheric neutrino data [11]:

$$R = \begin{cases} 0.63 \pm 0.03_{(stat.)} \pm 0.05_{(sys.)} & sub-GeV \\ 0.65 \pm 0.05_{(stat.)} \pm 0.08_{(sys.)} & multi-GeV \end{cases} \tag{1.1}$$

Both R were significantly smaller than unity by more than 4 standard deviations. These results were consistent with that of the Kamiokande and IMB(sub-GeV), and confirmed the atmospheric neutrino anomaly.

The other important report[11, 25] from the Super-Kamiokande experiment was on the zenith angle distribution of the atmospheric neutrinos. As mentioned, the zenith angle distributions of the atmospheric neutrino fluxes should be $Up/Down$ symmetric at multi GeV region. In contract to this, the observed $Up/Down$ ratios by the Super-Kamiokande were:

$$Up/Down = \begin{cases} 0.93 \ {}^{+\,0.13}_{-\,0.12} \ {}_{(stat.)} \pm 0.02_{(sys.)} & e-like \\ 0.54 \ {}^{+\,0.06}_{-\,0.05} \ {}_{(stat.)} \pm 0.01_{(sys.)} & \mu-like \end{cases}$$

The deviation of $Up/Down$ for μ-like events from unity was 6 σ, whereas that for e-like was consistent with the expected one. This means that the zenith angle anomaly is particular to μ-like events, and it is too large to be explained by a statistical fluctuation.

1.3 Neutrino Oscillation

Atmospheric neutrino data from Kamiokande and Super-Kamiokande can be explained by neutrino oscillations [26, 27]. In the standard model, neutrinos were regarded to be zero mass particles. However, if neutrinos have nonzero mass, then the eigenstates of the mass can be different from the ones of the week interactions flavor eigenstate. As a result, neutrinos oscillate among different neutrino flavors. This phenomenon is called as 'neutrino oscillations'. In the case of $\nu_\alpha \to \nu_\beta$ neutrino oscillations, the flavor eigenstates are expressed as combinations of mass eigenstates ν_1, ν_2 as follows:

$$\begin{pmatrix} \nu_\alpha \\ \nu_\beta \end{pmatrix} = \begin{pmatrix} \cos\theta & \sin\theta \\ -\sin\theta & \cos\theta \end{pmatrix} \begin{pmatrix} \nu_1 \\ \nu_2 \end{pmatrix} \equiv U \begin{pmatrix} \nu_1 \\ \nu_2 \end{pmatrix} \tag{1.2}$$

with θ being the mixing angle.

The states ν_α and ν_β are produced in a weak decay process. However their propagation in space-time are determined by the characteristic frequencies of the mass eigenstates:

$$\begin{aligned} \nu_1(t) &= \nu_1(0)e^{-iE_1 t}, \\ \nu_2(t) &= \nu_2(0)e^{-iE_2 t} \end{aligned} \tag{1.3}$$

Since momentum is conversed, the states $\nu_1(t)$ and $\nu_2(t)$ must have the same momentum p. As a result, if the mass $m_i \ll p$(i=1,2):

$$E_i = p + \frac{m_i^2}{2p} \tag{1.4}$$

Thus, the from Eq. 1.2 and 1.3 we find:

$$\begin{pmatrix} \nu_\alpha(t) \\ \nu_\beta(t) \end{pmatrix} = U \begin{pmatrix} e^{-iE_1 t} & 0 \\ 0 & e^{-iE_2 t} \end{pmatrix} U^{-1} \begin{pmatrix} \nu_\alpha(0) \\ \nu_\beta(0) \end{pmatrix} \tag{1.5}$$

Suppose we start at $t = 0$ with $\nu_\alpha(0) = 1$, $\nu_\beta(0) = 0$, the surviving probability of ν_α at time=t, $\nu_\alpha(t)$, is calculated as follows:

$$P(\nu_\alpha \to \nu_\alpha) = 1 - \sin^2 2\theta \sin^2 \left(\frac{(E_2 - E_1)t}{2} \right) \tag{1.6}$$

From 1.4, this equation is rewritten as:

$$P(\nu_\alpha \to \nu_\alpha) = 1 - \sin^2 2\theta \sin^2 \left(\frac{\Delta m^2 L}{4p} \right) \tag{1.7}$$

$$= 1 - \sin^2 2\theta \sin^2 \left(\pi \frac{L}{l_v} \right) \tag{1.8}$$

where l_v is the oscillation length, which is $4\pi p/\Delta m^2$, $\Delta m^2 = m_2^2 - m_1^2$, and L is the distance from the source.

Neutrino oscillation experiments Neutrino oscillation is tested by using the atmospheric, the solar, the reactor, and accelerator neutrinos. The Super-Kamiokande experiment obtained the allowed region Δm^2 v.s. $\sin^2 2\theta$ for $\nu_\mu \to \nu_\tau$ oscillation based on the atmospheric neutrino data [11]. Figure 1.5 illustrates the allowed region of $(\sin^2 2\theta, \Delta m^2)$

	Δm^2	$\sin^2 2\theta$
MSW (large angle solution)	$\sim 0.9 \times 10^{-5}$	~ 0.6
MSW (small angle solution)	$\sim 0.6 \times 10^{-5}$	$\sim 7 \times 10^{-3}$
MSW (low Δm^2 solution)	$\sim 0.7 \times 10^{-7}$	~ 0.8
vacuum oscillation	$\sim 10^{-10}$	~ 0.9

Table 1.2: The allowed region from the solar neutrino observation; Homestake [32], GALLEX [33], SAGE [34], and Super-Kamiokande [35].

obtained by the Super-Kamiokande experiment. This figure concluded that the atmospheric neutrino data were in good agreement with $\nu_\mu \to \nu_\tau$ oscillation with $\sin^2\theta > 0.82$ and $5 \times 10^{-4} < \Delta m^2 < 6 \times 10^{-3} eV^2$ at 90% confidence level.

Also the results from the Chooz experiment [28] put stringent limits on $\nu_\mu \to \nu_e$ mixing in the interest region of Δm^2. Therefore the hypothesis of $\nu_\mu \to \nu_e$ oscillations as an explanation of the atmospheric neutrino data is disfavored.

Besides the atmospheric neutrino, the Super Kamiokande experiment observes the solar neutrino. Additional signals of neutrino oscillations [1] arise from solar neutrino data. This result is summarized in Table 1.2.

1.4 Matter effect

When neutrinos propagate in matter, they acquire additional potential energy from their forward scattering amplitude. This effect was first pointed out by Wolfenstein [36](see also [37, 38]). In the presence of matter with constant density, we solve the following equation to obtain the time evolution of neutrino:

$$i\frac{d}{dt}\begin{pmatrix}\nu_\alpha\\ \nu_\beta\end{pmatrix} = \left[U\begin{pmatrix}E_1 & 0\\ 0 & E_2\end{pmatrix}U^{-1} + \begin{pmatrix}V_\alpha & 0\\ 0 & V_\beta\end{pmatrix}\right]\begin{pmatrix}\nu_\alpha\\ \nu_\beta\end{pmatrix} \tag{1.9}$$

[1] LSND [29, 30] reported they found the evidence of the $\bar{\nu_\mu} \to \bar{\nu_e}$ oscillations. Their result suggests the parameter range is $\Delta m^2 \sim 1 eV^2$ and $\sin^2 2\theta \sim 10^{-2}$. But KARMEN [31], which is the same type experiment as LSND, cannot confirm it. Hence I do not use the LSND result in this thesis.

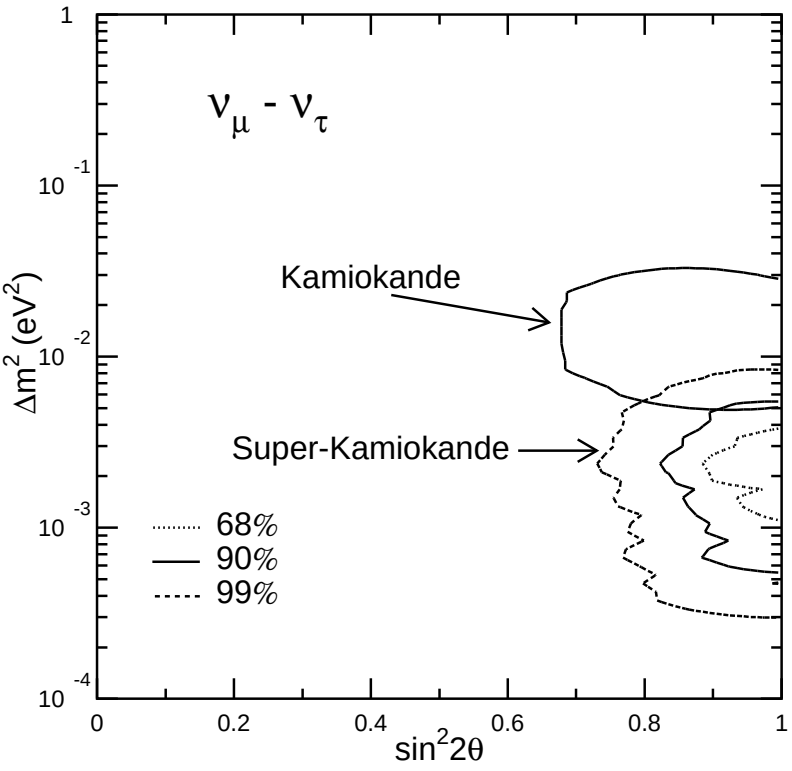

Figure 1.5: The allowed neutrino oscillation parameter regions obtained by Kamiokande and Super Kamiokande [11]. This analysis is based on the observation of the atmospheric neutrinos.

We can solve this equation to obtain the effective mixing angle θ_m and the oscillation length l_m as follows:

$$\begin{aligned} \sin^2 2\theta_m &= \frac{\sin^2 2\theta}{[\zeta - \cos 2\theta]^2 + \sin^2 2\theta}, \\ l_m &= \frac{l_v}{\sqrt{[\zeta - \cos 2\theta]^2 + \sin^2 2\theta}} \end{aligned} \tag{1.10}$$

where

$$\zeta = \frac{2p(V_\alpha - V_\beta)}{\Delta m^2}$$

The potential of ν_α, V_α, is given by

$$V_\alpha = \sqrt{2} G_F n_\gamma \left(L^{(\alpha)} - \frac{A_\alpha T^2}{M_W^2} \right) \tag{1.11}$$

where G_F is the Fermi coupling constant; M_W is the W boson mass; T is a temperature; n_γ is a number density of photons; and A_α is a numerical factor given by $A_e \sim 55$ and $A_{\mu,\tau} \sim 15.3$ [39, 40]. The quantity $L^{(\alpha)}$ is given by

$$L^{(\alpha)} = L_{\nu_\alpha} + L_{\nu_e} + L_{\nu_\mu} + L_{\nu_\tau} + \left(\pm \frac{1}{2} + 2\sin^2\theta_W \right) L_e + \left(\frac{1}{2} - 2\sin^2\theta_W \right) L_p - \frac{1}{2} L_n \tag{1.12}$$

where the plus sign refers to $\alpha = e$ and the minus sign refers to $\alpha = \mu, \tau$. Also $L_\alpha \equiv (n_\alpha - n_{\bar{\alpha}})/n_\gamma$ where n is the number densities. For anti-neutrinos, one must replace $L^{(\alpha)}$ by $-L^{(\alpha)}$ in Eq. 1.11.

Matter effect in the Earth From the above discussion, it is clear that the matter has no effect in the case of $\nu_\mu \to \nu_\tau$ oscillation. However, if we assume the neutrino oscillation between ν_μ and a non-interacting sterile neutrino, ν_s, the matter effect must be taken in account. When the $\nu_\mu \to \nu_s$ oscillation occurs in the Earth, $L^{(\mu)}$ is $-\frac{1}{2}L_n$, because the density of neutrinos is negligible and the density of electrons and protons is identical. And the term related to T in Eq. 1.11 is negligible at the normal temperature $T \sim 300K$. Therefore the effective potential for the $\nu_\mu \to \nu_s$ oscillation is given by:

$$V_{\mu s} \equiv V_\mu - V_s = -\frac{\sqrt{2}}{2} G_F n_n = -9.5 \times 10^{-5} \frac{\rho}{\rho_\circ} \left[\frac{eV^2}{GeV} \right] \tag{1.13}$$

where ρ is the mass density, $\rho_\circ = 5g \cdot cm^{-3}$ is the average mass density in the Earth. Here the neutron fraction is assumed to be 0.5. For the anti-neutrino, the sign of potential changes to plus. For $|\zeta \ll 1|$ (corresponding to low neutrino energies), the matter effect is negligible and the behavior of the $\nu_\mu \to \nu_s$ neutrino oscillation is same as the vacuum oscillation. For $|\zeta \gg 1|$ (high neutrino energies), the effective mixing angle and oscillation length becomes:

$$\begin{aligned} \sin^2 2\theta_m &\to \frac{(\Delta m^2)^2}{4p^2 V_{\mu s}^2} \sin^2 2\theta \\ l_m &\to \frac{2\pi}{V_{\mu s}} \sim 1.3 \times 10^4 \frac{\rho_\circ}{\rho}\ km \end{aligned} \tag{1.14}$$

The oscillation length for the high momentum neutrino is independent of E or Δm^2, and closes to be the diameter of the Earth. The survival probability of ν_μ at the high energy limit is:

$$P_m(\nu_\mu \to \nu_\mu) \to 1 - \frac{(\Delta m^2)^2}{4p^2 V_{\mu s}^2} \sin^2 2\theta \sin^2 \left(\frac{V_{\mu s} L}{2} \right) \tag{1.15}$$

In the case of short L compared to the Earth's diameter, P_m becomes $1 - \frac{(\Delta m^2)^2 L^2}{16p^4} \sin^2 2\theta$, which is the same as P in vacuum oscillation at high momentum limit. For $|\zeta| \sim 1$, the matter effect is strongly enhanced. This condition is rewritten as:

$$E_{msw} \equiv \frac{\Delta m^2}{2V_{\mu s}} = 2.4 \left(\frac{\Delta m^2}{\Delta m^2_{atm}} \right) \left(\frac{\rho_\circ}{\rho} \right) [GeV] \tag{1.16}$$

where $\Delta m^2_{atm} = 2.2 \times 10^{-3} eV^2$ is the best fit value for $\nu_\mu \to \nu_\tau$ oscillation obtained by the Super Kamiokande experiment [11]. In the case of $\Delta m^2 > 0$, the $\bar{\nu_\mu} \to \bar{\nu_s}$ oscillation is enhanced around E_{msw}, and the $\nu_\mu \to \nu_s$ oscillation is suppressed at the same energy region. For $\Delta m^2 < 0$, on the contrary, $\nu_\mu \to \nu_s$ ($\bar{\nu_\mu} \to \bar{\nu_s}$) is enhanced (suppressed). This is because of the difference of sign of $V_{\mu s}$. Figure 1.4 shows the survival probability of neutrino with energy $E = 5$, 10, and 20 GeV in the case of $\Delta m^2 = 2.2 \times 10^{-3}$ and $\sin^2 2\theta = 0.7$ and 1. Figure 1.7 shows the mass density distribution of the Earth used in this thesis [41].

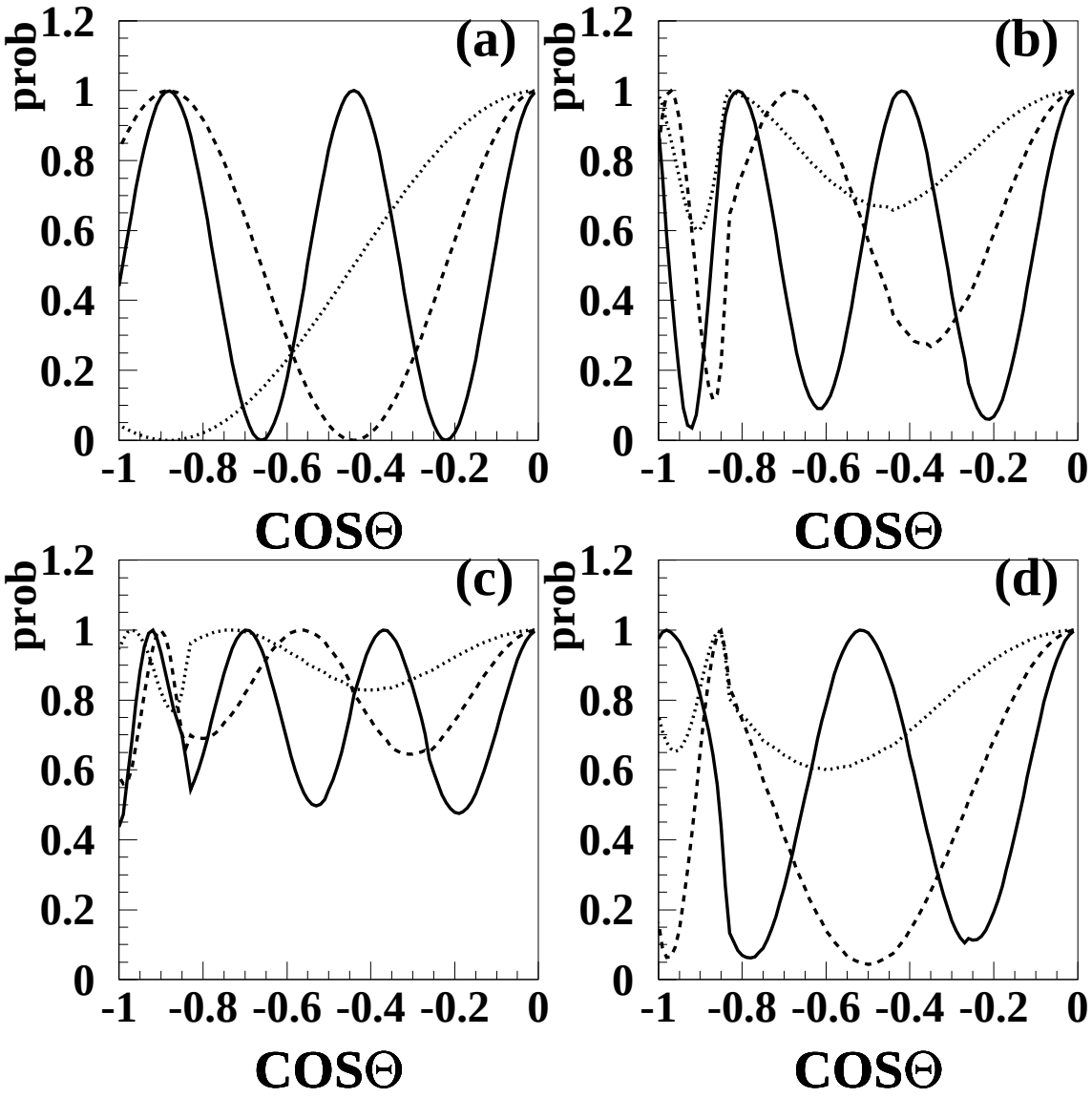

Figure 1.6: Survival probability of ν_μ as a function of zenith angle, $\cos\Theta$. Δm^2 is set to be $2.2 \times 10^{-3} eV^2$, which is the best-fit parameter obtained by Super-Kamiokande [11]. Solid line: $E_\nu = 5GeV$: Broken line: $E_\nu = 10GeV$: Dashed line $E_\nu = 20GeV$ (a) for $\nu_\mu \to \nu_\tau$ with $\sin^2 2\theta = 1.0$ (b) for $\nu_\mu \to \nu_s$ with $\sin^2 2\theta = 1.0$ (c) for $\nu_\mu \to \nu_s$ with $\sin^2 2\theta = 0.7$ (d) for $\bar{\nu_\mu} \to \bar{\nu_s}$ with $\sin^2 2\theta = 0.7$ The structure of $\nu_\mu \to \nu_s$ at $\cos\Theta \sim -0.8$ is caused by the core of the Earth.

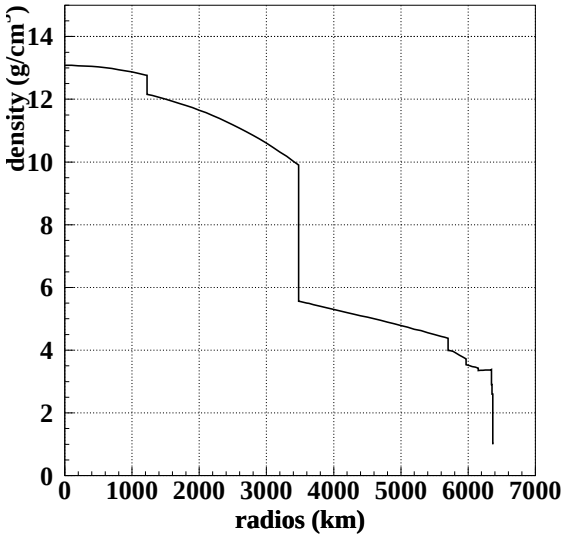

Figure 1.7: Mass density distribution in the Earth as a function of the radius of the Earth [41].

1.5 Sterile neutrino

In this section, we describe the "sterile" neutrino mentioned in the previous section. ν_s is requested to explain the atmospheric neutrino anomaly, and at the same time, to interpret neutrinos as the candidate of hot dark matter.

1.5.1 Indication of the Hot dark matter model

Another interesting subject related to the massive neutrino physics is the hot dark matter. Neutrinos are the most natural candidates of the hot dark matter, because they are solitary particles whose existence have been confirmed. In the standard big bang model, the contribution of the massive neutrinos to the energy density is given by [42]

$$\Omega_{neutrino} = \frac{\sum_i m_{\nu_i}}{92 h^2 eV} \tag{1.17}$$

where $h \sim 0.7$ is the Hubble constant in units of $100km \cdot s^{-1} \cdot Mpc^{-1}$. It was reported that a hot+cold dark matter mixture with $\Omega_{neutrinos} \sim 0.20 - 0.25$ can explain the structure formation [43]. This corresponds to 3 $eV \lesssim m_{\nu_\tau} \lesssim 7$ eV [2], if ν_τ has the heaviest mass among all flavors of neutrino, and neutrinos have the large mass difference in the

[2]Recent results from CHORUS [44] and NOMAD [45] excluded the $\nu_\mu \to \nu_\tau$ oscillation with parameter region $\Delta m^2 \gtrsim 1eV^2$ and $\sin^2 2\theta \sim 1$. However if the mixing angle among ν_μ and ν_τ is less than 10^{-4}, the experimental results are compatible with this assumption.

same way as the charged leptons. However this assumption is not compatible with the observations of the atmospheric and solar neutrinos. Figure 1.5 proves $M_{\nu_\tau} \sim 5 \times 10^{-2} eV$, that contradicts with Eq. 1.17. Accordingly, another neutrino to solve this question is introduced into the frame of neutrino oscillation. The new neutrinos should not interact with matter via weak current, because the number of active neutrinos with $M_\nu < M_{z^\circ}/2$ are proved to be 3 by experiments at LEP and SLAC [46]. Therefore this new neutrino is called "sterile" neutrino.

1.5.2 Constraints for sterile neutrino

Bounds on the existence of sterile states with large mixing to the standard neutrinos have been obtained from cosmological considerations. For large enough values of the mixing angle and Δm^2, the oscillations of standard neutrinos into sterile ones can bring the sterile states into the thermal equilibrium with matters before the nucleosynthesis epoch. The increase in the energy density results in the overproduction of primordial helium, spoiling the success of Big Bang Nucleosynthesis. Schramm and Turner [47] have estimated the upper limit (95 % C.L.) on the number of light degrees of freedom at nucleosynthesis as $N_\nu \leq 3.6$. This bound, according to the analyses in [48, 49, 50, 51, 52, 53, 54], is incompatible with the explanation of the atmospheric neutrino problem due to the mixing between muon and sterile neutrinos, because the allowed region in the oscillation parameter space would result in $N_\nu \simeq 4$.

However a recent work [55] has shown that this cosmological bound can be evaded, considering the suppression of oscillations due to the possible presence of a lepton asymmetry in the early universe that can be generated by the oscillations themselves.

1.5.3 Pseudo-Dirac neutrinos model

Here we introduce a scenario, "pseudo-Dirac neutrinos model"[56], which predicts "sterile" neutrino. This model can lead to the maximum mixing of $\nu_\mu \rightarrow \nu_s$ oscillation by installing the "right-handed" neutrinos and the light "Majonara mass". The result from Super-Kamiokande [11] proves neutrinos to be massive particles. It indicates the evidence of the "right-handed" neutrinos, because it is natural that the neutrino mass is derived from the

coupling of the "left-handed" and the "right-handed" ones. Moreover neutrinos can have the Majonara mass term, because they are neutral particles. Therefore a prerequisite for the "pseudo-Dirac neutrinos model" is naturally introduced from the neutrino oscillation.

This model interprets ν_s as the "right-handed" neutrino, which dose not interact with matter via weak interaction. The $\nu_\mu \to \nu_s$ oscillation is thought to be $\nu_{\mu L} \to \bar{\nu_{\mu}}_L$. The reason why ν_s is not $\nu_{\mu R}$ but $\bar{\nu_{\mu L}}$ is that $\nu_\mu \to \nu_s$ oscillation must conserve the angular momentum.

Generally, the neutrino mass term (Dirac-Majonara mass term) can be added to the standard model Lagrangian without special modifications. For one neutrino generation, neutrino mass eigenstates are expressed as:

$$m_{1,2} = \frac{\sqrt{4m_D^2 + (m_L - m_R)^2} \pm (m_L + m_R)}{2} \tag{1.18}$$

where m_D is the Dirac mass, and m_L, m_R are the left and the right handed Majonara masses. The mixing angle between the two states corresponding to the above mass eigenstate is:

$$\tan 2\theta = \frac{2m_D}{m_R - m_L} \tag{1.19}$$

The "pseudo-Dirac neutrino model" assumes $m_R = m_L = \delta m \ll m_D$, so that Eq. 1.18 can be rewritten as

$$m_{1,2} = m_D \pm \delta m \tag{1.20}$$

Therefore,

$$\Delta m^2 = 4\delta m \cdot m_D \tag{1.21}$$

in this scenario. Also the right term in Eq. 1.19 goes to infinity, which means $\sin^2 2\theta = 1$. The maximum mixing of $\nu_\mu \to \nu_s$ are conducted.

1.6 Difference between $\nu_\mu \to \nu_\tau$ and $\nu_\mu \to \nu_s$ in Super Kamiokande

As mentioned in Sec. 1.5, the existence of ν_s affects astrophysics like the big bang nucleosynthesis and the hot+cold dark matter scenario. Thus, it is interesting to distinguish

between $\nu_\mu \to \nu_\tau$ and $\nu_\mu \to \nu_s$ oscillation for the solution of the atmospheric neutrino oscillation. There are two samples to distinguish $\nu_\mu \to \nu_\tau$ from $\nu_\mu \to \nu_s$ at Super Kamiokande. In this thesis, the study of $\nu_\mu \to \nu_\tau$ and $\nu_\mu \to \nu_s$ in Super-Kamiokande is presented by using the following two samples.

1.6.1 Neutral current sample

Tau neutrinos interact with a nucleon via neutral current in the same way as muon neutrino, but by definition sterile neutrinos do not. Therefore, if $\nu_\mu \to \nu_s$ oscillation is the solution of the atmospheric neutrino oscillation, we can find a deficit of neutral current events. At present, one of the promising possibility to identify the neutral current effect is to study the reaction of one neutral pion production [57]: $\nu N \to \nu N \pi^\circ$. Another approach to the neutral current events is the study of multi-ring events [58], because the fraction of neutral current events in the multi-ring events is significantly higher than that in single-ring events.

In this thesis, we use the zenith angle distribution of multi-ring event to reduce several systematic errors.

1.6.2 High energy sample

When neutrinos propagate in matter, we must consider the matter effect (see Sec. 1.4). The neutral current cross section for ν_μ and ν_τ are identical. Accordingly the additional potential of ν_μ is identical to the potential of ν_τ, and the $\nu_\mu \to \nu_\tau$ oscillation in matter is the same as vacuum oscillation. This effect was reported in Refs. [59, 60, 61]. As shown in Sec. 1.4, however, ν_s is not affected by the matter, as a result $\nu_\mu \to \nu_s$ oscillation is modified by matter effect. The matter effect is significant at the high energy region, therefore we study the zenith angle distribution of PC events, whose $\bar{E}_\nu \sim 26 GeV$ is higher than that of FC single-ring multi-GeV μ events ($\sim 5 GeV$).

Chapter 2

Detector

The Super-Kamiokande detector is a cylindrical 50-kiloton ring imaging water Cherenkov detector. It is located 1000 m underground in the Kamioka Observatory in the Kamioka mine in Gifu Prefecture, Japan. The 1000 m thickness of rock is equivalent to 2700 m of water. At this depth, the cosmic ray muon flux is reduced down to 10^{-5} of that of the surface. The trigger rate due to cosmic-ray muons is about 2.2 Hz. The principle of the water Cherenkov detector is explained in Sec. 2.1 and details of the experimental setup are presented in Sec. 2.2-2.5.

2.1 Water Cherenkov detector

In Super-Kamiokande, the Cherenkov photons are detected by Photo Multiplier Tubes (PMTs) surrounding the inner water mass. It can reconstruct the vertex position, number of Cherenkov rings, direction, momentum and particle type of the charged particle which produced each Cherenkov ring, based on the information of the photon arrival-time and pulse height from each PMT. This sort of detector suppresses the cost of construction, so that we can make a large detector.

Cherenkov photons are emitted from a charged particle traveling in a medium at the velocity faster than the light velocity in the medium. They are emitted on a cone with a half opening angle θ with respect to the particle direction. The directionality of Cherenkov light enables us to reconstruct the direction of a charged particle. Let β be the velocity

of a charged particle and n be the index of refraction in the medium ($n = 1.33 \sim 1.36$ in water, it depends on the wavelength of the light), the relation of θ, β and n is explained as following:

$$\cos\theta = \frac{1}{n\beta} \tag{2.1}$$

The number of Cherenkov photons emitted per unit path length par unit frequency is given by

$$\frac{d^2N}{dxd\nu} = \frac{2\pi\alpha}{c}\left(1 - \frac{1}{n^2\beta^2}\right) \tag{2.2}$$

where α is the fine structure constant, x is the path length of the charged particle, and ν is the frequency of the emitted photon. The number of Cherenkov photons emitted by a charged particle with $\beta = 1$ in the wavelength range of 300-600 n m, which is the sensitive region of our PMT, is about 340 per cm.

The total number of Cherenkov photons is related to the energy of the charged particle. Especially for electrons and gammas, it is almost proportional to the energy. We can estimate the energy of the charged particle based on the above relation. Moreover the number of charged particles is measured from the number of the Cherenkov rings on the detector wall. In addition, it is possible to identify the particle type by using the photon distribution in the Cherenkov ring.

2.2 Water tank

Figure. 2.1 shows the view of Super-Kamiokande. The whole detector is held in a stainless steel tank of 39.3 m in diameter and 41.4 m in height. The detector is separated into two parts; the inner detector, ID, is completely surrounded by the outer detector, OD. The two detectors are optically separated by a pair of opaque sheets which enclose a dead region of $\sim$55cm in thickness as shown in Fig. 2.2. There are complicated stainless steel frames for supporting the PMTs in this optically insensitive region. The reason for the division is to identify entering cosmic-ray muons from outside, to shield gamma ray and neutrons from the rock, and to separate "fully contained events" and "partially contained events".

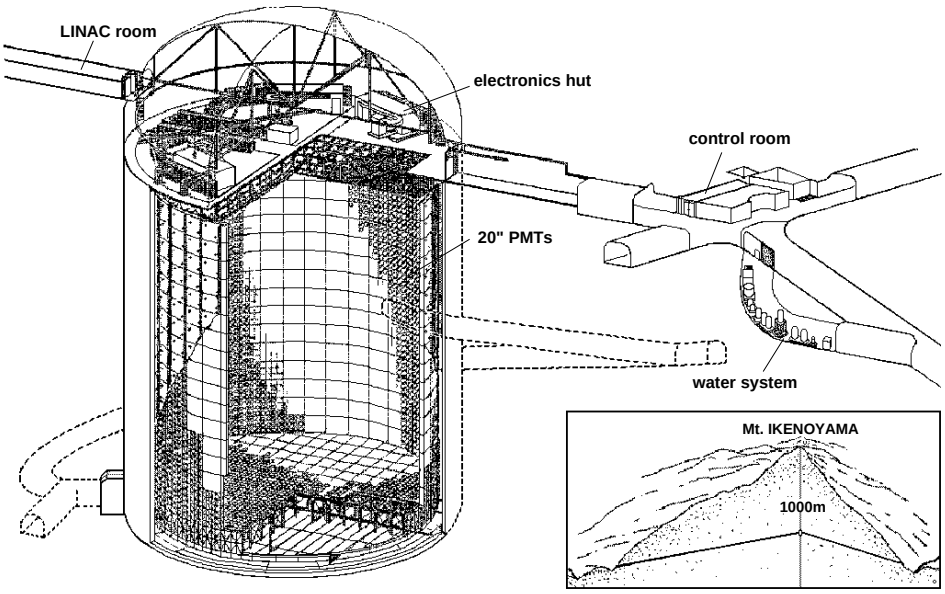

Figure 2.1: The Super-Kamiokande detector. Inset at bottom right shows the location within the mountain.

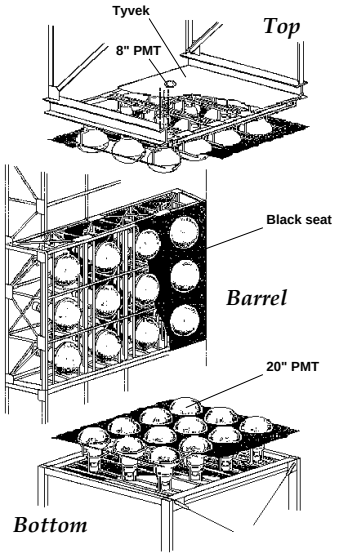

Figure 2.2: The schematic view of the frame which supports PMTs.

tank	Dimensions	39.3 m in diameter 41.4 m in height
	volume	50 kton
ID	Dimensions	33.8 m in diameter 36.2 m in height
	volume	32 kton
	Num.of PMT	1748(top and bottom) and 7650(side)
OD	Thickness	2.6 m on top and bottom
		2.75 m on side
	volume	18 kton
	Num.of PMT	302(top),308(bottom),and 1275(side)
Fiducial region	Thickness	2 m from the ID wall
	volume	22.5 kton

Table 2.1: Several parameters of the Super-Kamiokande detector.

Magnetic field of over 100 mG causes the timing resolution of PMTs worse. The geomagnetic field at the Super-Kamiokande site is about 450mG. 26 sets of Helmholz coils are located in the tank to compensate for the magnetic field. The Helmholz coils reduce the magnetic field inside the tank to 50mG.

The ID is 36.2 m in height and 33.8 m in diameter and 32,000 m^3 in volume; these dimensions are sufficient to contain muons with momentum up to 8 GeV/c. Water Cherenkov detector should have a large photosensitive area to detect as many Cherenkov photons as possible. Therefore, the ID is lined with 11146 20-inch PMTs uniformly. The ratio of the photosensitive area to the all surface area (photo coverage) is 40%, which is twice as large as that of Kamiokande. The surface of the ID is covered with black polyethylene terephtalate sheets called "black sheet" just behind the inner PMT's photo cathode as shown in Fig 2.1.

In the OD, there are 1885 8-inch outward facing PMTs with wavelength shifter plates which increase photo coverage. To maximize the light detection efficiency, all surfaces of the OD are covered with white tyvek sheets with a reflectivity of above 80 %. The thickness of the OD water including the dead region is 2.6 - 2.75 m.

The several parameters of Super Kamiokande are summarized in Table 2.1.

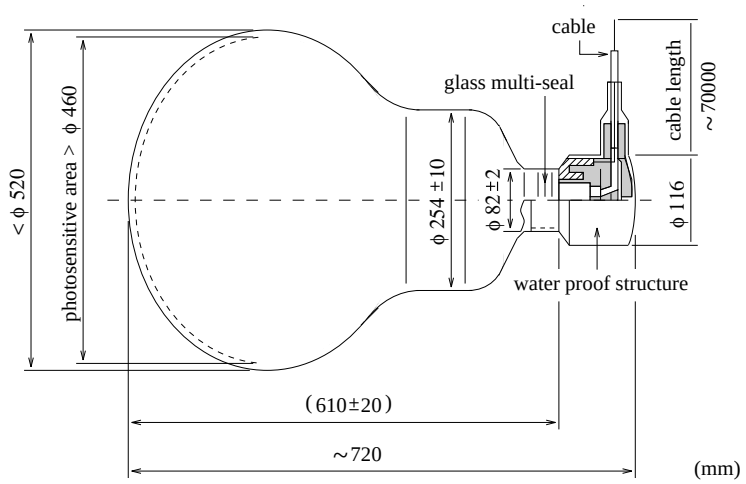

Figure 2.3: The schematic view of the PMT used in Super Kamiokande.

2.3 Photo Multiplier Tubes

2.3.1 Inner PMT

Figure. 2.3 shows a schematic view of the 20-inch PMT. The original 20-inch PMT was made by Hamamatsu Photonics Company for Kamiokande.

It was improved in the dynode shape: the bleeder chain to attain better timing and energy resolutions for Super-Kamiokande. Figure 2.4 shows the pulse height distribution for single photo-electron signals. Figure 2.5 shows the quantum efficiency of the 20 inch PMT. Properties of the PMT are summarized in Table 2.2. The details of the 20-inch PMT are presented in [62, 63].

2.3.2 Outer PMT

We use 1885 8-inch Hamamatsu R1480 PMTs, which were used at the IMB experiment, for the OD. The timing resolution of the PMT is $\sim 5.5ns$. A $6cm \times 6cm \times 1.3cm$ wave length shifter is optically coupled to each 8-inch PMT in order to enhance light collection. The wave length shifter makes the light collection increase by 60%, whereas the timing

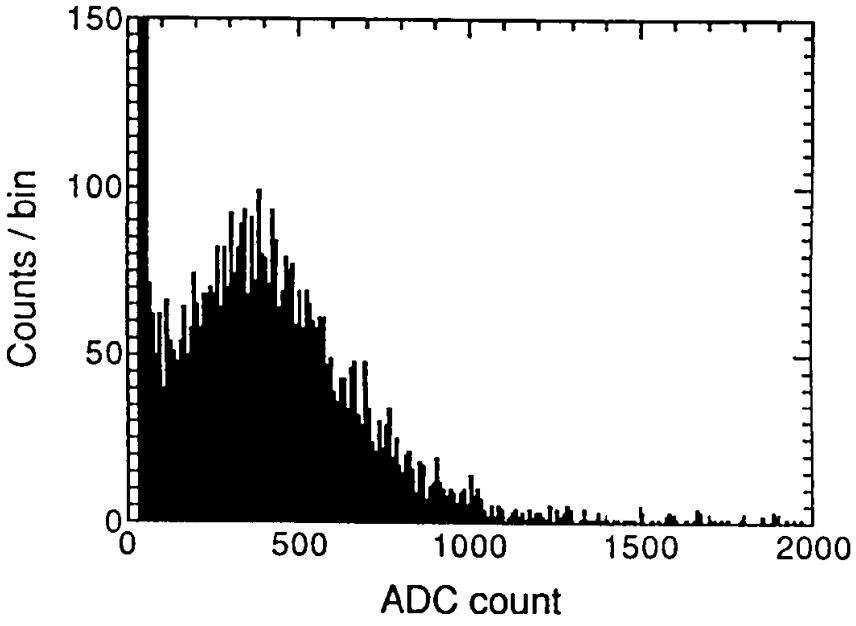

Figure 2.4: Single photo-electron distribution of the PMT used in Super Kamiokande.

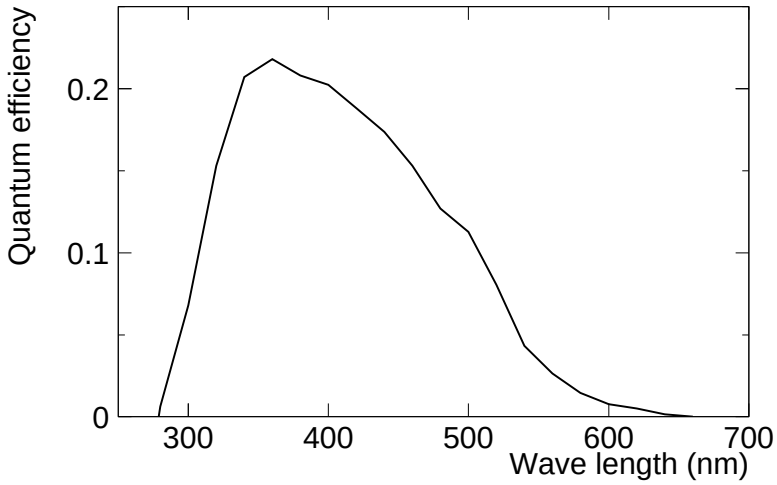

Figure 2.5: The quantum efficiency as a function of the wavelength of the light.

Photo-cathode area	50cm in diameter
Shape	Hemispherical
Window material	Pyrex glass (4∼5mm)
Photo-cathode material	Bialkali
Dynodes	11 stage, Venetian blind
Pressure tolerance	6kg/cm^2 water proof
Quantum efficiency	22% at λ=390nm
Gain	10^7 at $\sim$ 2000 Volt
Dark current	200nA at gain=10^7
Dark pulse rate	3kHz at gain=10^7
Cathode non-uniformity	less than 10 %
Anode non-uniformity	less than 40 %
Transit time spread	$\sigma \sim 2.5$ ns

Table 2.2: The properties of the 20-inch ϕ PMT

resolution goes down to $\sim 7.5ns$ which is still enough for OD.

2.4 Water purification system

In the Kamioka mine, there is clean water flowing near the detector, and it can be used freely in large quantities. In this section, the water system and the radon free air system are presented.

2.4.1 Water purification system

This water is circulated through the water purification system. The purpose of this water purification system is:

- To keep the water transparency as clear as possible. Small dust, metal ions like Fe^{2+},Ni^{2+}, Co^{2+}, and bacteria in the water should be removed.
- To remove the radioactive material: mainly Rn, Ra and Th.

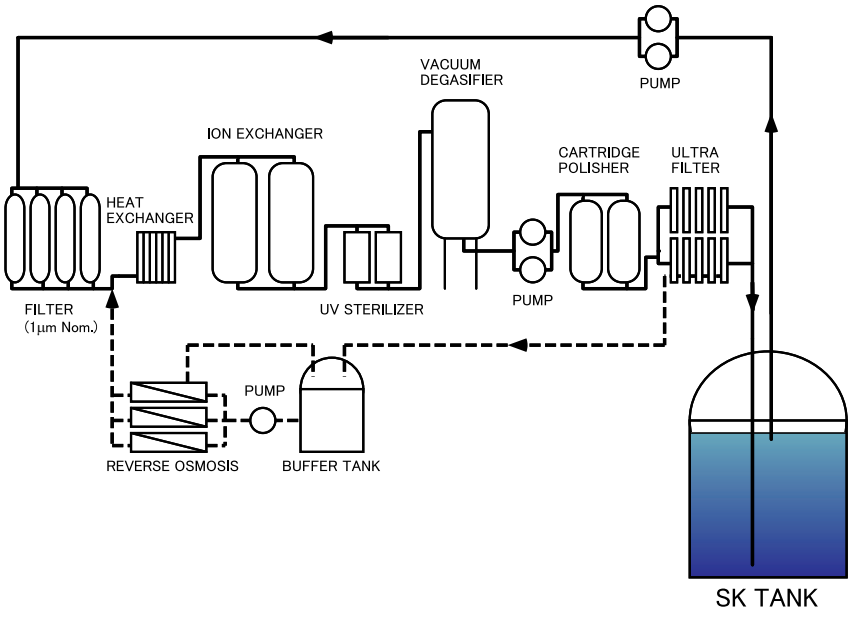

Figure 2.6: A flow diagram of the water purification system.

Fig. 2.6 shows the follow diagram of the water system. The water purification system consists of the following components,

- 1μm Filter:
- Heat-exchanger: To keep the water temperature at around 13 °C to suppress bacteria growth.
- Ion exchanger: To remove metal ions in the water.
- Ultra-violet sterilizer: To kill bacteria. According to the documentation, the number of bacteria can be reduced to less than $10^3 \sim 10^4$/1000ml.
- Vacuum degasifier: To remove gas resolved in the water. It is able to remove about 99% of the oxygen gas and 96% of the radon gas
- Ultra filter (UF): To remove small dust even of the order of 10 nm.
- Buffer tank
- Reverse osmosis

The water is taken from the top of the tank using a pump and returned to its bottom. Its flow rate is about 50 tons/hour. This system keeps the water transparency above 70m.

2.4.2 Radon free air system

There is ∼60cm space between the surface of the water and the top of the water tank. Radon gas contaminated in the air in the gap could dissolve in the water. Radon free air is sent to this region. The concentration of radon in the mine air is of order of 10∼1000 Bq/m^3. It changes seasonally because the flow of air in the mine changes. This system consists of the following components.

- Compressor: Air is compressed to 7.0∼8.5 atm.
- 0.3 μm air filter
- Buffer tank
- Air drier: To remove moisture in the gas to improve the efficiency of removing radon. This system can remove CO_2 in the gas too.
- Carbon column: To remove radon gas.
- 0.1 μm and 0.01 μm air filter
- -40°C cold carbon column

The concentration of radon in the air through this system is reduced to the order of a few $\times 10^{-3}$Bq/m^3 in all seasons.

2.5 Data acquisition system

2.5.1 Electronics for the ID

A block diagram of the electronics for the ID is shown in Fig. 2.7. The signals from PMTs in ID are sent to a TKO[1] system. The TKO system consists of 48 GONGs[2], 948

[1] Tristan-KEK-Online

[2] GO and NoGo trigger distribution module

Analog Timing Modules(ATM) [64], and 48 SCHs[3].

The main functions of ATM are to digitize the singles from the PMTs and to make trigger signals. ATM digitizes both timing and charge information of the PMT signal. ATM has the 2 channels for each PMT to reduce the dead time. If one channel is not available, the other one can be used instead. This structure enables us to detect a decay electron signal from a μ, which is very important for several analyses on the atmospheric neutrino or proton decay. The conversion factor is ~ 0.2 ns/count, and ~ 0.1 pC/count for timing and charge, respectively. The digitized data are sent to and stored in SMP[4] every 16 global trigger. The digital data from SMP modules are sent to 8 online computers for data acquisition.

The signal exceeding the threshold value corresponding to about 0.3 p.e. generates a rectangular pulse with the width of 200 nanoseconds and height of 11mV. These signals are summed to be used for the trigger. The summing signal goes through a discriminator that determines the trigger threshold. The value of the threshold is set to 320 mV corresponding to 29 hits, or approximately 5.6 MeV for electrons. This means that a global trigger is generated when 29 PMTs are hit in any 200 nanoseconds time window.

2.5.2 Electronics for the OD

Signals from the OD PMT are sent to a Charge to Time Converter (QTC) module which generates a rectangular pulse with a width proportional to the input charge. The pulses, which have charge and timing information, are digitized in Time to Distal converters: LeCroy 1887 multi-hit TDC. The TDC has 96 input channels and the minimum time unit of the TDC is 0.5 nanoseconds. This TDC can record multi-hits within a 16-microsecond window. The timing of the signal windows are set to -10 to +6 microseconds to the global trigger timing. The TDC is a FASTBUS module and its crate is controlled by a FASTBUS Smart Carte Controller (FSCC). The FSCC sends the digitized PMT data from TDCs to DPM[5] modules. Finally these data are read out by the OD data taking workstation through a VME bus.

[3]Super Controller Header, bus-interface module
[4]Super Memory Partner
[5]Dual Ported Memory

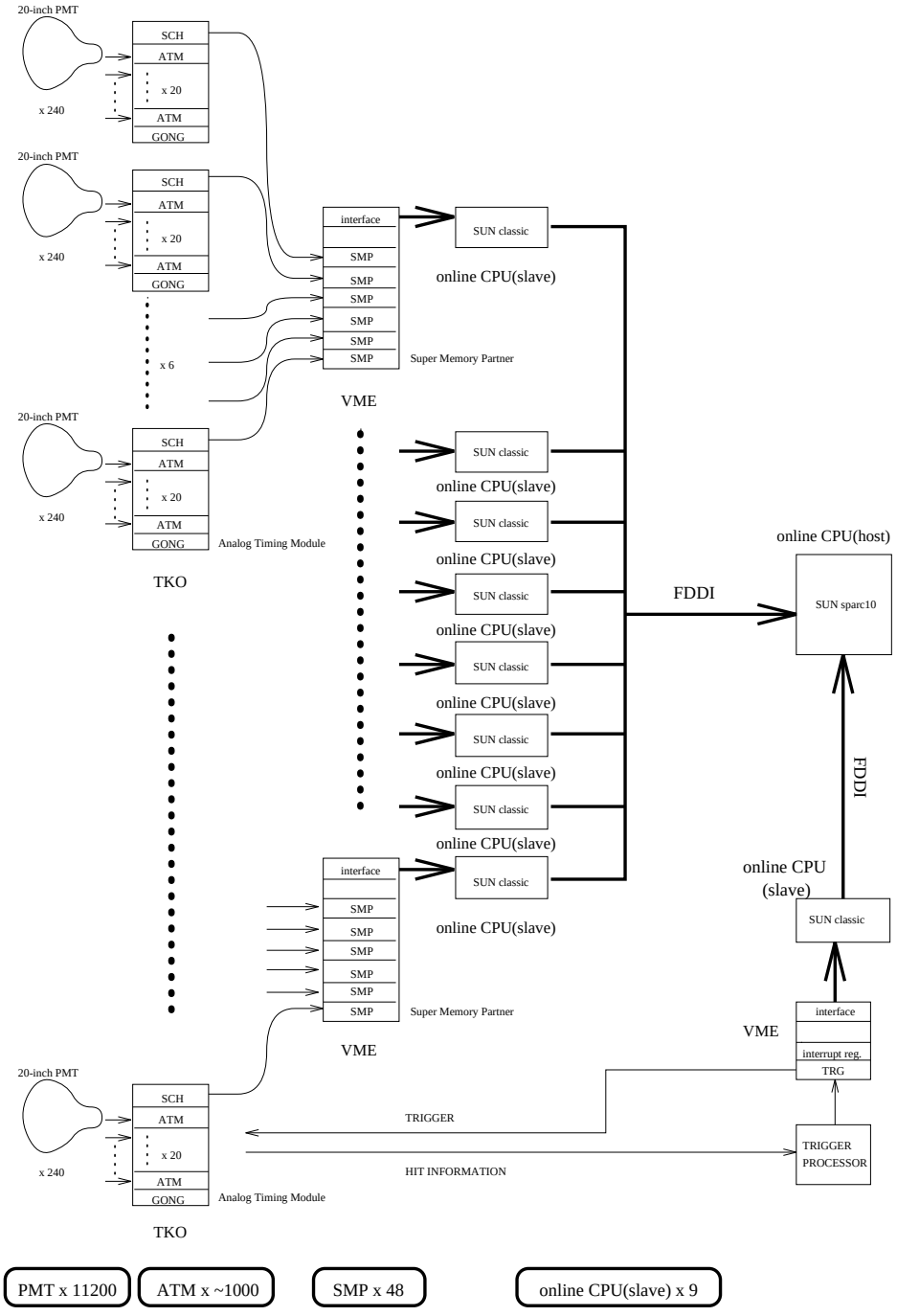

Figure 2.7: Data accusation system for the ID.

2.5.3 Online and offline systems

Each front-end workstation reads out the data from electronics independently, and transfers to an online host computer via FDDI. They are then sent to the offline computer located outside of the mine via an optical fiber cable. The data are transferred every ten minutes, and its size is about 70 MByte. The offline host computer saves all the data in a tape library. And it converts the data to offline format (ZBS[6]): ADC and TDC counts are converted to the units of photo-electrons and nanoseconds, respectively. Finally the offline data are distributed to analysis computers for the first reduction.

[6] Zebra Bank System

Chapter 3

Calibration

In order to reconstruct the neutrino events precisely, we calibrated the gain and timing response of each PMT and the absolute energy, and measured the water transparency. This chapter surveys the method of relative PMT gain calibration, absolute PMT gain calibration, timing calibration, water transparency measurements, and the absolute energy calibration.

3.1 Relative PMT gain calibration

A Xe lamp and scintillation ball system was used to calibrate the relative gain of PMTs. Figure 3.1 illustrates the setup of the relative gain calibration system. We used a Xe flash lamp as the light source, and a scintillation ball as the wavelength sifter. The light was passed through a UV filter to match the absorption wavelength of a wavelength shifter, and through ND filters to adjust the light intensity. Then it is fed into the scintillation ball via an optical fiber. The scintillation ball was made of acrylic resin, which uniformly contains 50ppm BBOT and 500ppm MgO powder to emit isotopic light. Where BBOT and MgO were used to shift wavelength and diffuse light, respectively. The typical wavelength of the light emitted from the scintillation ball was 440 nm, which is similar to the typical wavelength of Cherenkov light.

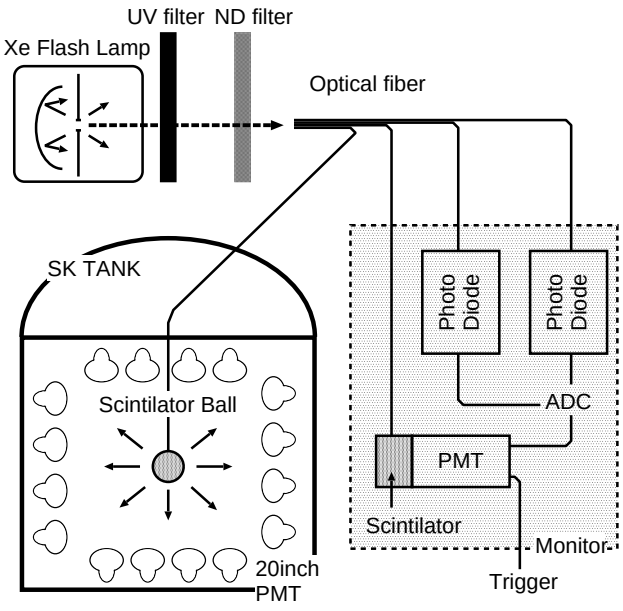

Figure 3.1: The setup of the Xe lamp and the scintillation ball system for the relative gain calibration.

The relative gain of the i-th PMT is obtained by the following equation:

$$G_i = \frac{Q_I}{f(\theta)} \times r_i^2 \times exp(\frac{r_i}{L})/Q_o \tag{3.1}$$

where $f(\theta)$ is a relative photosensitive area of the PMT viewed from an angle θ as shown in Fig. 3.2 (a); θ is an angle shown in Fig. 3.2 (b); Q_i is a charge in units of pC detected by the i-th PMT; L is a light attenuation length in the detector; Q_0 is a normalization factor to adjust the average G_i to unity. We set a high-voltage (HV) values of each PMT so that all PMTs have a common gain. We took the data for the relative gain calibration 9 times by changing the position of the scintillation ball from 1 to 35 m in height from the bottom PMT surface in order to minimize the r_i and $f(\theta)$ dependence to each PMT.

After the relative gain correction, we took the data with the same system again to check the relative calibration. Figure 3.3 shows a gain spread of the ID PMTs. According to this figure, the gain spread is reduced to be $\sim 7\%$. Since the average number of hit PMTs was about 1300 for atmospheric neutrino events, ambiguity in the energy measurement from the relative gain spread is estimated to be only $(\sim 7/\sqrt{1300}\%) = 0.2\%$. This value, 0.2 %, is much smaller then the uncertainty in the absolute energy calibration of the Super-Kamiokande detector, $\pm 2.5\%$.

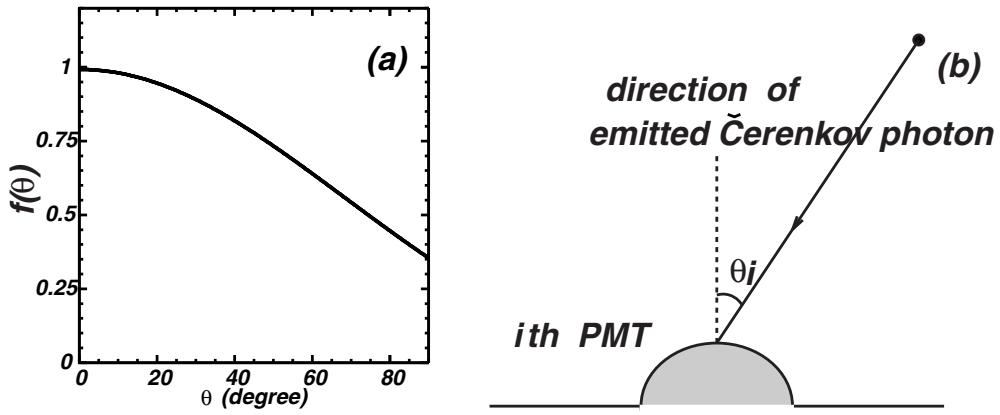

Figure 3.2: The relative photosensitive area $f(\theta)$. (a) shows the relative PMT photo sensitive area as a function of θ. (b) illustrates the definition of θ.

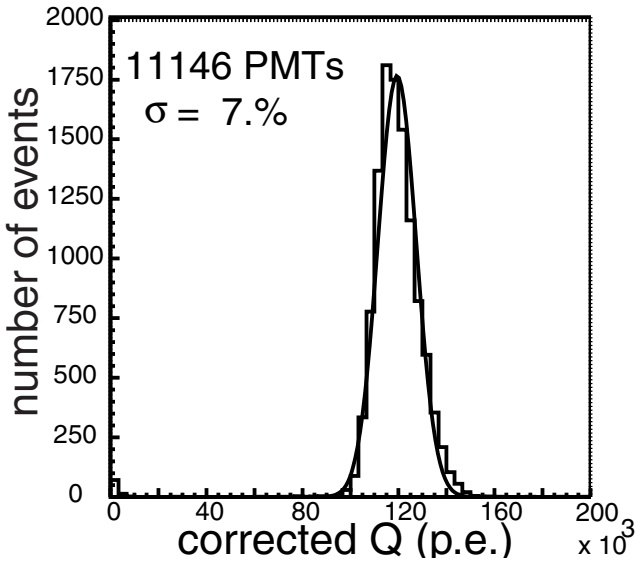

Figure 3.3: The gain spread of the ID PMTs. The spread of relative gain is reduced to be $\sim 7\%$.

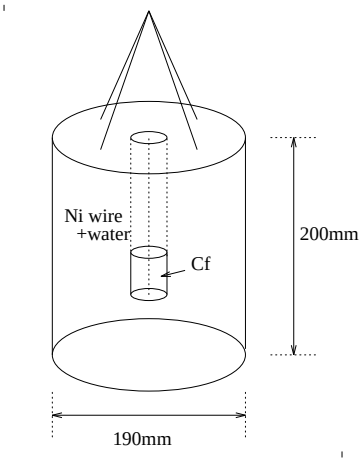

Figure 3.4: The view of Ni-Cf source

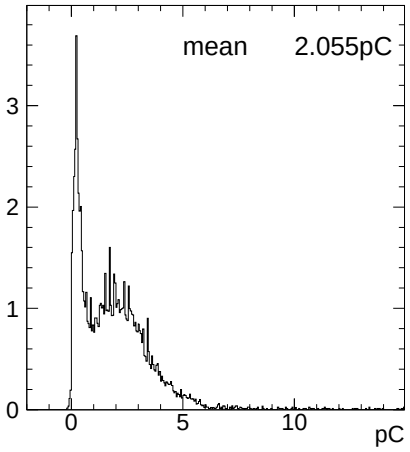

Figure 3.5: The single photo-electron distribution obtained by the Ni calibration.

3.2 Absolute PMT gain calibration

An absolute gain of the PMT was calibrated by measuring a charge distribution of single photoelectron (p.e.). In order to take the single p.e. distribution, we used low energy gamma-rays emitted from thermal neutron capture in nickel, Ni(n,γ)Ni*, because the number of p.e. in a PMT for such a low energy event is almost one. Neutrons were produced by spontaneous fission of ^{252}Cf. The Ni-Cf source shown in Figure 3.4 was located at the center of the inner detector. Figure 3.5 shows the typical single p.e. distribution. Since a mean value of this distribution was 2.055pC, the relation between pC and p.e. is $1p.e. = 2.055pC$. The absolute gain of the PMTs was $\sim 6 \times 10^6$.

3.3 Timing calibration

Let us define, T_0 as the time when a PMT signal exceeds a threshold in the discriminator. T_0 is different PMT by PMT, because of the difference of transit time and the cable length of each PMT. In addition, T_0 depends on the pulse height, because of the slewing effect that large signals tend to exceed the threshold earlier than the small ones.

In order to use the timing information in the data analyses, we have to make corrections

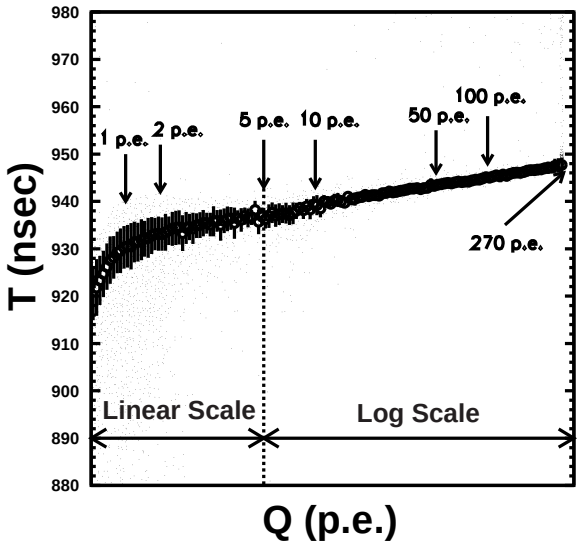

Figure 3.6: TQ map of a typical PMT. The white circles and the error bars show the peak values and resolution (at 1 sigma level), respectively.

to T_0. For this purpose, we made TQ map [1]. This map is the relation table between the pulse height and timing response, and includes the correction of transit time. In order to make this map, we used a later and diffusing ball system, because the timing width of the light source had to be narrow compared to the width of T_0 spread. Therefore we used the dye laser pumped by a pulsed N_2 laser whose pulse width is about 3 nanoseconds.

The laser light was passed through several optical filters to adjust light intensity, and then fed into a diffusing ball via an optical fiber. TQ map of each PMT was obtained by the laser calibration, and Fig. 3.6 shows a typical TQ map for a PMT. In addition, the timing resolution at each pulse height was estimated from TQ map by fitting the spread of T_0 distribution at each pulse height with Gaussian distribution as shown in Fig. 3.7. This distribution is used in the detector simulation.

3.4 Water transparency

The water transparency is an important information for the data analysis such as energy reconstruction. It was estimated by two independent methods: one method was the direct measurement by a dye laser and CCD camera; the other used the cosmic-ray muons.

[1] T(timing)-Q(charge) map

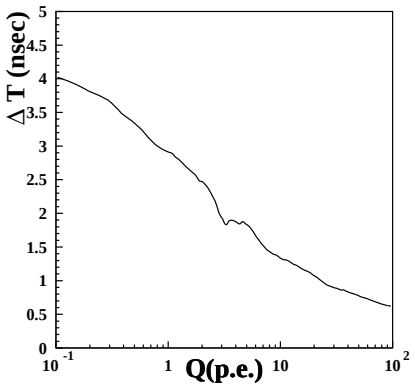

Figure 3.7: Timing resolution as a function of the pulse height.

3.4.1 Direct measurement with a dye laser

Figure 3.8 shows the setup of the dye laser plus CCD camera system. The light emitted from a dye laser was split into two optical fibers. One was fed into a 2-inch PMT to monitor the intensity of the light (I_{laser}), and the other into a diffusion ball and is remitted isotropically. The relation between the intensity of the image of the diffusion ball taken by the CCD camera (I_{CCD}) and I_{laser} is expressed as follows:

$$\frac{I_{CCD}}{I_{laser}} = const. \times exp(-\frac{l_d}{L(\lambda)}) \times \frac{1}{l_d^2} \tag{3.2}$$

where λ is a wavelength; $L(\lambda)$ is an attenuation length; l_d is the distance between the diffusion ball and the CCD. Figure 3.9 shows the observation of the $\frac{L_{CCD}}{I_{laser}} \times l_d^2$ as a function of I_d for wavelength of 420 nm. By fitting the data with a least square method, the attenuation length at 420 ns was estimated to be 92.2 ± 5.2 m. Similarly, the attenuation at various wavelengths were estimated as summarized in Fig. 3.10. These results are used in the detector simulation.

3.4.2 Cosmic-ray muon method

The attenuation length in water was also measured by the through-going cosmic-ray muons. The energy deposited by the cosmic-ray muon in the detector was almost independent of the muon energy ($\sim 2MeV/cm$), because main muon interaction with water is dominated by the ionization loss, which weakly depends on the muon energy at high energy region. Therefore the cosmic-ray muon can be used for a calibration source. Only vertical muons are used for the calibration. In contrast to the direct measurement method,

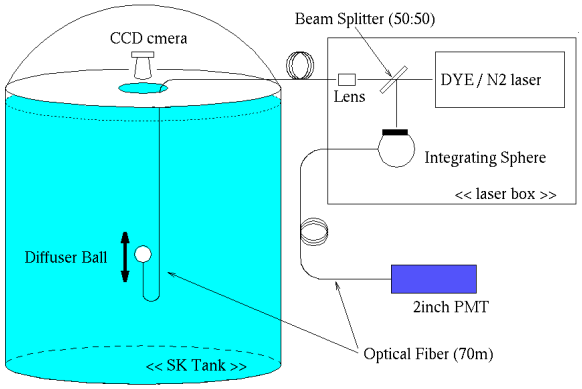

Figure 3.8: The setup of the dye laser + CCD camera system for the measurement of the waver transparency.

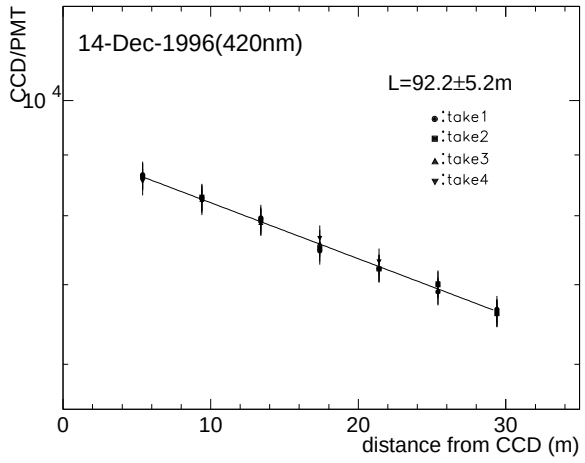

Figure 3.9: The observed light attenuation length at 420 nm.

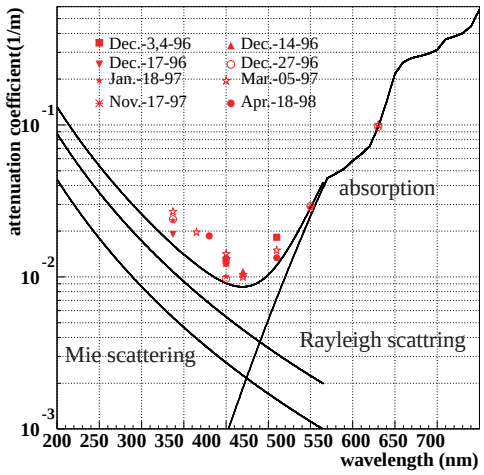

Figure 3.10: The $L(\lambda)^{-1}$ plot as a function of the wave length. Solid lines show the attenuation length used in the detector simulation.

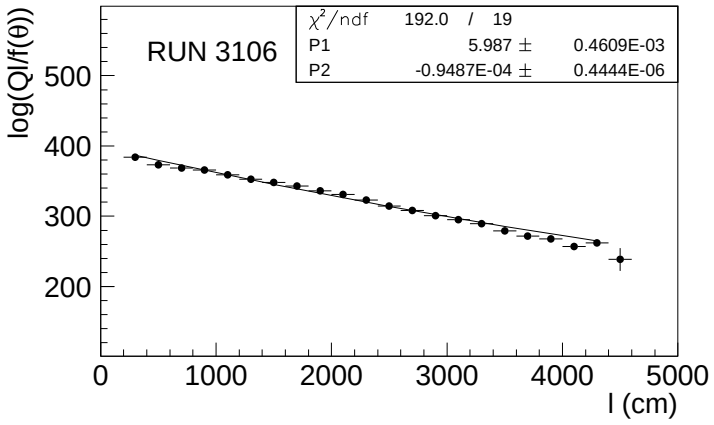

Figure 3.11: The log $\left(\frac{Q\times l}{f(\theta)}\right)$ plot as a function of l. The solid line shows the fitting result.

cosmic-ray muon method can be carried out during a normal data taking, therefore this method is useful to check a time variation of the attenuation length.

Under an assumption that the light reaching PMT was only non-scattered light, the observed charge (Q) by a PMT can be expressed by the following equation:

$$Q = const. \times \frac{f(\theta)}{l} \times exp(-\frac{l}{L}) \tag{3.3}$$

where l is the light path length; L is the attenuation length of the Cherenkov light. Figure 3.11 shows $log(\frac{Q\times l}{f(\theta)})$ plot v.s. l in a typical run. The attenuation length obtained from Fig. 3.11 was 105.4 $\pm$0.5 m(error of the fitting). Since the attenuation length in water varied with the condition of water purification system, it was calculated for each run to correct for the time variation. Figure 3.12 shows the time variation of the attenuation length obtained by the cosmic-ray muon method.

3.5 Absolute energy calibration

We must understand how precise the Monte Carlo simulation reproduces the absolute energy scale, because the systematic uncertainty in the absolute energy scale affects the atmospheric neutrino flux measurements. We have five calibration sources for the absolute energy calibration: decay electrons from stopping cosmic ray muons; π° mass; LINAC; low and high energy stopping cosmic ray muons. In this section, we describe these calibration methods.

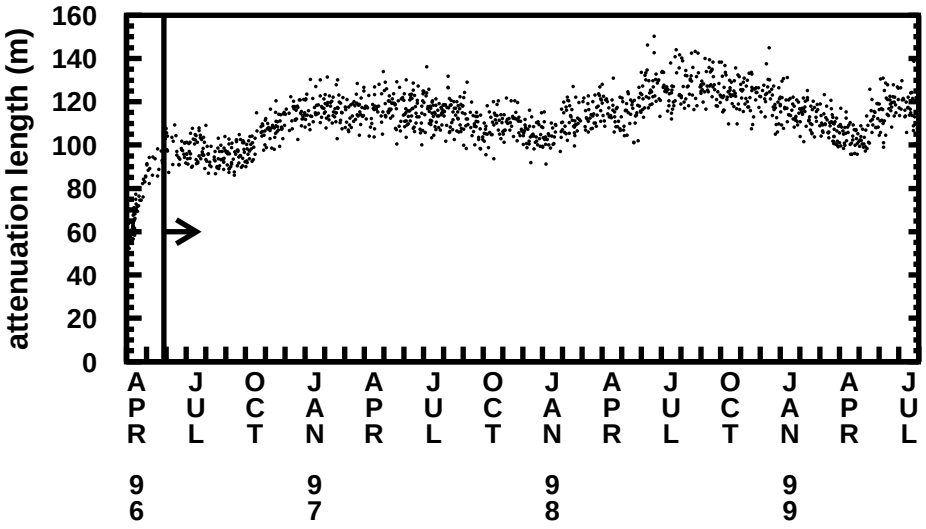

Figure 3.12: The time variation of light attenuation length in water measured by cosmic-ray muons. Only the data after the end of May, 1996 (shown by an arrow) are used in this thesis.

3.5.1 Decay electrons

We have a large number of low energy electrons by the decay of cosmic-ray stopping muons. The absolute energy scale was checked by comparing the momentum of the decay electrons from the stopping cosmic-ray muons between the real data and the Monte Carlo prediction. Decay electrons were selected with the following criteria:

1. electrons are detected from 1.5 to 8 micro seconds after the trigger of a parent muon.
2. number of ID-hits is less than 1000.
3. $goddoness_{low}$ is more than 0.5
4. the vertex position is reconstructed in the fiducial volume.

Monte Carlo events were generated uniformly in the fiducial volume and randomly for the direction. Figure 3.13 shows the momentum spectrum for electrons in the fiducial volume compared with the Monte Carlo predictions. An effect of the nucleon Column field caused by the atomic capture of a parent muon were considered [65] in the spectrum

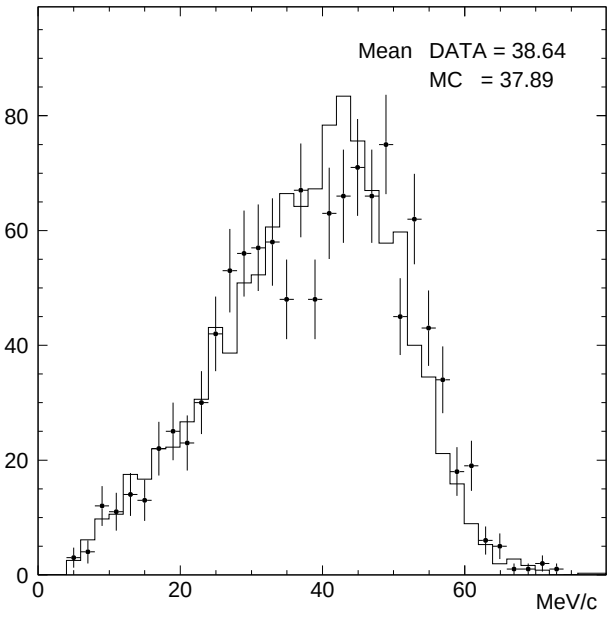

Figure 3.13: Momentum spectrum of the decay electrons from the stopping cosmic ray muons in the fiducial volume. The points with error bars show the data, and the histogram shows Monte Carlo.

of the Monte Carlo events. The spectrum of the data agrees well with that of the Monte Carlo. The mean value of the data is 2.0 % higher than that of the Monte Carlo.

The decay electron is also used to check the detector stability. Figure 3.14 shows the time variation of the reconstructed momentum of the decay electron events. This figure illustrates that the absolute gain for relatively low energy events is stable within $\pm 1\%$.

3.5.2 LINAC

In Super Kamiokande, an electron linear accelerator(LINAC) is used to understand precisely the performance of the detector for low energy events [66]. The energy of electrons cab be adjusted from 5 to 16 MeV and energy spread at the end of the beam pipe is less than 0.3 %. We used electrons with the energy of 16MeV. The injected position was 6m from the top PMT surface and the direction was downward. LINAC electron events were selected according to the following criteria:

1. number of ID-hits is between 100 and 210.
2. $goodness_{low}$ is more than 0.5.
3. the distance between the injected position and the reconstructed position is less than 2m.

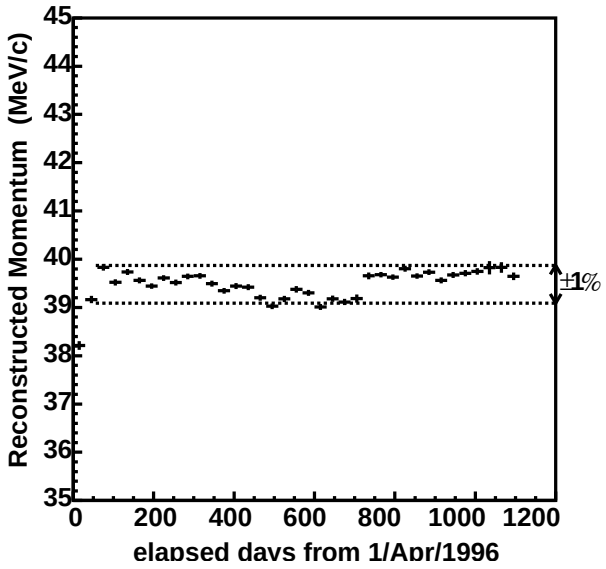

Figure 3.14: Time variation of the reconstructed momentum of the decay electron.

Figure 3.15 shows the momentum distribution for LINAC electrons compared with the Monte Carlo events. The agreement of the momentum distribution between the data and Monte Carlo is satisfactory. The mean value of the real data was 2.4% lower than that of the Monte Carlo.

3.5.3 π° mass

Selection criteria of π° events are described in Appendix. B. Here we explain the result only. We estimate the uncertainty in the π° reconstruction efficiency to be 7% (see Appendix. B). Since this uncertainty increases with increasing π° momentum,we used the π°'s with momentum < 400 MeV/c to reduce the uncertainty. Figure 3.16 shows the M_{π° distribution for the real data and the Monte Carlo. The fitted peak is 2.5% higher for the real data than for the Monte Carlo.

3.5.4 Low energy stopping cosmic ray muons

Using the opening angle of the Cherenkov ring for low-energy muons, we can estimate the momentum independent of the p.e. information to check the systematic uncertainty of the momentum reconstruction. The relation between the momentum, p, and the opening

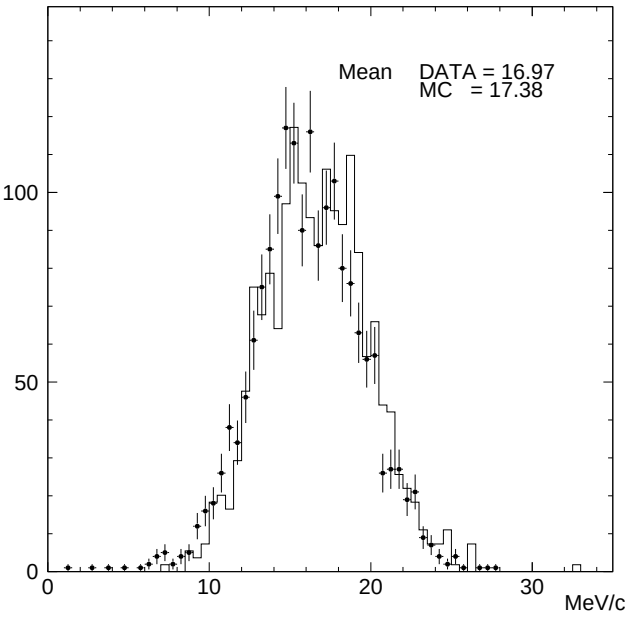

Figure 3.15: Momentum spectrum of LINAC electrons. The points with error bars shows the data, and the histogram shows Monte Carlo.

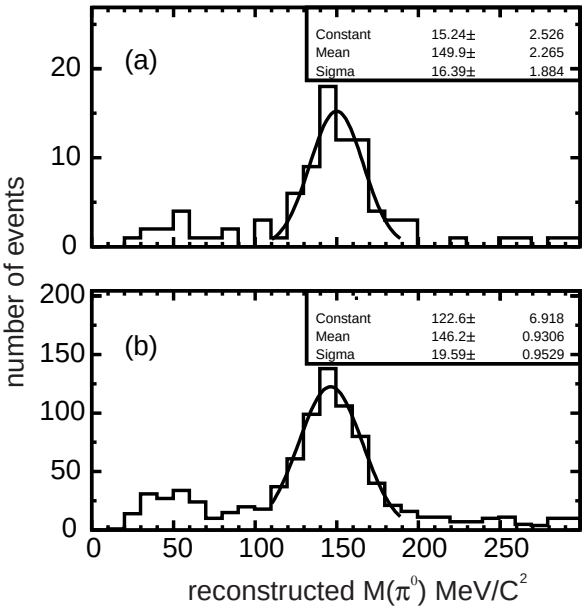

Figure 3.16: M_{π° distributions. (a) for data, (b) for Monte Carlo prediction. The solid line shows the result of a Gaussian fit.

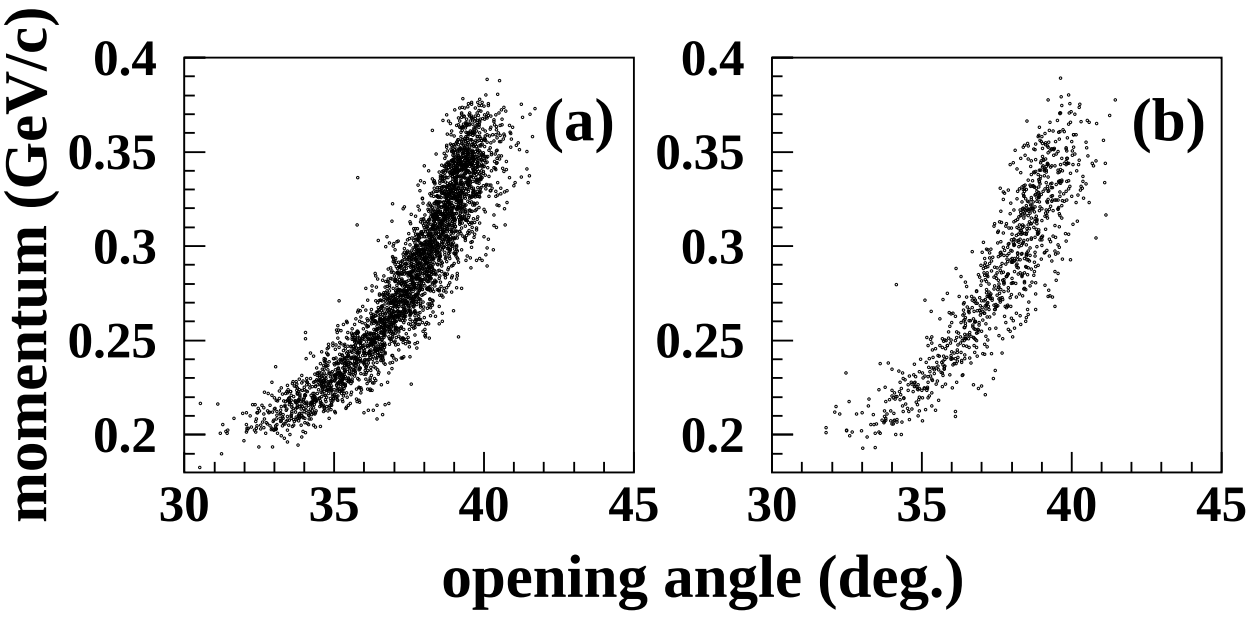

Figure 3.17: Opening angle vs momentum plots for the stopping muon events; (a) for the real data, (b) for the Monte Carlo.

angle, θ, is given by:

$$\cos\theta = \frac{\sqrt{p^2 + m_\mu^2}}{np} \tag{3.4}$$

where n is the index of refraction of the water, and m_μ is the muon mass. We used stopping muons which enter from the top wall and have one decay-electron. Figure 3.17 shows the reconstructed momentum as a function of the opening angle for the low energy stopping muon events. We calculated a (momentum)/(momentum estimated by the opening angle) ratio, R_p. To estimated the momentum dependence, data are divided into 5 momentum bins. Figure 3.18 shows the $R_p(MC)/R_p(data)$ plots as a function of momentum. This figure illustrates the systematic uncertainties of the momentum determination between the data and the Monte Carlo. The deviation from unity is less than ± 1.5 %.

3.5.5 High energy stopping cosmic ray muons

In the high energy region, the range of the stopping muon is used to check the absolute energy scale, because the range of the stopping muons is proportional to the muon

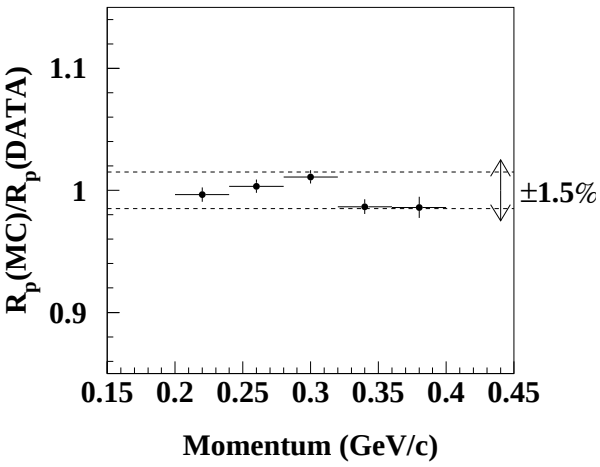

Figure 3.18: $R_p(MC)/R_p(data)$ plots as a function of momentum. Crosses show the average of $R_p(MC)/R_P(data)$, and dotted lines show ± 1.5 %.

momentum and it is easy to calculate the end point of the muons by finding the vertex position of the muon-decay electrons. The range is defined as the distance from the vertex position of the stopping muon to the vertex position of its decay electron. Figure 3.19 shows the momentum and range ratio as a function of range. The energy deposit per 1cm is about 2.5 MeV. We used the events with the range longer than 7 m, because the ambiguity of the vertex determination affects the range determination when the range is short. Events were devised into 6 bins by the range. The average of the momentum/range ratio for the real data and the Monte Carlo were calculated and the ratio is taken. Figure 3.20 shows the ratio for the real data and the Monte Carlo events. The ratio for the real data was about 2.6 % lower than that for the Monte Carlo.

Moreover we checked the detector stability by using this ratio Figure 3.21 shows the time variation of the ratio, and demonstrates that the absolute gain at relatively high energy range is stable within ±1%.

3.5.6 Summary of the absolute energy calibration

Figure 3.22 summarizes the studies for the absolute energy scale. Events with the momentum from 16 MeV/c to about 10 GeV/c were examined and the energy scale for the Monte Carlo events agreed with that for the data within +2.6% and -2.5%.

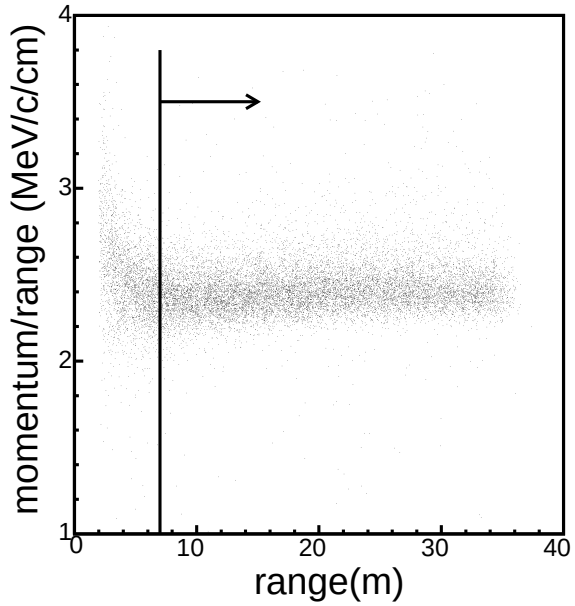

Figure 3.19: Momentum/range ratio of the stopping muon as a function of range.

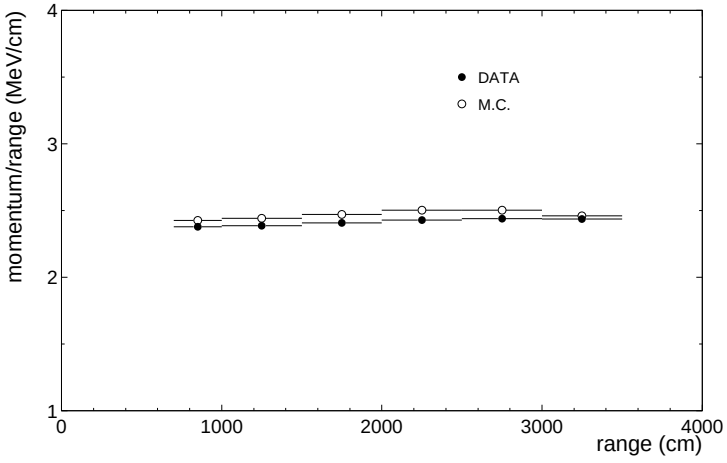

Figure 3.20: Momentum/range plots as a function of range.

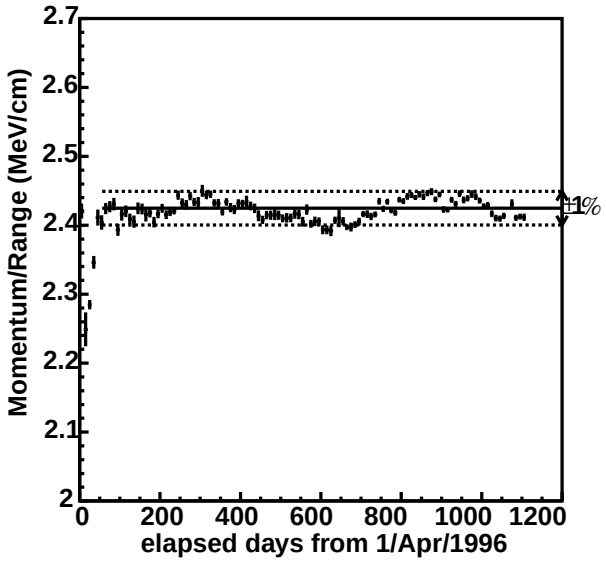

Figure 3.21: Time variation of the reconstructed momentum/range for the real stopping muon events.

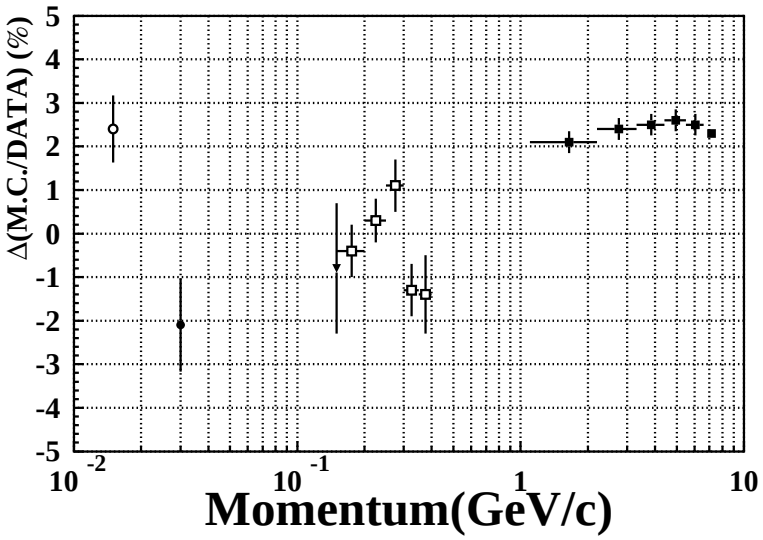

Figure 3.22: Summary of the absolute energy calibration; the white circle for LINAC, the black circle for decay electron, the triangle for π°, the white squares for the low energy stopping μ, and black squares for the high energy stopping μ.

Chapter 4

Data reduction

4.1 Reduction outline

Atmospheric neutrino events have two basic topologies that determine the data reduction stream. If all of the visible energy is contained within ID, the event is called "fully contained event"(FC). An event for which some produced particles deposit visible energy in the OD is called "partially contained event"(PC). Figure 4.1 shows the definitions of the FC and PC events. In this analysis, we used the data set from May 27, 1996 to April 3, 1998, which corresponded to 848 days of detector livetime, and the number of recorded events for this period were about 800 millions.

The main backgrounds for atmospheric neutrino events are the cosmic ray muon events and low energy radioactivity in the detector.

This chapter surveys the FC and PC reductions.

4.2 FC reduction

The reduction for FC sample contains four steps. Figure 4.2 shows the algorithm of the FC reduction. Each reduction step is described below.

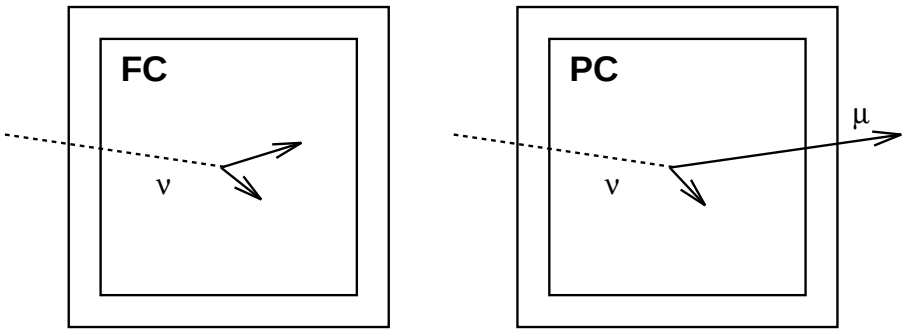

Figure 4.1: Definitions of the FC and PC events. The FC events required that all visible particles stop in the ID, whereas the PC events have 1 particle reaching the OD.

4.2.1 First reduction

The first step of FC reduction was low energy events cut and OD cut. The events whose total photo-electrons within 300 ns (PE_{300}) were less than 200 p.e. (corresponding to visible energy < 23 MeV) were rejected. These low energy events were caused by radioactivity such a radon in the detector or gamma ray coming from the rock. Figure 4.3 shows the PE_{300} distributions for the data and the Monte Carlo of the atmospheric neutrino events with visible energy greater than 30 MeV. This figure demonstrates PC_{300} cut is safe for FC neutrino events.

The cosmic ray muon events had hit OD PMTs near the entrance and exit points, and they were rejected by eliminating the events for which the number of the hit OD PMT within 800 ns ($NHIT_{800}$) was greater than 50. After these cuts, the event rate was reduced to 4,000 event/day.

4.2.2 Second reduction

In the next reduction step, we required a tighter OD and a max photo-electron cuts. OD cut is essentially same as the first reduction, but here the events with $NHIT_{800}$ greater than 25 were removed. Figure 4.4 shows the $NHIT_{800}$ distribution for the data and the Monte Carlo prediction for FC sample. This figure demonstrates $NHIT_{800}$ cut is safe for FC event sample.

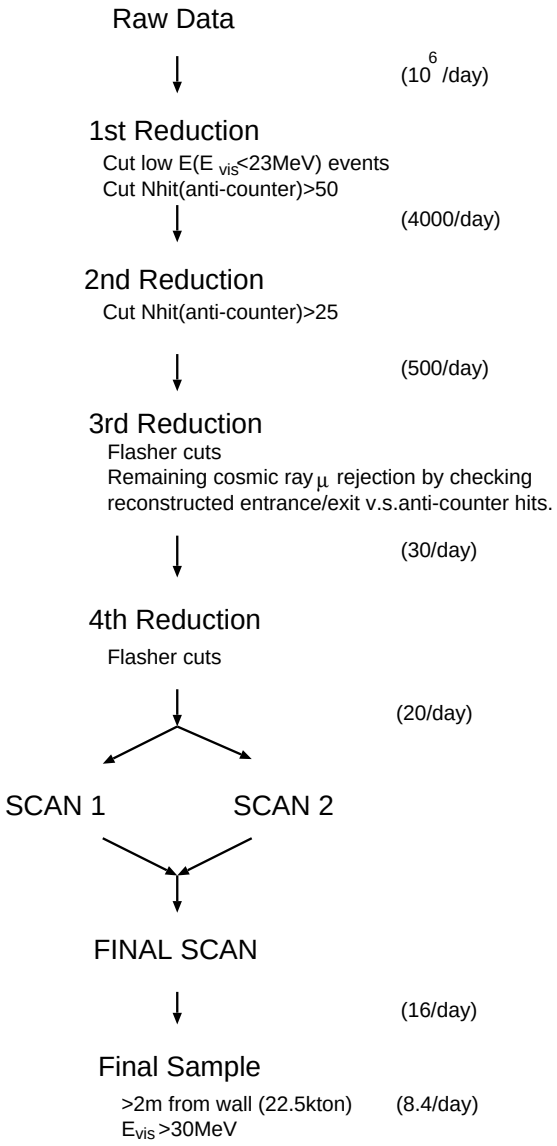

Figure 4.2: Algorithm of the FC reduction.

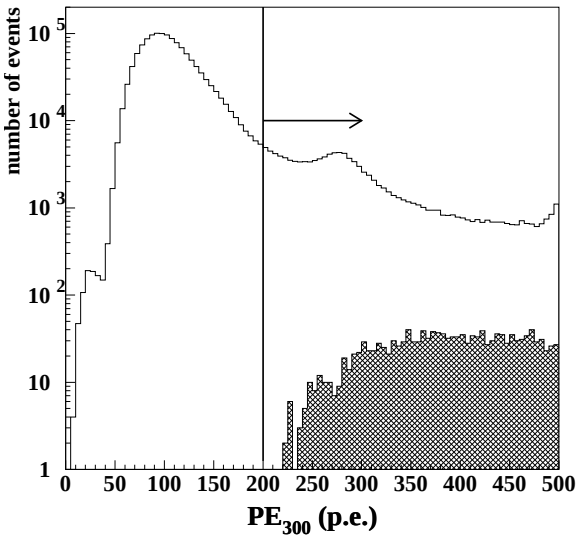

Figure 4.3: PE_{300} distribution for 512 days data; the white histogram for the raw data, the hatched one for the Monte Carlo events with visible energy $> 30MeV$. These Monte Carlo events are produced in the fiducial volume, and their rates are normalized by the data livetime. The line shows the PE_{300} cut.

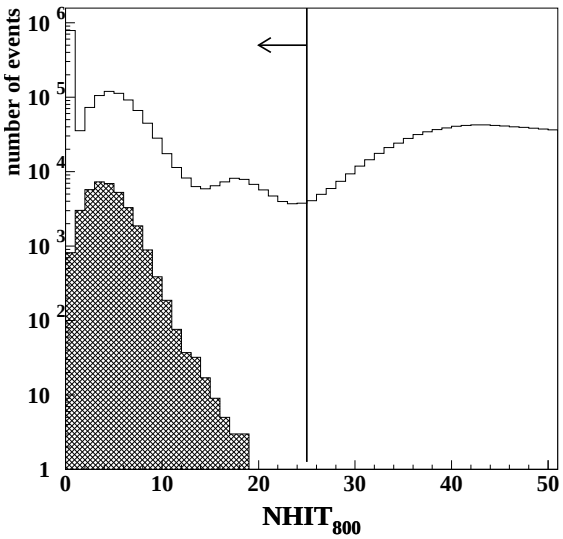

Figure 4.4: $NHIT_{800}$ distribution for 521 days data; the white histogram for the raw data, the hatched one for the FC Monte Carlo sample within the fiducial volume. The solid line shows the $NHIT_{800}$ cut.

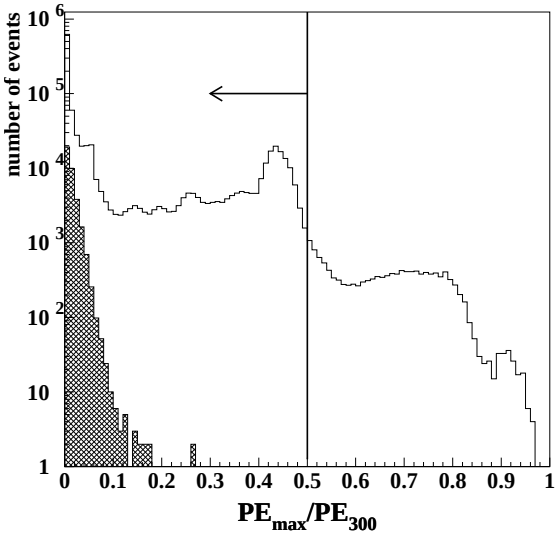

Figure 4.5: PE_{max}/PE_{300} distribution for 512 days data; the white histogram for data after the first reduction and the hatched one for the atmospheric neutrino Monte Carlo events within the fiducial volume. The Monte Carlo events are normalized by the live-time of data.

Max photo-electron cut was applied to reject the "flashing PMT" events. If some problems occur in the dynode of a PMT, this PMT can make a large charge signal. To eliminate these events, we required the $PE_{max}/\ PE_{300}$ ratio less than 0.5., where PE_{max} is a maximum number of p.e. in PMTs. Figure 4.5 shows the PE_{max}/PE_{300} distribution, and it demonstrates that the max photo-electron cut is safe for neutrino events.

The number of events satisfied these criteria were about 400 events/day.

4.2.3 Third reduction

The next reduction step is composed of more intelligent algorithms. The remaining events except for neutrino events were either through-going muons, stopping muons, low energy events, "flashing PMT" events, "cable hole" muons, or an accidental events. These backgrounds were rejected by the following cuts.

Through-going muon cut

As shown in Fig. 4.6, remaining through-going muon events have some hits in the OD, and make many Cherenkov photons in ID. Therefore, the events with $PE_{max} > 230 p.e.$ and the number of hit PMTs > 1000 were candidates of through-going muons and were applied a special fitter, Through-going muon fitter. The entrance point was determined by the position of the earliest hit ID PMT with two or more neighbor PMTs hit. Many

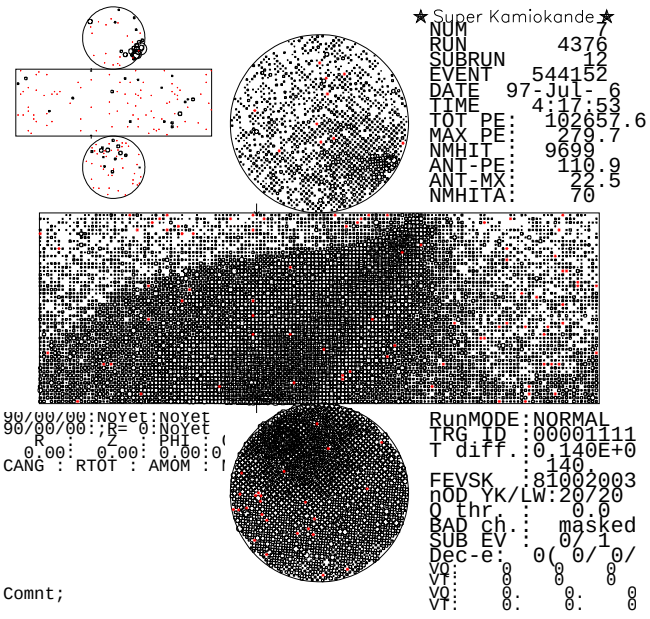

Figure 4.6: A typical through-going muon event rejected by the through-going muon cut. The circles in the figure show the hit PMTs and the area of the circle is proportional to the observed p.e numbers. The small figure on the upper left side displays OD.

Cherenkov photons are detected around the exit point of a muon, thus the exit point was defined as the center position of saturated PMTs. The events satisfying the following conditions were identified as the through-going muons and rejected.

- the number of OD hit PMTs within 800 ns timing window within a radius of 8 m from the entrance or exit point in the outer detector was greater than 9.

Figure 4.7 shows the number of OD hit PMTs distributions for the through-going candidate events and the atmospheric neutrino Monte Carlo.

Stopping muon cut

Figure 4.8 shows a typical stopping muon. In this reduction step, the Stopping muon fitter was used. It searched the vertex point in the same way as the Through-going muon fitter. And the direction was estimated by maximizing of the p.e. within the cone with opening angle 42°. Selection criteria for stopping muon cut were as the following.

1. The number of hit PMTs within 800 ns timing window within a radius of 8 m from the entrance point, OD-hit$_{ent}$, was greater than 9.

2. OD-hit$_{ent}$ was more than 4 and the goodness of the stopping muon fit was greater than 0.5.

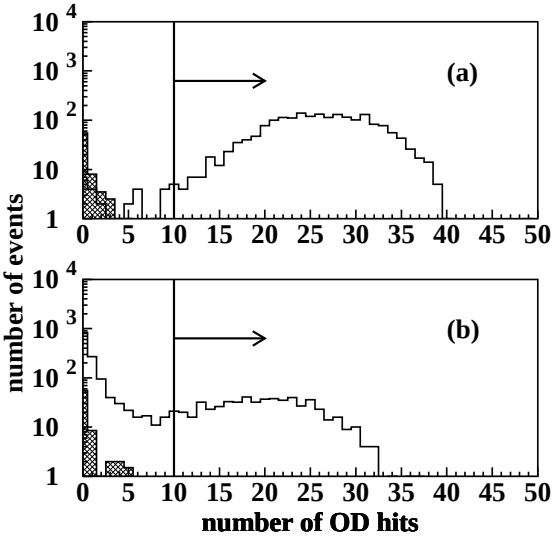

Figure 4.7: The number of OD hit PMTs distribution; (a) for the number of hits in the cluster near the entrance point of the cosmic-ray muon, (b) for the exit point. The white histogram is for the through-going muons event, and the hatched one for the atmospheric neutrino Monte Carlo events within the fiducial volume. The exposure of data and Monte Carlo is 521 days.

where the definition of goodness is the same as TDC-fit (see 5.2). Figure 4.9 shows the OD-hit$_{ent}$ distribution. The event which satisfied either one of the above criteria was identified as a stopping muon and removed.

Low-energy event cut

In this step, "low-energy fitter" was used. This fitter searches for the vertex point with an assumption that all photons were produced at a point. See Sec. 5.2.1 for the description of the essential idea of this fitter. Low energy cut excluded the event with the number of ID-hits less than 500 and N_{50} less than 50. Where N_{50} is the maximum number of hits within 50 ns window in the time residual (time - time of flight of Cherenkov photon). This value is almost proportional to the visible energy at the low energy region and $N_{50} = 50$ corresponds to visible energy $\sim 10MeV$.

Flashing PMT cut

A "Flashing PMT" event was defined as the event caused by the light emitted by a PMT with a mechanical problem in the dynode structure (internal corona discharge). Most of the events have a board timing distribution compared to the neutrino events, therefore "flashing PMT" events were selected using the width of the timing distribution. We define, N_{min}, the minimum hits within a 100 ns sliding time window in off-timing region of 300 to 900 μs after the event trigger. We rejected the events satisfying either of the

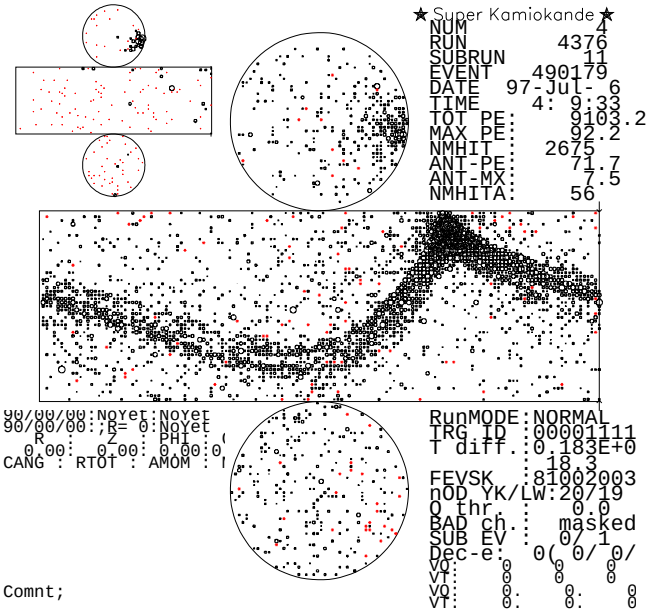

Figure 4.8: A typical stopping muon event rejected by the stopping muon cut.

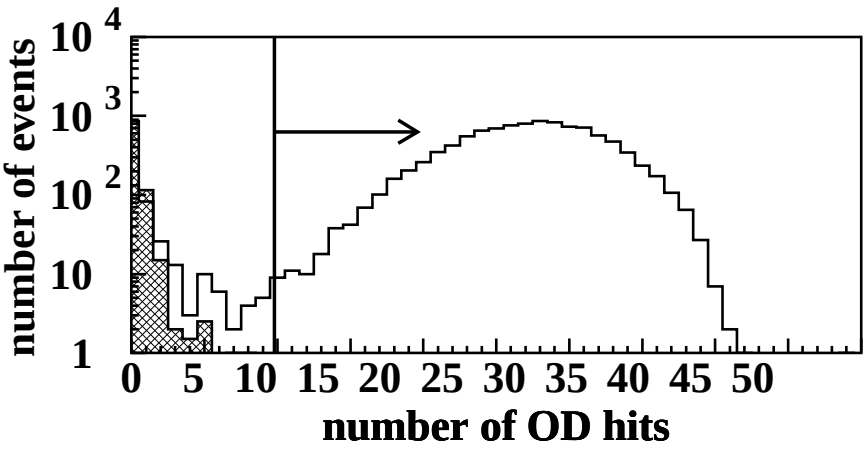

Figure 4.9: The number of OD hit PMTs distribution for the stopping muon events; The white histogram is for the stopping muon events and the hatched one for the atmospheric neutrino Monte Carlo events within the fiducial volume. The exposure of data and Monte Carlo is 521 days.

following selection criteria as the "flashing PMT".

$$N_{min} > \begin{cases} 15 & ID \text{ hits} > 800 \\ 10 & \text{otherwise} \end{cases} \tag{4.1}$$

Accidental hit cut

The accidental hit cut rejected the event that had two or more independent particles in an event accidentally. An event was rejected as accidental if both of the following conditions were satisfied.

1. OD-hits with a 500 ns time window between 400 to 900 ns after the event trigger was more than 20.

2. The total photo-electron number in ID within a 500 ns time window between 400 to 900 ns was more than 5000 p.e.

Cable hole muon cut

Cables from ID and OD PMTs were bundled in the upper OD-layer and were taken out of the tank through the 12 cable-holes. Four of the 12 cable-holes were located away from the fringe of the tank, and the identification efficiency of the OD was low for muons passing near these cable-holes. In order to compensate for the inefficiency of the OD around the four cable-holes, we installed 2.0m $\times$ 2.5m veto-scintillation counters on each of the four cable-holes in April 1997. Figure 4.10 shows the vertex position distribution of FC sample before/after installation of the veto-scintillation counters. This figure shows that the veto counters reject the muons through the cable-holes.

An event satisfied both of the following conditions was identified as a cosmic ray muon and rejected even if there were a few OD hits.

1. One of the veto-scintillation counters was hit.

2. Vertex was reconstructed within 4m from the cable-hole by the stopping muon fitter.

The number of events passing the above reductions was 30 events/day.

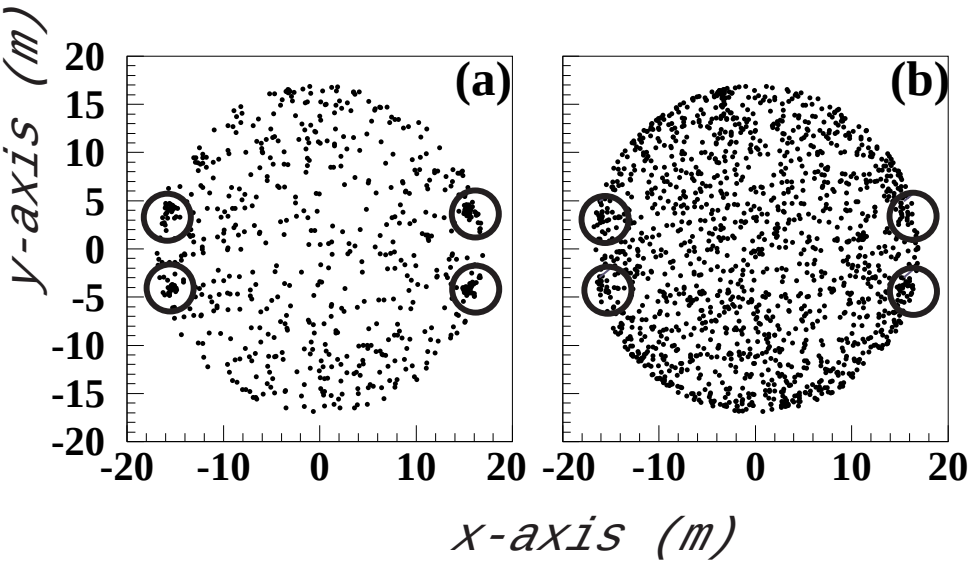

Figure 4.10: The vertex position distribution of the FC final sample with $z > 16.10m$, which indicates these events are out of the fiducial volume. The eight circles show positions of cable holes. (a) is for the distribution before installation of the veto-counters. (b) is after the installation.

4.2.4 Fourth reduction

Next reduction was another "flashing PMT" cut using pattern recognition algorithm. Since some "flashing PMT" events had the similar timing distribution as neutrino events, they were not rejected by the third reduction. The remaining "flashing PMT" events had repeated charge pattern, therefore we applied a pattern recognition program to remove them. The algorithm of this program is the following:

1. divide detector's wall into 1350 regions roughly 2 × 2 m patches,
2. compute the sum of charge in each patch : q_i,
3. for two independent events A and B, compute a linear correlation:

$$r = \frac{1}{n} \sum \frac{(q_i^A - \langle q^A \rangle) \times (q_i^B - \langle q^B \rangle)}{\sigma_{q^A} \times \sigma_{q^B}} \tag{4.2}$$

where $\langle q_i^{A(B)} \rangle$ and $\sigma_{q^{A(B)}}$ is the average and the deviation of $q^{A(B)}$, respectively. r takes the value of less than 1 and the higher value is estimated to be better matched.

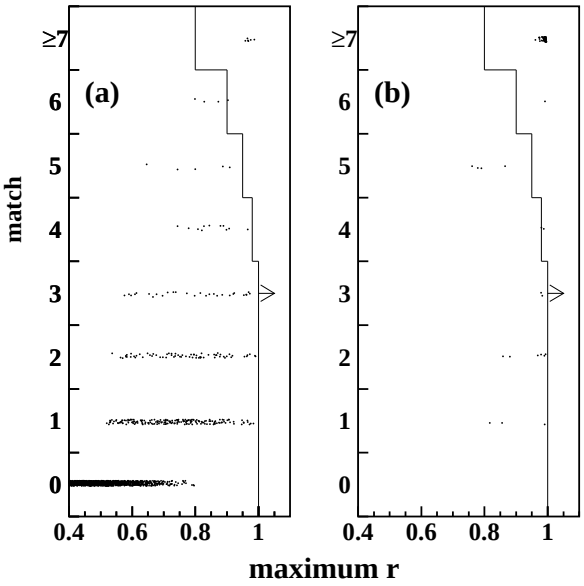

Figure 4.11: "match" v.s. "maximum r planes; (a) for the selected events by eye-scan, (b) for the flashing PMT events. Solid lines show the cut criterion for the forth reduction. Events at the right of the cut lines are rejected as flashing PMT events.

4. define "match", which is a number of events satisfying in $r > r_{ant}$, where r_{ant} is the cut value in r,

5. an event is eliminated by a cut in a two dimensional "match"-"maximum r" plane as shown in Fig. 4.11.

The events passing this reduction were reduced to 20 events/day.

4.3 PC reduction

The reduction for PC contains five steps. Figure 4.12 shows the algorithm of the PC reduction. Each reduction step is described below.

4.3.1 First reduction

In first step of PC reduction, low energy events with less than 1000 total p.e. were removed, corresponding to muons (electrons) with momentum less than 310(110) MeV/c. By definition, exiting particles must have reached the OD from the inner fiducial volume,

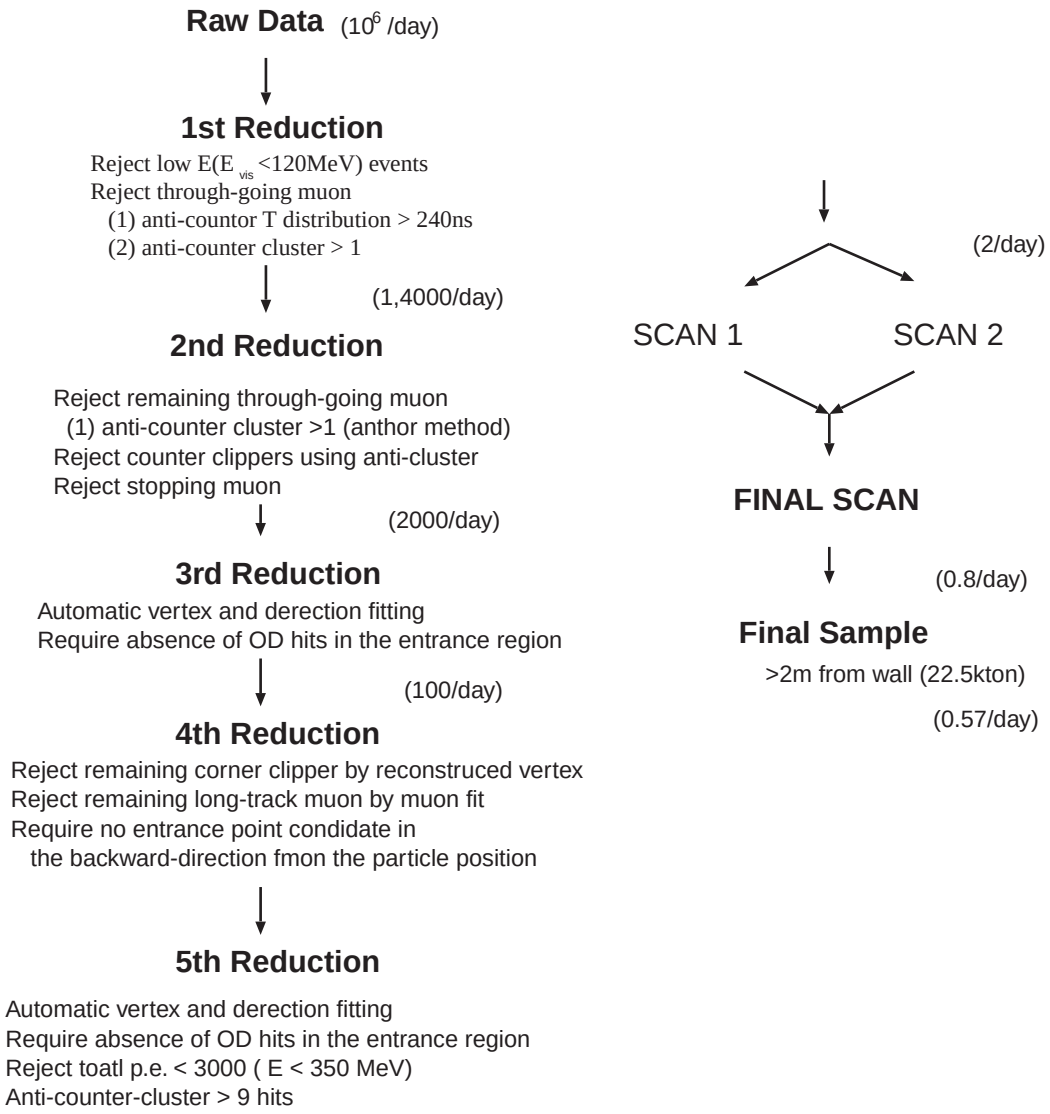

Figure 4.12: Algorithm of the PC reduction.

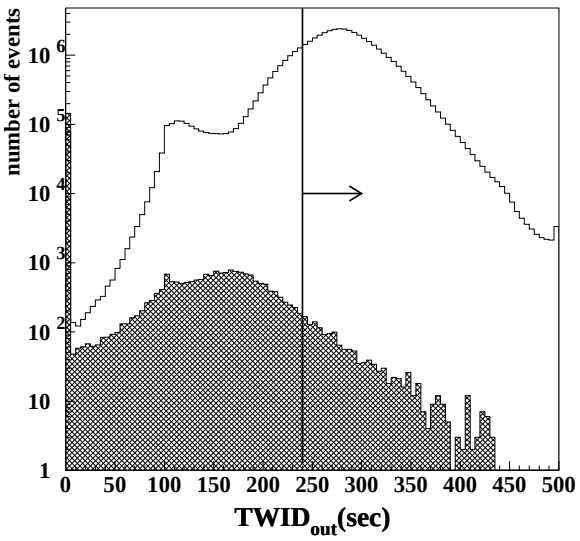

Figure 4.13: $TWID_{out}$ distribution for 521 days data. The white histogram shows the data distribution, and the hatched one shows the Monte Carlo prediction of FC+PC sample which is produced in the fiducial volume. The exposure of Monte Carlo is the same as that of data. The solid line shows the cut criterion $TWID_{out} = 240$ns.

and therefore must have had a minimum track length of about 2.5 m (corresponding to muons with $>$ 700 MeV/c momentum).

Most of through-going muons were rejected in this reduction step using timing distribution of OD hits. Typical through-going muon events have two OD clusters and therefore have a broad timing distribution of OD, hence the events whose width of the time distribution of hits in the OD, $TWID_{out}$, exceeded 240 ns were eliminated. TWID$_{out}$ is shown in Fig 4.13.

Moreover we required the number of cluster in the OD should be less than or equal to 1 in order to reject the through-going muon events. The definition of the cluster used in the first reduction is that the spatial cluster of neighboring hit-PMTs. One cluster is formed around PMT which has more than 8.p.e. and the clusters which lie within 8 m are merged. Figure 4.14 shows the number of OD clusters, $NCLSTA$, distribution of data and atmospheric neutrino Monte Carlo. This criterion is safe for PC neutrino events.

4.3.2 Second reduction

The second reduction is also based on a clustering of the ID and OD signals. The OD clusters are calculated by an algorithm shown in Fig. 4.15. Each grid is separated by 10 m $\times$ 10 m size in the OD. The cluster is formed by looking at the charge gradient

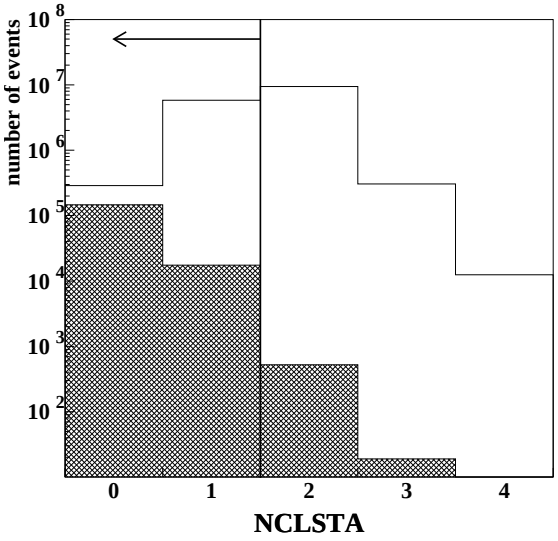

Figure 4.14: $NCLASTA$ distribution; the white histogram for the data distribution, and the hatched one for the Monte Carlo prediction of FC+PC sample which is produced in the fiducial volume. The exposure of data and Monte Carlo is 521 days.

to the neighboring grids. We required that the number of the OD cluster, $NCLASTA2$ which have more than 7 hit PMTs should be less than or equal to 1. This cut eliminates remaining through-going muons.

The cosmic muons that clipped the edge of ID were eliminated based on the topology of the OD cluster. Cosmic ray muons which entered and stopped in the ID were removed by excluding events whose ID photo-electrons within 2.0 m from the OD cluster, PE_{200} were less than 1000 p.e. This cut was safe for PC neutrino events because PC events must have left large numbers of photo-electrons near the exit point. Figure 4.16 shows the PE_{200} distributions for the data and PC Monte Carlo events. The event rate after the PC second reduction is about 2000 events/day.

4.3.3 Third reduction

In the third reduction, the remaining cosmic-ray muon and "flashing PMT" events were rejected.

The "flashing PMT" events were rejected in the same way we did for the FC "flashing PMT" events (see Sec. 4.2.3).

In order to identify cosmic-ray muon, a simple vertex fit and direction estimate "Point fit "(see Sec. 5.2.1) were used. A requirement of less than 10 hits in OD within 8 m of the back-extrapolated entrance point, $EHIT_{800}$, was imposed to reject "cosmic-ray muons". Figure 4.17 shows the distribution of the number of OD hits within 8m of the

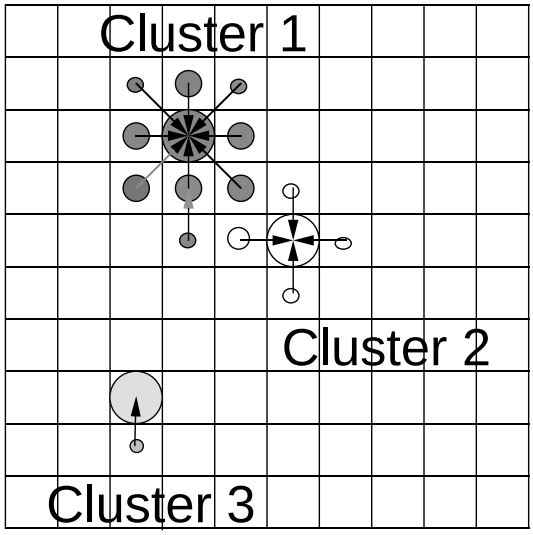

Figure 4.15: Schematic view of the clustering algorithm in the second reduction. The circles in the figure show the sum of the charge in each cluster. The arrows represent the vector charge gradient. Each arrow points the highest charge neighbor for a given angular bin. The angular grid is centered upon the anti-counter charge distribution. The angular bin sizes correspond to roughly 10 m × 10 m.

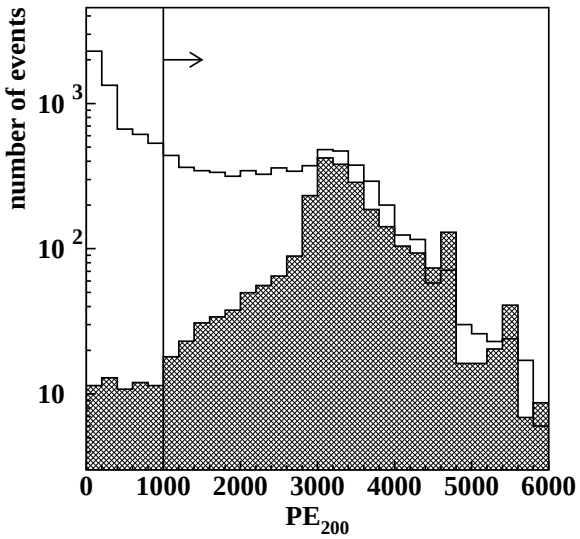

Figure 4.16: PE_{200} distributions; the white histogram for the 521 days data after the first reduction, the hatched one for the PC Monte Carlo prediction within the fiducial volume with the same livetime as data.

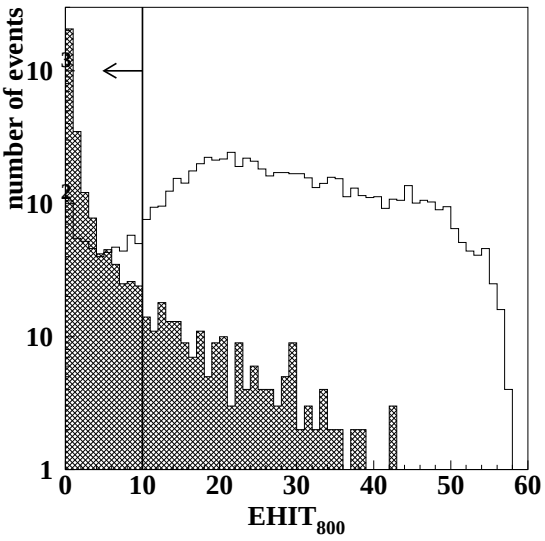

Figure 4.17: $EHIT_{800}$ distributions for 521 days data; the white histogram for the data after the second reduction, the hatched one for the PC Monte Carlo prediction. The exposure of Monte Carlo is also 521 days.

back-extrapolated entrance point for the data and PC Monte Carlo events. The event rate after the PC third reduction was about 100/day.

4.3.4 Fourth reduction

The remaining muon events after the third reduction were muons which left few entrance hits in OD. These events were rejected by the condition that the angle subtended by the earliest ID PMT hit, the vertex and the back-extrapolated entrance point to be $< 37°$.

And, to reject the remaining corner clipping muons, we required a fitted vertex to be at least 1.5 m away from the fringes of the ID volume.

Finally, Through-going muon fitter(see Sec. 4.2.3) was also applied to reject events with a well-fit muon track greater than 30 m long. The events satisfying the following events were rejected as the through-going muon.

1. *Goodness* of through-going muon > 0.85, which means this fitter can get the entrance point and the direction of the through-going muon.

2. The estimated muon track length by the entrance and exit point is grater than 30 m.

where the definition of *goodness* will be described in Sec 5.2.

The event rate after the PC firth reduction was about 20 events/day.

	fraction (%)
first	96.4
second	92.3
third	91.7
forth	88.1
firth	88.0

Table 4.1: The fraction of Monte Carlo events for PC sample within fiducial volume at each reduction step.

4.3.5 Fifth reduction

In order to further reject cosmic-ray muon entering events, an optimized automatic fitting algorithm what is called TDCfit (see 5.2) was applied. Again we required less than 10 hits in OD within 8 m of the more accurately back-extrapolated entrance point.

At this stage, we required that the total p.e. numbers of the ID should be larger than 3000 p.e. This requirement corresponded to $E \sim 350MeV$, well below that of any PC events. It was estimated that 0.1 % of the PC events in the fiducial volume were eliminated by this requirement.

Finally, we required the number of OD cluster hits >= 10 to reject FC events.

The event rate after the PC fifth reduction was 2 events/day.

4.4 Reduction performance

We applied reduction program for atmospheric neutrino MC, and checked the reduction efficiency. For FC events in the fiducial volume with $E_{vis} > 30MeV$, the reduction efficiency was estimated to be 99.87 %. On the other hand, the efficiency for PC events in the fiducial volume was estimated to be 88 %. Table 4.1 shows the fraction of Monte Carlo events for PC sample at each reduction step.

4.5 Scanning

After these software reduction steps, the candidate events were reduced to 20 and 2 events/day for FC and PC sample, respectively. All the remaining events were scanned to

category	fraction (%)
stopping μ	25.0
through-going μ	2.5
flashing PMT	69.5
noise	1.5
others	1.5

Table 4.2: Fraction of each category of the events which were rejected final scan.

be checked data quality by two physicists independently. When the detector performance was not good, for instance too many flashing events or some of the PMTs were not active, these runs (subruns) were regarded as bad-runs (bad-subruns) and were rejected. At the same time, each scanner removed the remaining background events.

After the double scan, the final scan was done to check the consistency of the double scan result and made the final data sample. Because of the double-scanning, the scanning efficiency was estimated to be better than 99%. Table 4.2 summarizes a category of the event rejected by the scan.

Finally, 12862(721) candidate events were selected as the FC(PC) data sample.

Chapter 5

Event reconstruction

5.1 Outline of reconstruction

After the event selection processes, events were reconstructed by procedures as shown in Fig 5.1. The flow of a reconstruction process was separated into two; one was a process for "fully contained" (FC) events, another was for "partially contained" (PC) events. These procedures are fully automatic. Therefore, there is no bias by a physicist in the event reconstruction procedures.

For FC events, the beginning of all processes was vertex reconstruction, called "TDC fit". Then, "Ring-counting" which estimates the number of Cherenkov rings based on a likelihood method, was applied. The next step was particle identification which distinguishes between showering electron(e)-type and non-showering muon(μ)-type. For the events identified as single-ring in the second step, a more precise fitter "MS fit" was applied. Finally, the energy of particle was estimated from the intensity of Cherenkov light.

On the other hand, PC event reconstruction involved the first vertex fitter only.

These processes are explained in this chapter.

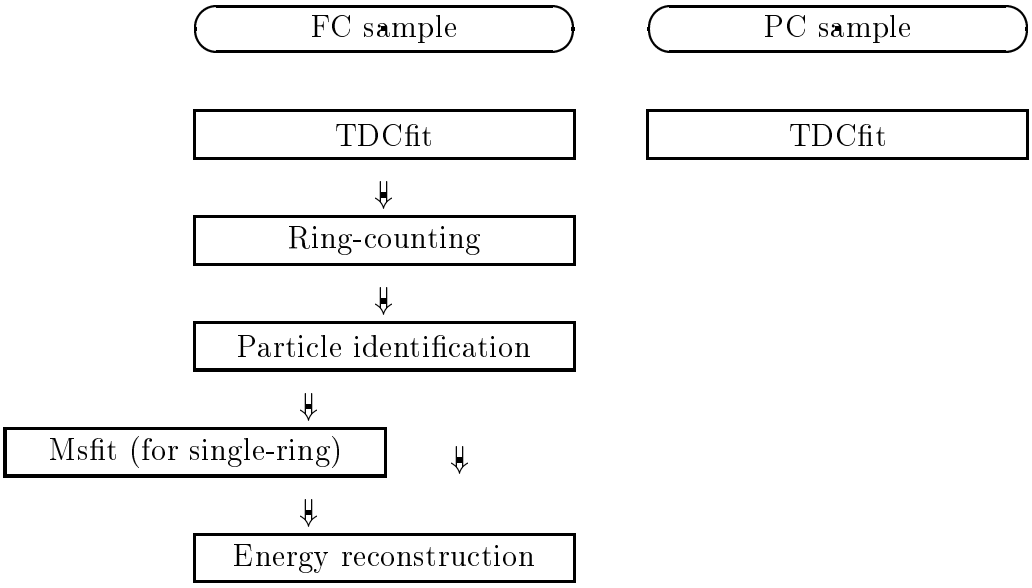

Figure 5.1: The flow chart of event reconstruction

5.2 TDCfit

The principle of spatial reconstruction tool, TDCfit, is to search for the position where the timing residuals t_i of the entire hit PMTs are equal. The timing residual t_i of the i-th hit PMT is defined as:

$$t_i = t_i^0 - (n/c) \times |\vec{P}_i - \vec{O}| - \langle t \rangle \tag{5.1}$$

where n is the refractive index of water; c is the light velocity; t_i^0 is the hit time of the i-th PMT; $\langle t \rangle$ is the average of t_i; $\vec{P}_i$ shows the position vector of the i-th PMT, and $\vec{O}$ is the position vector of an assumed vertex position of the particle. TDCfit considers the track length of the charged particle by using the total charge within a Cherenkov cone. Hence, this process needs to know the rough vertex, direction, and opening angle of the Cherenkov cone. In this process, for simplicity, it assumes that all events consist of single-ring.

TDCfit estimates the vertex, direction, and opening angle of Cherenkov ring in the following steps:

1. "Point fit", which searches for a rough vertex using only the timing information of hit PMTs,

2. "ring edge search", which searches for the direction and opening angle of the Cherenkov ring produced by the most energetic charged particle,

3. "the fine vertex fitting", which determines more precise vertex by taking account of the track length of the charged particle,

The steps 2 and 3 are iterated until the distance between the previous vertex and the latest one is less than 50 centimeters.

These three steps are described below.

5.2.1 Point fit

The principle of Point fit is to search for a position where the timing residual t_i of all the hit PMTs are approximately equal. To search for the vertex, we use goodness G_p:

$$G_p = \frac{1}{N_{hit}} \sum_i \exp\left(-\frac{t_i^2}{2\sigma^2}\right) \tag{5.2}$$

where N_{hit} is the number of hit PMTs in ID, and σ is the typical timing resolution. We use $\sigma = 3.75$ ns. Because of a technical reason, this value is larger than the actual timing resolution of PMT($\sim$ 2.5ns). It should be noticed that the definition of G_p is the sum of gaussian probabilities. This way, the contribution to G_p of scattered photons, which produce delayed signal and therefore $\exp\left(-\frac{t_i^2}{2\sigma^2}\right) \sim 0$, is minimized. The Point fit searches for the position where G_p is maximum, and its vertex resolution is about 1 meter.

After determining the vertex roughly, Point fit estimates the direction $\vec{d_p}$ defined as:

$$\vec{d_p} = \sum_i \frac{\vec{P_i} - \vec{O}}{|\vec{P_i} - \vec{O}|} \times C_i \tag{5.3}$$

where C_i is the charge of the i-th hit PMT.

5.2.2 Cherenkov edge search

This process searches for the direction and opening angle of the Cherenkov ring which maximize "Q" around the estimated direction in the previous step. The procedure involves the following steps:

1. Make the angular distribution of the effective charge "CH(θ)", where θ is the opening angle between the particle direction and Cherenkov photon direction. Figure. 5.2(a) shows CH(θ). The effective charge means the charge corrected in acceptance and water transparency. In addition CH(θ) is smoothed by taking account of the vertex resolution.

2. Obtain the opening angle of Cherenkov ring "θ_{edge}" which simultaneously satisfies the following two criteria:

   - θ_{edge} must be larger than the angle at peak position of CH(θ) (θ_{peak})
   - θ_{edge} must be the angle nearest to θ_{peak} among the angles, which satisfy $\frac{d^2\,\mathrm{CH}(\theta)}{d^2\theta} = 0$ (see Fig. 5.2(b)).

3. Calculate "Q" defined as follows:

$$Q = \frac{\int_0^{\theta_{edge}} \mathrm{CH}(\theta)d\theta}{\sin\theta_{edge}} \times \left(\left. \frac{d\,\mathrm{CH}(\theta)}{d\theta} \right|_{\theta=\theta_{edge}} \right)^2 \times \exp\left(-\frac{(\theta_{edge}-\theta_C)^2}{2\sigma_\theta^2} \right) \tag{5.4}$$

   where θ_C is the Cherenkov opening angle expected from the charge within the cone; σ_θ is the opening angle resolution.

The optimization was carried out by changing the particle direction. The particle direction and θ_{edge}, which maximize Q, were adopted as the final ones.

5.2.3 Final vertex fitter

After the Cherenkov edge search, we determine the vertex position more precisely by considering the scattered Cherenkov light and the particle track length. Two goodnesses,

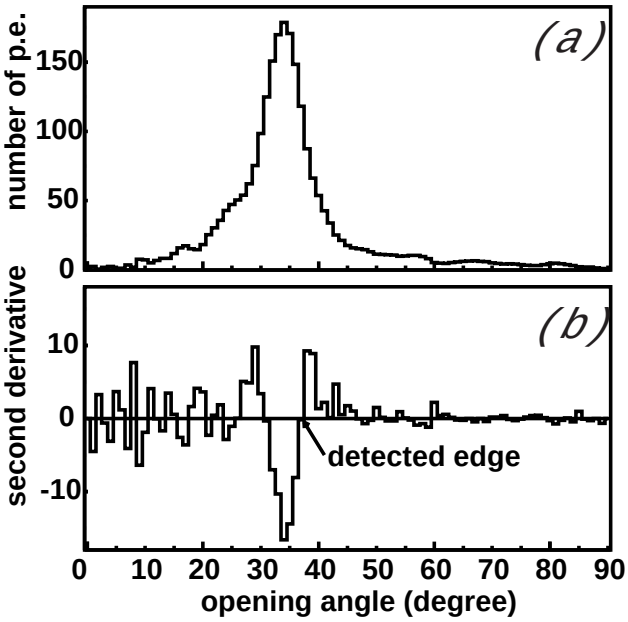

Figure 5.2: The CH(θ) distributions; (a) for the $CH(\theta)$ distribution, (b) the second derivative of CH(θ).

G_I and G_O are used. G_I is the goodness calculated using the PMTs which are located in the Cherenkov ring obtained in "Cherenkov ring edge search". The definition of G_I is;

$$G_I = \sum_i \frac{1}{\sigma_i^2} \exp\left(-\frac{t_i^2}{2\sigma^2}\right) \tag{5.5}$$

where σ_i is the timing resolution of the i-th PMT, which is a function of its charge.

G_O is the goodness for the remaining hit PMTs, which are considered to be hit by either direct and/or scattered photons.

$$G_O = \sum_i \frac{1}{\sigma_i^2} \times max\left[\exp\left(-\frac{t_i^2}{2\sigma^2}\right), 0.8 \times \exp\left(-\frac{t_i}{T_l}\right)\right] \tag{5.6}$$

where T_l is the typical timing delay of scattered photons. It was estimated by a Monte Carlo study, and is set to be 20 ns.

Finally, G_T is defined as

$$G_T = \frac{G_I + G_O}{\sum_i \frac{1}{\sigma_i^2}} \tag{5.7}$$

where $\sum_i 1/\sigma_i^2$ is a factor to normalize G_T from 0 to 1.

Next, the tack length of particle is considered as follows:

1. Estimate the total track length "L_t" from the total charge within a cone of 70° half opening angle

2. Recalculate t_i for PMTs, which are located in the Cherenkov ring, by taking account of the particle velocity (which is assumed to be the light velocity) and position along the track where Cherenkov photons are emitted.

3. Calculate G_I using the corrected t_i

These procedures are iterated several times and finally the vertex position and direction which maximize G_T are determined as best fit points. Figure 5.3 shows the Δpos distribution for the FC, PC, π°, and multi-rings events, where Δpos is the distance between the reconstructed and the real vertex position. Defining the vertex resolution as the distance where the 68% of events are found within Δpos, the resolutions are 55cm, 94cm, 42cm, and 52cm for FC, PC, $\pi\circ$, and multi-rings events. The vertex potion determined by this process is the final vertex potion for multi-ring events.

5.3 Ring-counting

After the reconstruction of the vertex position, direction and opening angle of the most energetic Cherenkov ring, we tried to find other Cherenkov rings and determine whether the event is a singe or multi-ring event. The number of Cherenkov rings is a very important information, since it is used in various atmospheric neutrino analyses. The Ring-counting process counts the number of rings and estimates the direction and opening angle of the found rings. The algorithm of Ring-counting is:

1. Make a special "charge map".

2. Search a candidate direction using the charge map.

3. Determine whether the candidate is true or not by a likelihood method using charge pattern of hit PMTs.

4. If a new ring is found, go back to the first step to search for another ring.

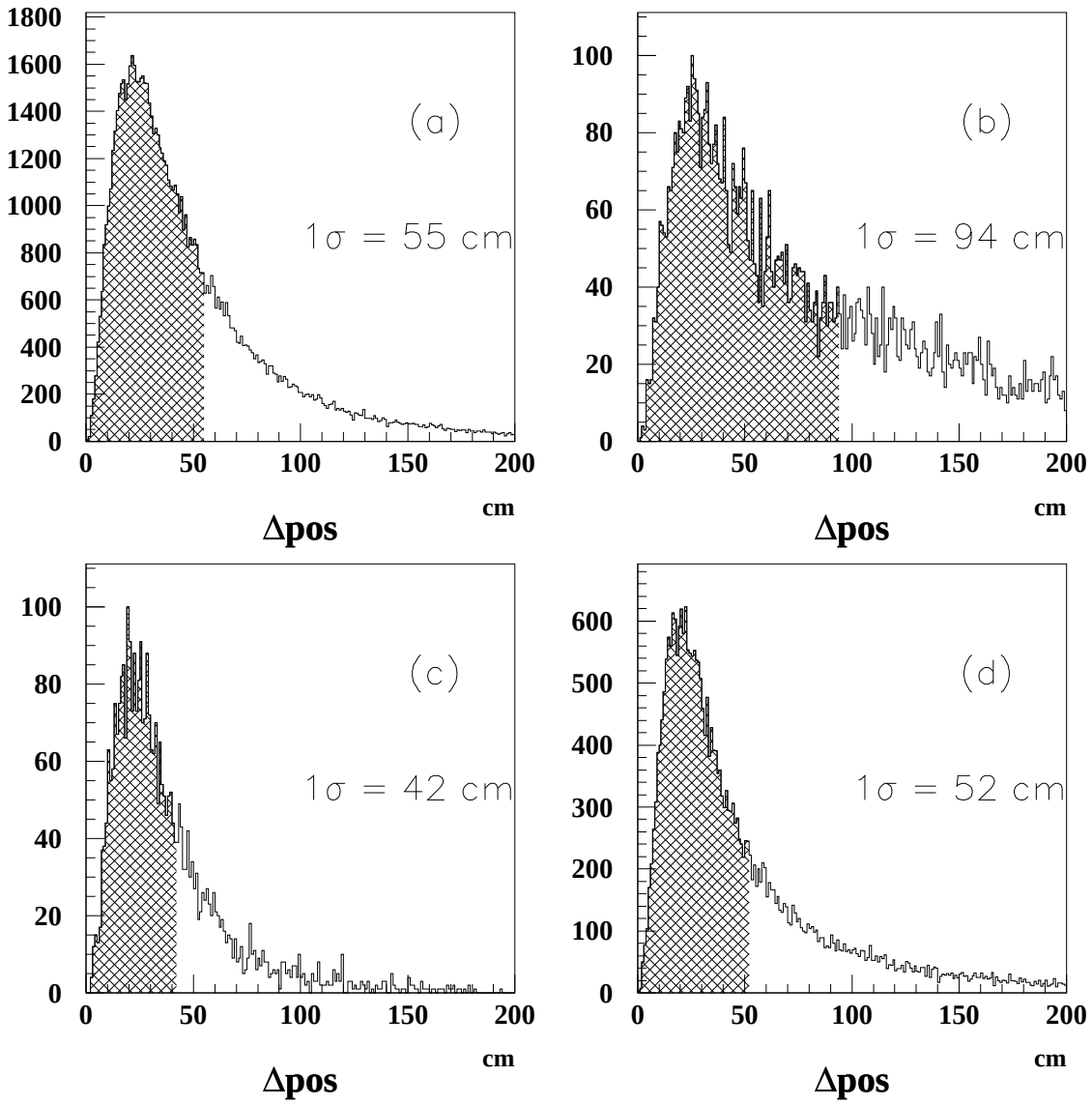

Figure 5.3: The Δpos distributions; (a) for the FC, (b) for the PC, (c) for the $\pi\circ$, and (d) for the multi-rings events. The hatched area corresponds to 68% of the total events.

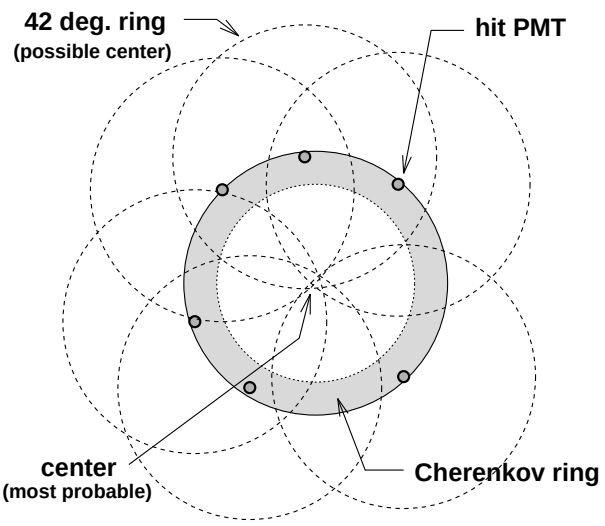

Figure 5.4: Basic idea of the "charge map". The ring at the center shows the Cherenkov ring; the small circles on the center ring are hit PMTs; The dashed circles are the circles with the same radius as the observed Cherenkov ring with their centers on the each hit PMT. The crossing point of each dashed circle should be the center of the Cherenkov ring.

This process searches for Cherenkov rings up to five. The detail of each part is described below.

5.3.1 Search for candidate rings

Figure 5.4 illustrates the basic concept of the search for candidate rings. Assume we observe a Cherenkov ring on a flat plane. If we draw circles on this plane with the center at the position of the hit PMTs and with the radius same as the observed radius of the Cherenkov ring, we find that the circles overlap at the center of the Cherenkov ring. Therefore, a point where the maximum overlapping of the circles can give the information of the particle direction.

In the real situation, first, we subtract the expected charge of found rings from each hit PMTs, in order to efficiently find the rings produced by low energy particles. Then Ring-counting process makes a special "charge map", which is a 2-dimensional array with 72 bins for azimuth angle and 36 bins for zenith angle. Each bin corresponds to a direction from the vertex position obtained by the TDCfit. The charge of hit PMT is distributed to each bin with an weight of the PE(θ). This PE(θ) shows the charge distribution of an electron event, and is a function of θ which is the opening angle between the bin direction and the PMT direction. This way of making charge map corresponds to drawing circles

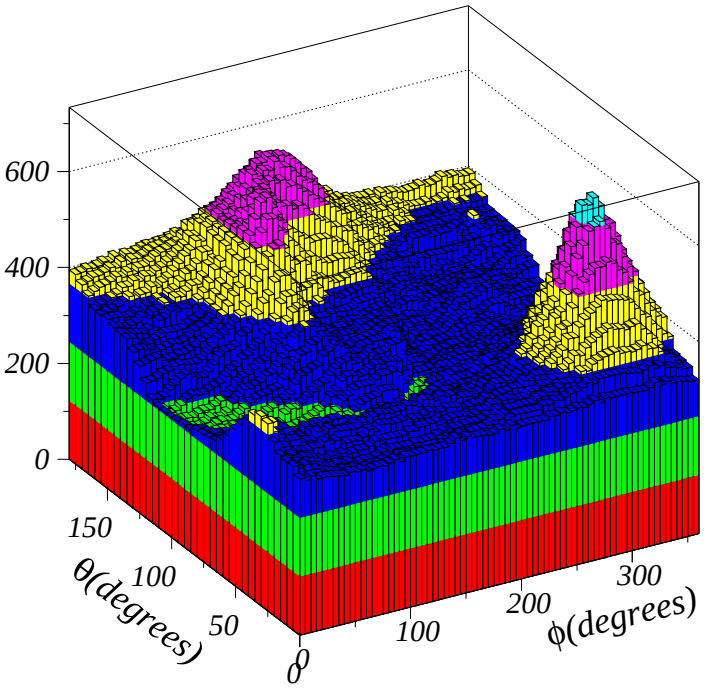

Figure 5.5: The charge map of a typical two ring event. This is a 2-dimensional array with 72 bins for azimuth angle and 36 bins for zenith angle. Each bin corresponds to the direction from the vertex. Two peaks correspond to the directions of the Cherenkov rings from the vertex position.

on the flat plane described above. Figure 5.5 shows the "charge map"[1] of a typical two ring event. Two peaks on the map correspond to the direction of each ring.

5.3.2 Charge separation and determination of ring number

Let n be the number of rings already observed in an event. To determine whether the additional candidate ring is a real Cherenkov ring or not, we carry out the following procedures.

First, we define the expected charge distribution of the j-th ring, $C_{ring,exp}(j,p,\theta)$, where p is the expected momentum of the particle corresponding to the j-th ring, and θ is the angle from the direction of the particle. At the first stage, the expected charge of the ring $C_{ring,exp}(j,p,\theta)$ is calculated on the assumption that all particles are electrons. Then the expected charge, $C_{exp}(i,j)$, from the j-the ring at the i-th PMT is calculated:

$$C_{exp}(i,j) = \alpha(i) \times C_{ring,exp}(j,p,\theta) \tag{5.8}$$

where α is a conversion factor correcting for acceptance, distance from the vertex position to the PMT and the attenuation of the Cherenkov light. Then the expected charge from

[1] This map is made without subtracting the charge of the first ring.

all rings to the i-th PMT is:

$$C_{sum,exp}(i) = \sum_{j=1}^{n} C_{exp}(i,j) \tag{5.9}$$

Then we defined a likelihood:

$$L(j) = \sum_{i} \ln\left(prob(C_{obs}(i), C_{sum,exp}(i)) \times \sqrt{C_{exp}(i,j)}\right. \tag{5.10}$$

where $C_{obs}(i)$ is the observed charge for the i-th PMT. The function *prob* calculates the probability that the observed value is C_{obs} when the expected one is C_{exp}. Its definition is:

$$prob(C_{exp}, C_{obs}) = \begin{cases} \text{Poisson distribution} & \\ \text{corrected for single p.e. distribution} & (C_{obs} \leq 20 p.e.) \\ \frac{1}{\sqrt{2\pi}\sigma} \exp\left(-\frac{1}{2}\left(\frac{C_{exp}-C_{obs}}{\sigma}\right)^2\right) & \\ \sigma = \sqrt{1.2^2 \times C_{exp} + (0.1 \times C_{exp})^2} & (C_{obs} > 20 p.e) \end{cases} \tag{5.11}$$

where the factor 1.2 comes from the result of a comparison between the real charge resolution of PMTs and poison statistics; and the factor 0.1 is derived from the uncertainty of the relative gain calibration of the PMT. The factor $\sqrt{C_{exp}(i,j)}$ in Eq. 5.10 enhances the contribution from PMTs around the expected Cherenkov ring positions. We change the total charge of the j-th Cherenkov ring so that $L(j)$ is maximized. This way, the best fit total charge for each Cherenkov ring is determined.

It is possible to estimate the contribution of the j-th ring to the observed charge by the i-th PMT:

$$C_{obs}(i,j) = C_{obs}(i) \times \frac{C_{exp}(i,j)}{C_{sum,exp}(i)} \tag{5.12}$$

Now by using $C_{obs}(i,j)$, it is possible to re-estimate $C_{ring,exp}(j,p,\theta)$. Then we repeat the same procedure by using new $C_{ring,exp}(j,p,\theta)$. This way, the total charge for each Cherenkov ring is determined essentially independent of the initial assumption of the electron-rings.

Now, we define that $L_{max}(n)$ is the maximum likelihood of Eq. 5.10 for n-ring assumption. Then $L_{max}(n) \times W(n)$ is used to determine the number of rings, where $W(n)$

is an empirical weight as a function of the opening angle among the each ring direction. In a same way, $L(n+1) \times W(n+1)$ is calculate using the additional candidate ring. If the $L(n) \times W(n)$ is greater than $L(n+1) \times W(n+1)$, Ring-counting process determine the number of ring as n, otherwise the process goes back to the step 1 to search for another ring.

Finally, we show a performance of Ring-counting by using Monte Carlo events. Here we used the charged current quasi-elastic (CC q.e.) interaction events and neutral current single π° (NC π°) interaction events to estimate the performance, because CC q.e. (NC π°) events are expected to be identified as single-ring(two-ring) events.

The fraction of CC q.e. events which are identified as single-ring events is 93.8 %. The reasons that some CC q.e. events are identified as multi-ring events are the followings.

1. A high momentum recoil proton makes Cherenkov lights, which is identified second ring(2.4 % of CC q.e. events).

2. An outgoing lepton is misidentified as two-ring event(3.8 % of CC q.e. events).

For the NN π° events, the fraction of two-ring events is $\sim$ 60 %. This fraction strongly depends on the π^0 momentum. Figure B.2 in Appendix B shows the probability of identifying two Cherenkov rings as a function of π° momentum. The detail of π° analysis will be described in Appendix B.

5.4 Particle identification

A particle identification (PID) process makes use of the pattern and opening angle of the Cherenkov ring. Figure 5.6 shows typical events of e- and $\mu - like$ events. This figure shows that muons produce shape Cherenkov edges. In contract to this, electrons produce electro-magnetic showers and low-energy electrons in particular exhibit many multiple scattering and produce rather diffuse Cherenkov rings.

For low momentum particles, information of the opening angle, θ_C, is important, because $\cos\theta_c$ is equal to $1/(n\beta)$. The PID process determines a particle type in the following steps:

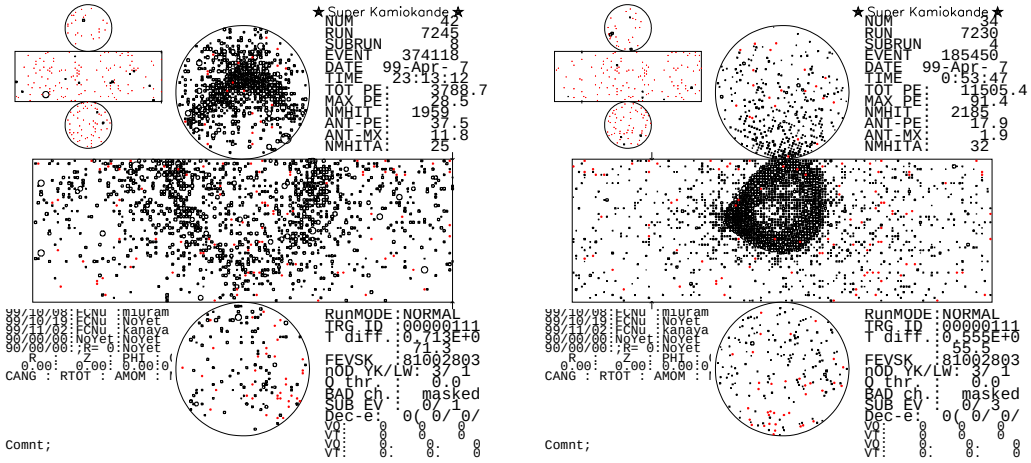

Figure 5.6: Typical FC single ring events. The left figure is for $e-like$, and the right one is for $\mu-like$.

1. estimate the intensity of direct light for each PMT for e-like and μ-like assumptions,

2. estimate the scattered light,

3. estimate the particle type.

These steps are described below.

5.4.1 Estimate the direct photon

At first, the PID algorithm estimates the intensity of the direct photon for each PMT under the assumption of an electron ring. We made the Monte Carlo simulation for electron events with momentum 100 MeV/c, 300MeV/c, and 1000MeV/c with perfect water transparency. Then we estimated the photo-electron number received in a circular area of 50 cm diameter (equal to PMT photosensitive area) located on a sphere of 16.9 m in radius. Since the Cherenkov photons are emitted in a cone, we averaged this photo-electron number as a function of an angle between the circular area and the particle direction, θ. Let $C_{MC}(\theta, p_e)$ be the average charge for electron events with their momentum p_e.

The expected number of photo-electrons in the i-th PMT produced by an electron is

expressed as:

$$C_{e,exp}(direct,i) = \alpha_e \times C_{MC}(\theta, p_e) \times \left(\frac{16.9m}{l_i}\right)^{1.5} \times \exp\left(-\frac{l_i}{L}\right) \times f(\theta_i) \qquad (5.13)$$

where α_e is the normalization factor; l_i is a distance from the particle position to the i-th PMT; θ_i is the angle of the i-th PMT from the particle direction; L is the light attenuation length. $f(\theta)$ is the effective photo-sensitive area of the PMT (see Fig. 3.2). The power index, 1.5, was estimated by a Monte Carlo study.

Next we explain the way of the estimation of the intensity of the direct photons for the μ-like assumption. For μ-like events, the expected number of photo-electrons in the i-th PMT can be calculated numerically by the following equation:

$$C_{\mu,exp}(direct,i) = \left(\alpha_\mu \times \frac{1}{l_i\left(\sin(\theta_i) + l_i\frac{d\theta}{dx}\right)} \times \sin^2(\theta_i) + C_{\mu,knock,exp}(i)\right) \times \exp\left(-\frac{l_i}{L}\right) \times f(\theta_i) \qquad (5.14)$$

where α_μ is a normalization factor; $l_i(\frac{d\theta}{dx})$ comes from the ionization energy loss of the muon; As shown in Fig. 5.7, $\sin\theta dx + l d\theta$ takes into account the change in the photon density which is caused by the change in θ, corresponding to the energy loss. $\sin^2\theta_i$ expresses the intensity variation of the Cherenkov photons. The $C_{knok,exp}(i)$ shows the number of the expected photons from the knock-on electrons as a function of θ_i which is estimated by a Monte Carlo study.

5.4.2 Estimate the scattered lights

Scattered photon can be separated from the direct Cherenkov photons by checking its arrival time. We first pick up hit PMTs within a cone having an opening angle of $1.5 \times \theta_C$, which θ_C is the reconstructed Cherenkov opening angle. This aims to eliminate accidental hits which lie mostly outside he Cherenkov cone. Then a histogram of timing residuals, t_i, is made for all the selected PMTs. Scattered photons are selected with the following criterion:

$$\begin{aligned} t_{peak} - 30nsec < t_i \leq t_{peak} + 2\sigma_i + 5nsec \quad &\longrightarrow \quad \text{direct photons} \\ t_{peak} + 2\sigma_i + 5nsec < t_i \quad &\longrightarrow \quad \text{scattered photons} \end{aligned} \qquad (5.15)$$

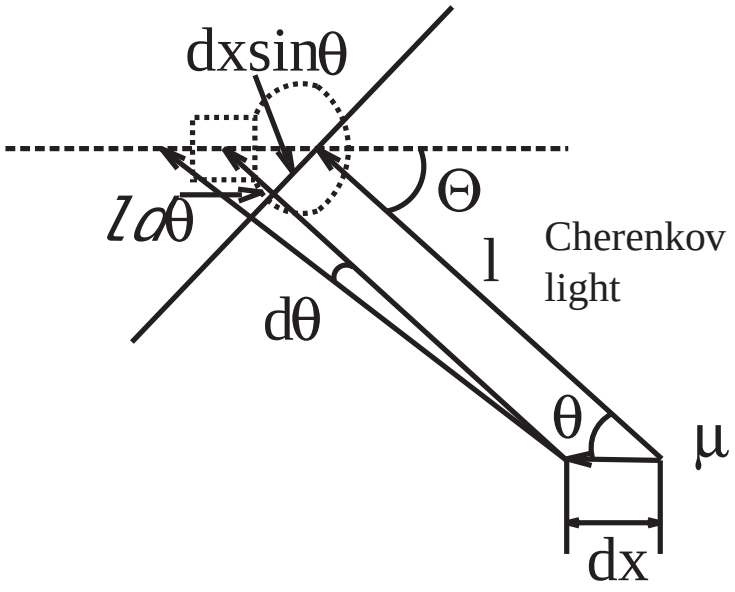

Figure 5.7: Relation between the PMT and Cherenkov photon.

where t_{peak} is the peak in the timing histogram and σ is the timing resolution of the i-th PMT as a function of the detected number of photons.

The number of photons originating from the scattered photons, $C_{exp}(scatter, i)$ is estimated from the information of the attenuation length and the distance between the vertex position and the PMTs which detect Cherenkov photons. Thus the expected number of photons for the i-th PMT is given by adding both contributions:

$$C_{e\ or\ \mu,exp}(i) = C_{e\ or\ \mu,exp}(direct, i) + C_{exp}(scatter, i) \tag{5.16}$$

5.4.3 Estimate particle type

We now define a likelihood function for PID, $L_{e\ or\ \mu}$ as:

$$L_{e\ or\ \mu} = \prod_{\theta_i < 1.5 \times \theta_C} Prob_{e\ or\ \mu}(i) \tag{5.17}$$

where $Prob_{e\ or\ \mu}(i)$ is the probability function for the i-the PMT, which is expressed in two different ways, according to whether the PMT is hit by direct or scattered photons.

$$Prob_{e\ or\ \mu}(i) = \begin{cases} prob(C_{e\ or\ \mu,exp}(i), C_{obs}(i)) & \text{direct photons} \\ prob(C_{e\ or\ \mu,exp}(direct, i), 0) & \\ \times prob(C_{exp}(scatter, i), C_{obs}(i)) & \text{scatted photons} \end{cases} \tag{5.18}$$

where *prob* is the same function as in Eq. 5.11.

In order to combine the information of the Cherenkov opening angle with the information of the ring pattern, L_x is transformed into the χ^2 distributions:

$$\chi^2(e\ or\ \mu) = -2\ln(L_{e\ or\ \mu}) - constant. \tag{5.19}$$

If the degree of freedom, N_D, exceeds 30, which is normally the case, the sigma of the χ^2 distribution, σ_{χ^2}, is approximated as:

$$\sigma_{\chi^2} = \sqrt{2N_D} \tag{5.20}$$

In this case, N_D is the number of PMTs within the $1.5 \times \theta_C$. Then the probabilities by using Cherenkov pattern can be rewritten as:

$$P_{pattern}(e\ or\ \mu) = \exp\left(-\frac{1}{2}\left(\frac{\chi^2(e\ or\ \mu) - \min(\chi^2(e), \chi^2(\mu))}{\sigma_{\chi^2}}\right)^2\right) \tag{5.21}$$

Next, the Cherenkov angle will be considered. From the reconstructed momentum and particle type we can calculate the expected Cherenkov angle, $\theta_{exp}(e \text{ or } \mu)$. If the reconstructed Cherenkov opening angle is given as $\theta_{obs} \pm \delta\theta$, the probability is derived as:

$$P_{angle}(e\ or\ \mu) = \exp\left(-\frac{1}{2}\left(\frac{\theta_{exp}(e\ or\ \mu) - \theta_{obs}}{\delta\theta}\right)^2\right) \tag{5.22}$$

Combining Eq. 5.21 and Eq. 5.22, the probability P_{PID} is given by

$$P_{PID}(e\ or\ \mu) = P_{pattern}(e\ or\ \mu) \times P_{angle}(e\ or\ \mu) \tag{5.23}$$

A ring with $P_{PID}(\mu) > (<) P_{PID}(e)$ is identified as μ-like(e-like). We shows the performance of particle identification using CC p.e. events. Figure 5.8 shows a $\sqrt{P_{PID}(\mu)} - \sqrt{P_{PID}(e)}$ distribution of CC q.e. interaction events which were identified as single-ring events. This figure illustrates that our particle identification is very good for CC q.e. events. The misidentification probability of the particle identification is 0.5 and 0.8 % for $CC\ \nu_e$ and $CC\ \nu_\mu$ events, respectively.

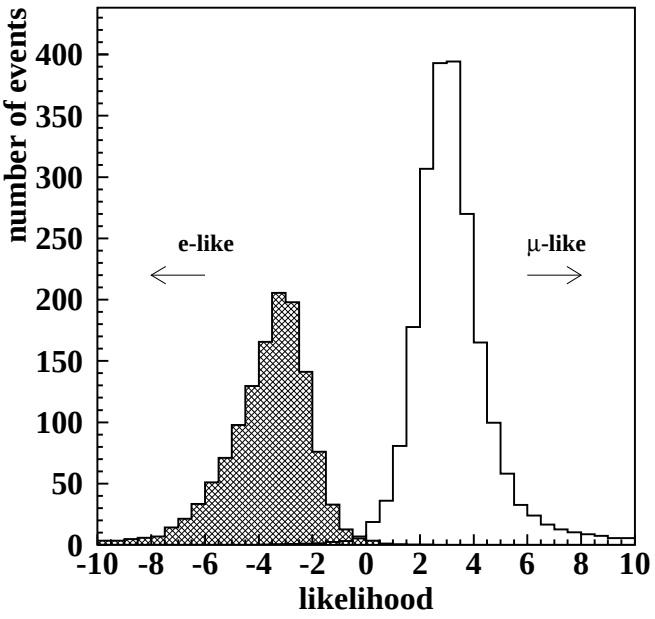

Figure 5.8: $\sqrt{P_{PID}(\mu)} - \sqrt{P_{PID}(e)}$ distribution for CC q.e. single-ring events; the white histogram for CC ν_μ, and the hatched one for CC ν_e.

5.5 MS fit

The vertex resolution of TDCfit for single-ring events is relatively poor compared with that of multi-rings events. This reason comes from the facts that a fitter using timing information is not sensitive in the longitudinal direction of a Cherenkov ring, and its vertex shift in the longitudinal direction depends on the particle type. Therefore, we use another fitter, which obtains the vertex position using the charge pattern information, for FC single-ring events to improve its vertex resolution. This fitter is called "MS fit".

At this stage, we already know the particle type, which means that we can estimate charge pattern distribution. MS fit moves the vertex position parallel to the particle direction, to search for the position where the observed charge distribution and the expected one match the best. The comparison is carried out based on the likelihood defined in PID. Then it adjusts the direction where the above likelihood gives the maximum. Next, it looks for the vertex position with the maximum goodness used in the TDC fit, shifting the vertex perpendicular to the particle direction. MS fit iterates these three steps until the change of vertex and direction relative to the previous ones is less than 5 cm and 0.5°, respectively.

The performance of MSfit is estimated using the Monte Carlo study and cosmic-ray muons. In the Monte Carlo study, we use the atmospheric neutrino events identified

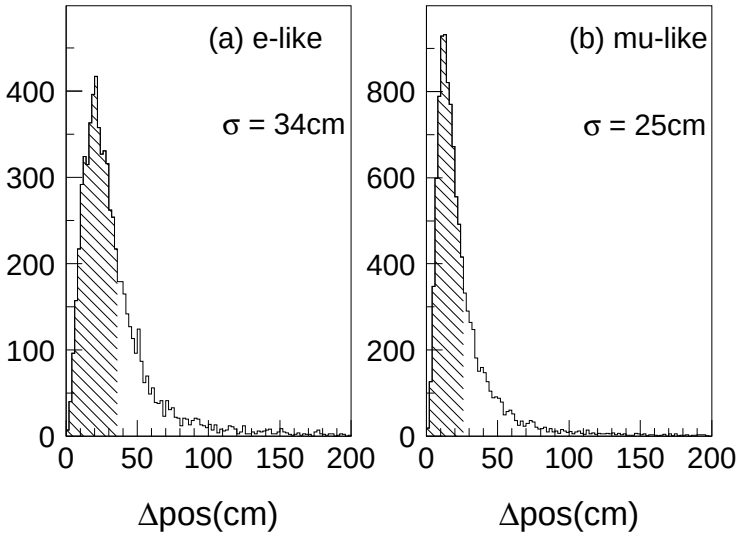

Figure 5.9: The vertex resolution of MSfit. The hatched histogram shows the events within 1 σ vertex position resolution.

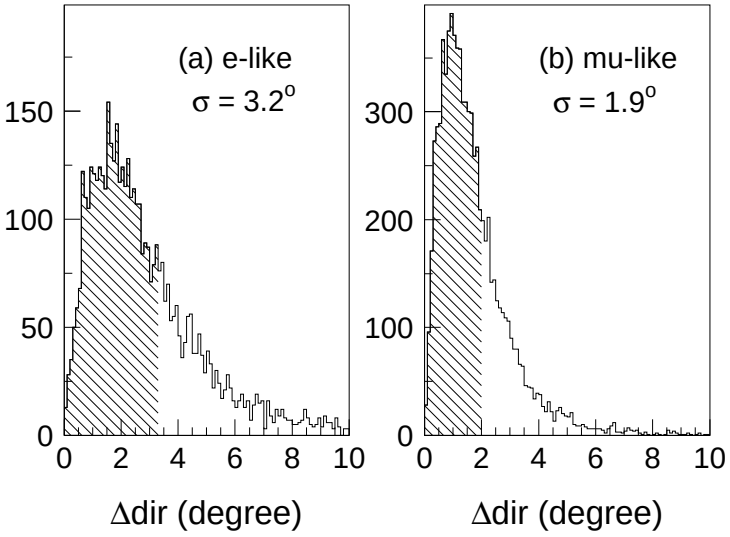

Figure 5.10: The angular resolution of MSfit. The hatched histogram shows the events within 1 σ angular resolution.

as a single-ring event by Ring-counting. Figure 5.9 represents the distribution of the distance between the fitted and the real vertex. Let the vertex resolution be the distance where 68% of events are covered. Figure 5.9 shows that the vertex resolution of MSfit is 34 and 25 centimeters for e-like and μ-like events, respectively. Figure 5.10 shows the distribution of opening angle between the fitted and real direction. From this figure, the angular resolution is 3.2° for e-like events and 1.9° for μ-like events, where the angular resolution is defined in the same way as for the vertex.

5.6 Momentum estimation

In order to estimate the momentum, we use the corrected total charge R_{tot}. To reduce the scattered light effect, we use the PMTs satisfying the following criteria:

- Select the PMT whose opening angle from the particle direction is less than 70°
- select the PMT which satisfy: $t_{peak} - 50(ns) < t_i < t_{peak} + 250(ns)$

The R_{tot} is corrected for the PMT acceptance and water transparency and its definition is:

$$R_{tot} = \frac{G_{MC}}{G}\left[\alpha_R \sum_{\substack{\theta_i<70^\circ \\ -50<t_{res}<250}} C_{obs}(i) \times \frac{\cos\Theta_i}{f(\Theta_i)} \times \exp\left(-\frac{l_i}{L}\right) - \sum_{\theta_i<70^\circ} C_{exp}(scatter, i)\right] \tag{5.24}$$

where $G(G_{MC})$ is a relative PMT gain of data (MC), α_R is normalization factor, t_{res} is a time from the peak of time residual, θ_i is an opening angle between the i-th PMT direction from the vertex position and the particle one, Θ_i is angle of photon arriving direction relative to the i-th PMT facing direction, and L is the attenuation length of light in the water. Figure 5.11 (a) shows the relation between R_{tot} and momentum which is obtained from a Monte Carlo study. The momentum resolution, σ_p, of each particle is shown in Fig. 5.11 (b). From this figure, σ_p at low momentum regions ($P \lesssim 2.0 GeV/c$) is approximately calculated as:

$$\sigma_p = \begin{cases} 0.6 + \frac{2.6}{\sqrt{p}}\% & \text{(for electrons)} \\ 1.7 + \frac{0.7}{\sqrt{p}}\% & \text{(for muons)} \end{cases} \tag{5.25}$$

where p is the momentum of each particle in GeV/c.

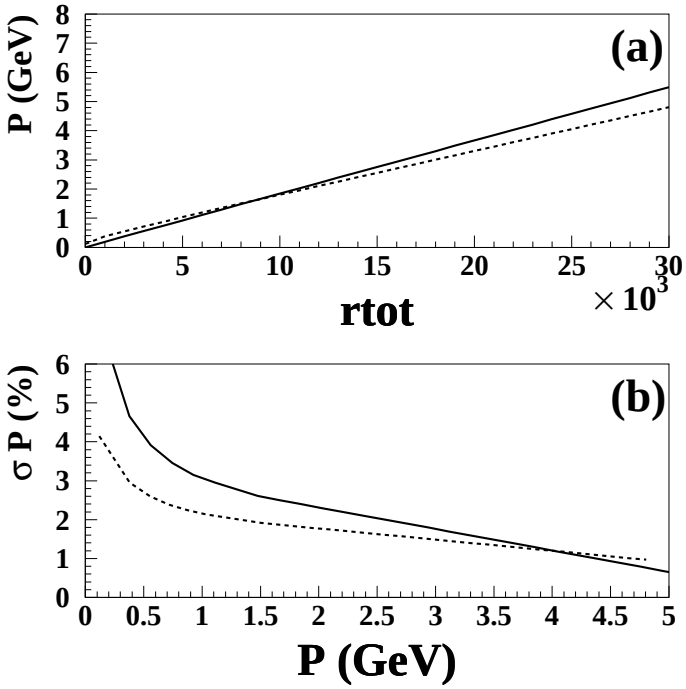

Figure 5.11: The reconstructed momentum by using R_{tot}. (a) shows a reconstructed momentum, p, as function of R_{tot}. (b) shows a momentum resolution, σ_p, as function of p. Solid (broken) line shows e (μ)-like events.

Chapter 6

Monte Carlo simulation

In this analysis, we use a Monte Carlo simulation to predict various numbers and distributions. In addition, the estimations of several criteria for reduction and reconstruction arise from Monte Carlo studies. Therefore the Monte Carlo simulation plays a vital role. Our Monte Carlo separates into the neutrino interaction and a detector simulation.

6.1 Atmospheric neutrino flux

Several persons have calculated the atmospheric neutrino flux. Here we use the Honda *et al*'s calculation [13], because their flux model considers the magnetic latitude of the Kamioka site and covers the neutrino energy from 10 MeV to 1 TeV. In order to estimate the systematic errors coming from the neutrino flux, we use the Bartol's flux [14], which is also calculated taking into account the magnetic cut-off at Kamioka. The discrepancy of the calculated neutrino flux between these two models is less than $\pm 10\%$. The uncertainty of the absolute flux of the atmospheric neutrino is estimate to be $\sim 25\%$.

6.2 Neutrino interaction

Our Monte Carlo considers the following neutrino interactions:

- Charged Current quasi-elastic scattering ($\nu\ N \rightarrow l\ N'$)
- Neutral Current elastic scattering ($\nu\ N \rightarrow \nu\ N$)

- Charged Current single π production ($\nu\ N \to l\ N'\ \pi$)
- Neutral Current single π production ($\nu\ N \to\ \nu\ N'\ \pi$)
- Charged Current coherent π production ($\nu\ ^{16}O \to l^{\pm}\ ^{16}O\ \pi^{\mp}$)
- Neutral Current coherent π production ($\nu\ ^{16}O \to\ \nu\ ^{16}O\ \pi^{\circ}$)
- Charged Current multi π production ($\nu\ N \to l\ N'\ n\pi$)
- Neutral Current multi π production ($\nu\ N \to\ \nu\ N'\ n\pi$)

where N and N' are the nucleons; l is the charged lepton; n is the multiplicity of pions. The probability of the other interaction modes is too small compared to the above interactions, therefore we neglect them in this simulation. We have checked the total cross section in each mode with the real data [67]. The momentum distribution of outgoing lepton, and the angular distribution have been compared with the data from the BNL[1] 7-foot bubble chamber by Hasegawa [68]. Each interaction is presented in this chapter. Then the comparisons with the real data and the Monte Carlo prediction are presented.

6.2.1 Quasi-elastic scattering

In the calculation of the cross section for the charged current quasi-elastic interaction, $\nu + n \to l^- + p$, the differential cross section is written [69]:

$$\frac{d\sigma}{dq^2} = \frac{M^2 G^2 \cos^2\theta_c}{8\pi E_\nu^2}\left[A(q^2) \mp B(q^2)\frac{s-u}{M^2} + C(q^2)\frac{(s-u)^2}{M^4}\right] \tag{6.1}$$

where q is a square of the 4-momentum transfer of lepton, s and u are Mandelsam variables, E_ν is a neutrino energy, M is a target nucleon mass, θ_c is Cabibbo angle, and G is

[1] Brookheaven National Laboratory

Fermi coupling constant. $A(q^2), B(q^2)$, and $C(q^2)$ is written as the following:

$$\begin{aligned} A(q^2) &= \frac{m^2-q^2}{4M^2}\left[\left(4-\frac{q^2}{M^2}\right)|F_A|^2-\left(4+\frac{q^2}{M^2}\right)|F_V^1|^2\right. \\ &- \left.\frac{q^2}{M^2}|\xi F_V^2|^2\left(1+\frac{q^2}{4M^2}\right)-\frac{4q^2F_V^1\xi F_V^2}{M^2}-\frac{m^2}{M^2}\left((F_V^1+\xi F_V^2)^2+|F_A|^2\right)\right] \\ B(q^2) &= \frac{q^2}{M^2}\left(F_A(F_V^1+\xi F_V^2)\right) \\ C(q^2) &= \frac{1}{4}\left(|F_A|^2+|F_V^1|^2-\frac{q^2}{4M^2}|\xi F_V^2|^2\right) \end{aligned} \tag{6.2}$$

where m is a lepton mass, and $\xi = 3.71$. The vector form factor, F_V^1 and F_V^2 are explained by:

$$\begin{aligned} F_V^1(q^2) &= \left(1-\frac{q^2}{4M^2}\right)^{-1}\left(1-\frac{(1+\xi)q^2}{4M^2}\right)\left(1-\frac{q^2}{M_V^2}\right)^{-2} \\ F_V^2(q^2) &= \left(1-\frac{q^2}{4M^2}\right)^{-1}\left(1-\frac{q^2}{M_V^2}\right)^{-2} \end{aligned} \tag{6.3}$$

In our Monte Carlo, M_V is set to be 0.84 GeV/c^2. The axial vector form factor F_A is experimentally obtained as the follow:

$$F_A(q^2) = -1.23\left(1-\frac{q^2}{M_A^2}\right)^{-2} \tag{6.4}$$

The uncertainty of M_A is large, and various experiments suggested 0.9 $GeV/c^2 \lesssim M_A \lesssim$ 1.1 GeV/c^2 [70]. We adopt $M_A = 1.01GeV$ in our Monte Carlo. In the case of free proton target, the total cross section is directly determined from Eq. (6.1). Figure 6.1 shows the calculated cross sections and the real data in $\nu_\mu n \to \mu^- p$ and $\bar{\nu_\mu} p \to \mu^+ n$. Figure 6.2 shows the q^2 distribution for $\nu_\mu n \to \mu^- p$, and this figure proofs the reproducibility of our Monte Carlo.

On the other hand, in the case that the target is a nucleon in Oxygen, we take account of nuclear effects such as Pauli blocking and Fermi motion of the nucleon. For the Pauli blocking, we request the momentum of the recoil nucleon should exceed the Fermi surface momentum. Fermi motion is adopted based on the Fermi gas model on the assumption that 4 nucleons are in the 1s states and 12 nucleons are in 1p states.

We also consider the neutral current elastic interaction. The cross section for NC

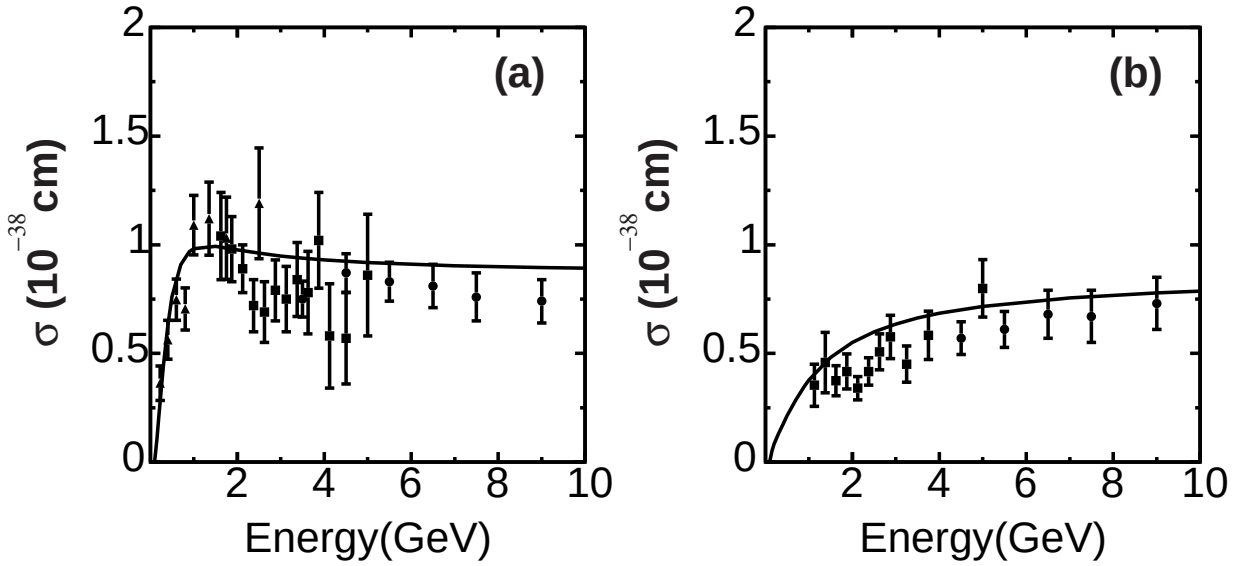

Figure 6.1: The calculated cross section of quasi-elastic interactions compared with the experimental data; (a) for $\nu_\mu n \to \mu^- p$, (b) for $\bar{\nu_\mu} p \to \mu^+ n$. triangle: ALN [71], square: GGM77 [72], circle: Serpukhov [73].

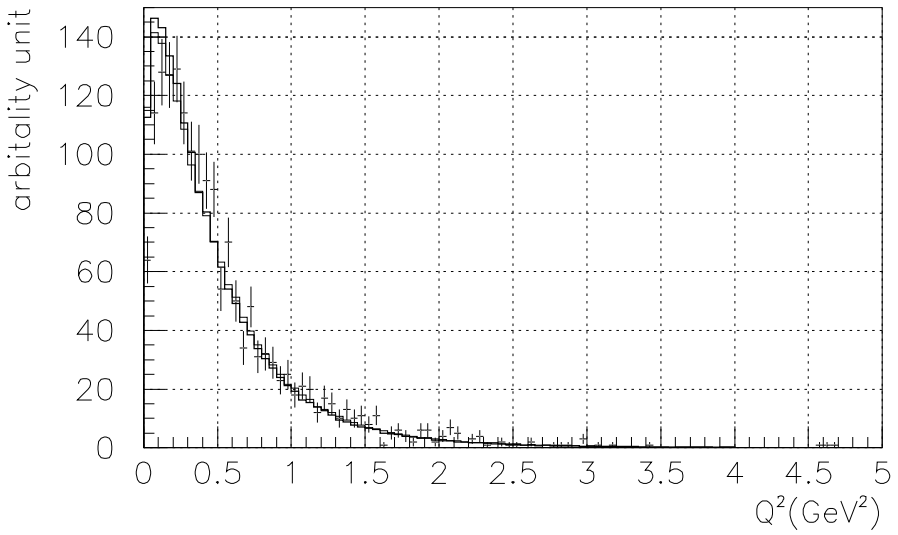

Figure 6.2: The q^2 distribution for $\nu_\mu n \to \mu^- p$. The histogram shows the Monte Carlo result, and the points with error bars shows the experimental data from BNL [74].

elastic scattering is evaluated using the relation [75, 76]:

$$\begin{aligned}
\sigma(\nu p \to \nu p) &= 0.153 \times \sigma(\nu n \to e^- p), \\
\sigma(\bar{\nu} p \to \bar{\nu} p) &= 0.218 \times \sigma(\bar{\nu} p \to e^+ n), \\
\sigma(\nu n \to \nu n) &= 1.5 \times \sigma(\nu p \to \nu p), \\
\sigma(\bar{\nu} n \to \bar{\nu} n) &= \sigma(\bar{\nu} p \to \bar{\nu} p)
\end{aligned} \tag{6.5}$$

6.2.2 Single pion production

Here "single pion production" is defined as the interaction which makes single pion produced via the baryon resonance states as follows:

$$\begin{aligned}
\nu + N \to l + \quad & N^* \\
& N^* \quad \to \pi N'
\end{aligned}$$

where N and N' are the nucleon, N^* is the baryon resonance(N and Δ). In addition, to be consistent with multi pion productions(see sec 6.2.4), it is restricted to the interaction whose hadronic invariant mass W is less than 2.0 GeV.

We adopt Rein-Sehgal's method [77] to simulate this interaction. To evaluate the cross section, this model, calculates the amplitude ($|T|$) of producing 18 resonance states shown in Table 6.1. In the next step, it multiplies the respective amplitude by the branching ratio χ_E that the excited baryon decays into one pion and a nucleon. At this time, it considers interference among the resonances. The differential cross section is:

$$\frac{d^2\sigma}{dq^2 d\nu} = \frac{1}{32\pi M E^2} \cdot \frac{1}{2} \cdot \sum_{spins} |T(\nu N \to l N^*)|^2 \cdot \chi_E \cdot \left(\frac{1}{2\pi} \cdot \frac{\Gamma^2}{(W-M)^2 + \Gamma^2/4} \right) \tag{6.6}$$

Figure 6.3 shows the cross section for single pion production channels compared with the experimental data [72, 78].

In the case that the target is a nucleon in Oxygen, we consider that 20% of Δ decays without pion [79].

6.2.3 Coherent pion production

The interaction of neutrinos with nuclei, via charged our neutral currents, can lead to the coherent production of pions which carry the same charge as the incoming current. The

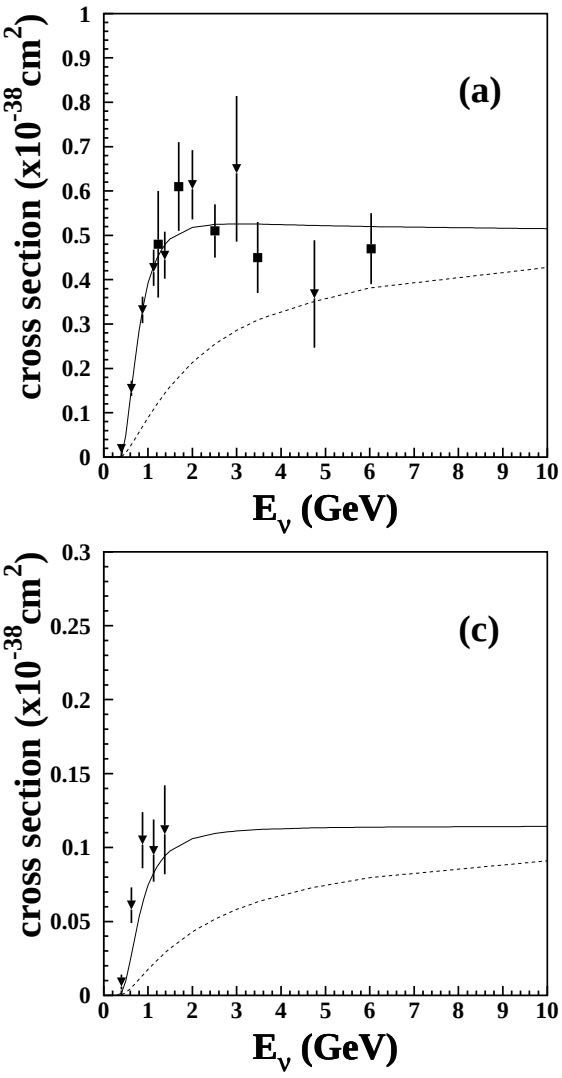

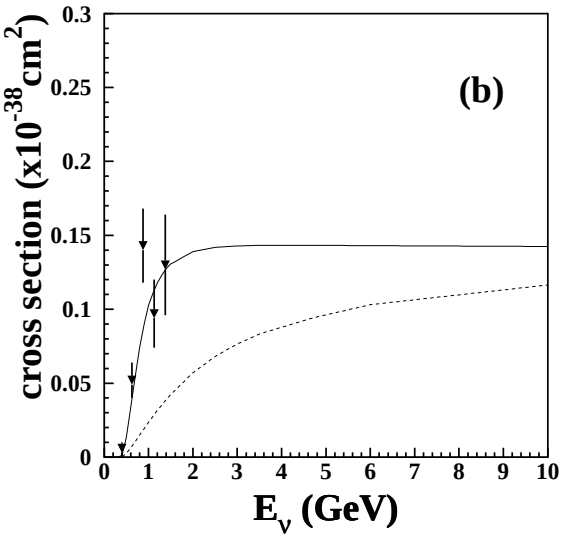

Figure 6.3: The calculated cross section of the single pion production compared with the experimental data. In (a), solid (broken) line shows $\nu P \rightarrow l^- P \pi^+$ ($\bar{\nu} N \rightarrow l^+ N \pi^-$). In (b), solid (broken) line shows $\nu N \rightarrow l^- P \pi^\circ$ ($\bar{\nu} N \rightarrow l^+ N \pi^\circ$). In (c), solid (broken) line shows $\nu N \rightarrow l^- N \pi^+$ ($\bar{\nu} P \rightarrow l^+ N \pi^-$). Triangles (squares) show the data from [78]([72]). In these figures, we restricted that W should be less than 1.4 GeV/c^2.

R.S.	$M\ [MeV/c^2]$	$\Gamma\ [MeV]$	χ_E
P_{33}	1232	115	1.00
P_{11}	1440	200	0.60
D_{13}	1520	125	0.55
S_{11}	1535	150	0.43
S_{31}	1620	140	0.30
S_{11}	1650	150	0.60
P_{33}	1600	370	0.10
D_{13}	1700	100	0.10
D_{15}	1675	155	0.35
F_{15}	1680	125	0.60
P_{11}	1710	110	0.15
D_{33}	1700	250	0.15
P_{13}	1720	200	0.15
P_{31}	1910	220	0.22
P_{35}	1905	300	0.12
P_{37}	1950	240	0.40
P_{33}	1920	250	0.17
F_{17}	1990	325	0.01

Table 6.1: Table of resonances used in this simulation. R.S. is Resonance States, M is the invariant Mass, Γ is the total width, and χ_E is the elasticity (πN branching ratio).

differential cross section of coherent pion production can be calculate based on Alder's PCAC formula [80, 81], and be expressed as follows [82, 83]:

$$\frac{d^3\sigma}{dQ^2dydt} = \beta \times \frac{G^2M}{2\pi^2} f_\pi^2 A^2 E_\nu (1-y) \frac{1}{16\pi} \left[\sigma_{tot}^{\pi^\circ N}(E_\nu y)\right]^2 \left(1 + \left(\frac{\mathrm{Re}(f_{\pi N}(0))}{\mathrm{Im}(f_{\pi N}(0))}\right)^2\right) \times \left(\frac{M_A^2}{M_A^2+Q^2}\right)^2 \exp\left(-\frac{1}{3}R^{2/3}|t|\right) F_{abs} \quad (6.7)$$

where q^2 is the square of the 4-momentum transfer of lepton, t is the square of the momentum transferred to the nucleus, M_A is the axial-vector mass ($1.01 GeV/c^2$), $f_\pi = 0.93 m_\pi$, $f_{\pi N}$ is the πN scattering amplitude, G is the weak coupling constant, M is the mass of nucleon, E_ν and E_l are the energy of neutrino and outgoing lepton, respectively and $y = (E_\nu - E_l)/E_\nu$, A is the atomic number of oxygen ($= 16$), and R is the nuclear radius. β is the axial vector coupling constant. Because β is recalling that the axial parts of the neutral and charged currents form a triplet in isospace, it takes 2(1) for the charged(neutral) current interaction. $\sigma_{tot}^{\pi^\circ N}$ is the average pion-nucleon cross section, which is approximately expressed as:

$$\sigma_{tot}^{\pi^\circ N} = \frac{1}{4}\left[\sigma_{tot}^{\pi^+ D} + \sigma_{tot}^{\pi^- D}\right] \quad (6.8)$$

where $\sigma_{tot}^{\pi^\pm D}$ is the $\pi^\pm D$ total cross section [84]. F_{abs} is t-independent attenuation factor representing the effect of pion absorption in the nucleus, and is expressed as:

$$F_{abs} = \exp\left(-\frac{9A^{1/3}\sigma_{inel}}{16\pi R_0^2}\right) \quad (6.9)$$

where $R_0 = 1.0 fm$, σ_{inel} is the inelastic πN Cross section which is taken from the data Table [84]. The cross section of coherent pion production is shown in Fig. 6.4.

6.2.4 Multi pion production

The total cross section of charged current multi pion production is calculated by integrating the following equation:

$$\begin{aligned} \frac{d^2\sigma}{dxdy} &= \frac{G_F^2 M_N E_\nu}{\pi}\left(\left(1 - y + \frac{y^2}{2} + C_1\right) F_2(x,q^2) \pm y\left(1 - \frac{y}{2} + C_2\right)\left(xF_3(x,q^2)\right)\right), \\ C_1 &= \frac{yM_l^2}{4M_N E_\nu x} - \frac{xyM_N}{2E_\nu} - \frac{M_l^2}{4E_\nu^2} - \frac{M_l^2}{2M_N E_\nu x}, \\ C_2 &= -\frac{M_l^2}{4M_N E_\nu x} \end{aligned} \quad (6.10)$$

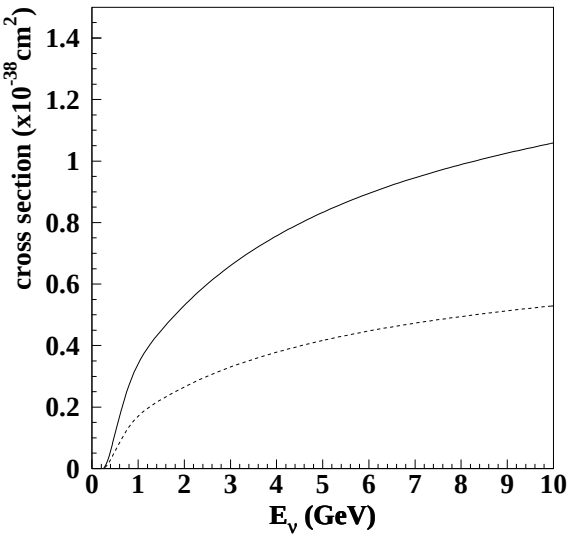

Figure 6.4: The cross section of the coherent pion production. Solid (broken) line shows the cross section for $\nu + {}^{16}O \rightarrow l + \pi^{\pm} + {}^{16}O(\nu + {}^{16}O \rightarrow \nu + \pi^{\circ} + {}^{16}O)$. For the interaction via the neutral current, the calculated cross section is exactly half of the CC cross section.

where M_N is the mass of nucleon, M_l is the mass of lepton, $x = -q^2/\{2M(E_\nu - E_l)\}$, $y = (E_\nu - E_l)/E_\nu$, E_ν and E_l are the energy of incoming neutrino and outgoing lepton in the laboratory frame, respectively. In the case of ν, $\pm$ takes plus, otherwise it is minus. The nucleon structure function F_2 and xF_3 are taken from Ref. [85].

In our simulation, the cross sections via neutral current are expressed by the following relations:

$$\frac{\sigma(\nu N \rightarrow \nu X)}{\sigma(\nu N \rightarrow \mu^- X)} = \begin{cases} 0.26 & (E_\nu \leq 3GeV) \\ 0.26 + 0.04 \times \frac{E_\nu - 3}{3} & (3 < E_\nu < 6GeV) \\ 0.30 & (E_\nu \geq 6GeV) \end{cases}$$

$$\frac{\sigma(\bar{\nu} N \rightarrow \bar{\nu} X)}{\sigma(\bar{\nu} N \rightarrow \mu^+ X)} = \begin{cases} 0.39 & (E_\nu \leq 3GeV) \\ 0.39 - 0.02 \times \frac{E_\nu - 3}{3} & (3 < E_\nu < 6GeV) \\ 0.37 & (E_\nu \geq 6GeV) \end{cases} \tag{6.11}$$

These relations are estimated from the experimental results [86, 87].

Figure 6.5 shows the calculated cross section for multi pion production based on Eq. 6.10.

The kinematics of out-going mesons is calculated by two method. At the invariant mass range less than 2.0 GeV, we use our original code. From the result of Fermi-lab 7-foot hydrogen bubble chamber experiment, the mean multiplicity of charged pions $\langle n_{\pi^\pm} \rangle$is

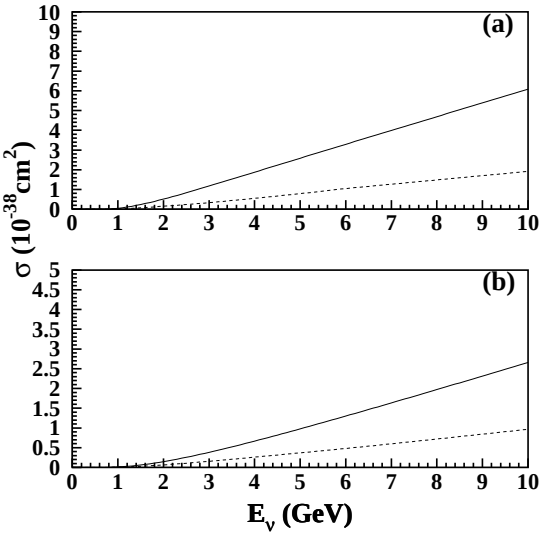

Figure 6.5: The calculated cross section for multi pion production as a function of E_ν. (a) for CC, (b) for NC. Solid (broken) lines show the cross section for $\nu_\mu + n \to \mu^- + p + n\pi (\bar{\nu_\mu} + p \to \mu^+ + n + n\pi)$.

estimated as:

$$\langle n_{\pi^\pm} \rangle = (0.06 \pm 0.06) + (1.22 \pm 0.03) \ln(W^2) \tag{6.12}$$

Assuming $\langle n_{\pi^+} \rangle = \langle n_{\pi^-} \rangle = \langle n_{\pi^\circ} \rangle$, the mean multiplicity of pion $\langle n_\pi \rangle$ is:

$$\langle n_\pi \rangle = 0.09 + 1.83 \ln(W^2) \tag{6.13}$$

The number of pion for each events is determined based on the KNO scaling [88]. Since the range of W overlaps with that of the single pion production, we require $n_\pi \geq 2$ in this W range of multi-pion production. The forward-backward asymmetry of pion multiplicity (n_π^F / n_π^B) in the center of the mass system of the hadrons is obtained from the BEBC experiment [89], and included as follows:

$$\frac{n_\pi^F}{n_\pi^B} = \frac{0.35 + 0.41 \ln(W^2)}{0.5 + 0.09 \ln(W^2)} \tag{6.14}$$

In the case of $W > 2.0$ GeV, we use the Jetset [90], which is frequently used for event generation in high-energy physics.

Finally the total cross section is calculated by adding all the channels and is shown in Fig. 6.6.

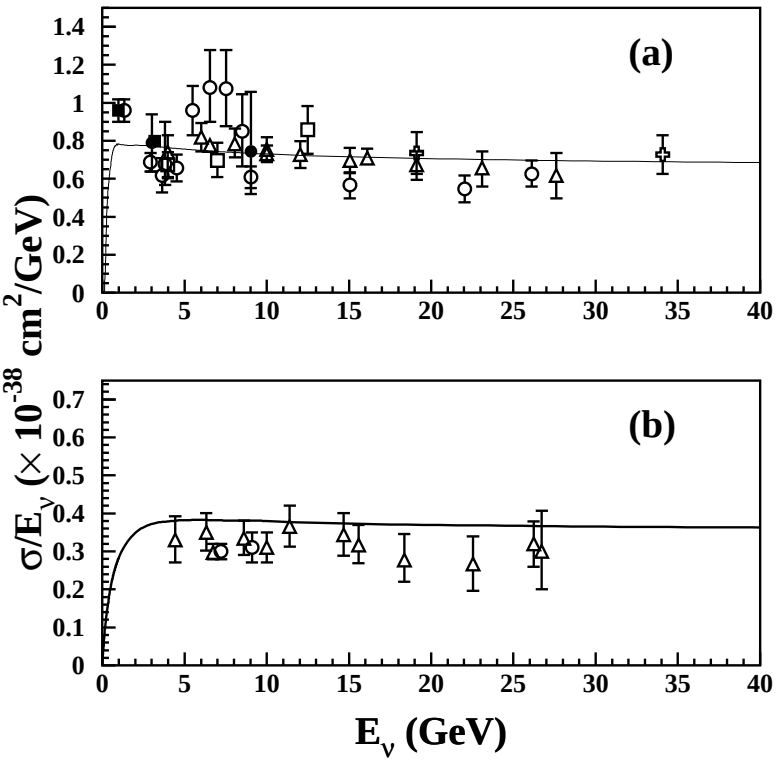

Figure 6.6: The charged current total calculated cross section derived by E_ν used in our Monte Carlo simulation. (a) for $\nu_\mu n \to \mu^- p$, (b) for $\bar{\nu_\mu} p \to \mu^+ n$ White circle [91, 92, 93], white square [94], cross [95], triangle [96, 97], and circle [74]

6.3 Meson nuclear effect

The mesons produced in a ^{16}O nucleus often make secondary interactions before leaving the nucleus. Thus, the meson interactions with nucleon have a significant effect in estimating the detection efficiency of π°, or in the selection of single-ring events.

The interaction position ($\vec{r}$) of a neutrino, and the production position of a pion in the oxygen nucleus is set according to the Woods-Saxon type nucleon the density distribution $\rho(\vec{r})$:

$$\rho(\vec{r}) = \frac{1}{2}\bar{\rho}\left\{1 + \exp\left(\frac{|\vec{r}| - c}{a}\right)\right\}^{-1} \tag{6.15}$$

where $\bar{\rho}(= 0.48 m_{\pi}^{3})$ is the average density of nucleus, a$(= 0.41 fm)$ and c$(= 2.69 fm)$ are density parameters of nucleus. In our Monte Carlo simulation program, the pion interaction in ^{16}O includes:

- inelastic scattering
- charge exchange
- absorption

Each cross section is calculated based on the Oset model [98]. In selecting interaction modes, Fermi motion of nucleus and Pauli blocking effect are considered. If inelastic interaction or charge exchange is selected, the momentum of the recoil nucleon is requested to exceed the Fermi surface momentum $p_F(r)$, which is a function of the density of nucleon at the interaction position $\vec{r}$:

$$p_F(r) = \left[\frac{3}{2}\pi^2 \rho(\vec{r})\right]^{-1/3} \tag{6.16}$$

The direction and momentum of the pion is estimated from the result of a phase shift analysis obtained from the π-N scattering experiment [99].

We tested this pion interaction model using the following three interaction data:

- $\pi^{12}C$ scattering [100] (see Fig. 6.7)
- $\pi^{16}O$ scattering [101] (see Fig. 6.8)

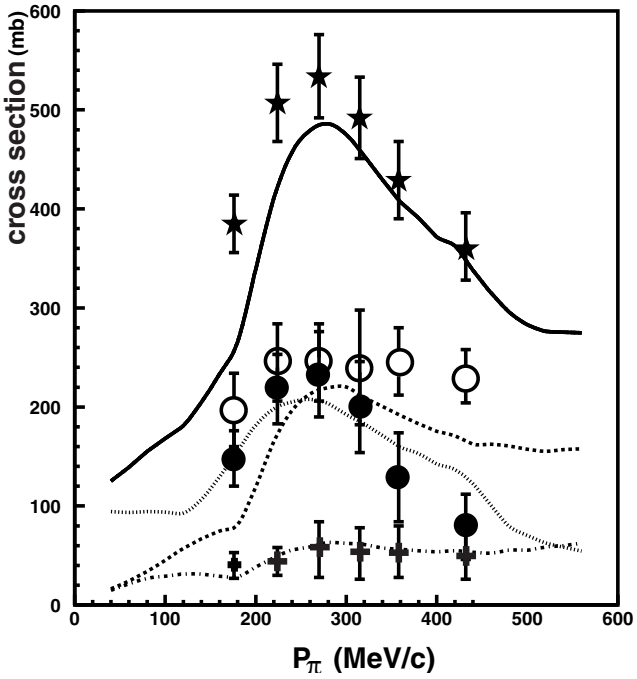

Figure 6.7: The calculated cross sections of the pion with a ^{12}C nucleus compared with the experimental data [100]. The stars (Solid line) for the total cross section, the white circles (broken line) for the inelastic scattering, the black circles (dashed line) for absorption, the crosses (dashed dotted line) for the charge exchange.

- photo-production of pions ($\gamma^{12}C \to \pi^- X$) [102, 103] (we used the cross section of primary interaction ($\gamma n \to \pi^- p$) from the experimental result [104]) (see Fig. 6.9)

6.4 Detector simulation

The GEANT package [105], which is used generally among high-energy experiment, is used for detector simulation in Super-Kamiokande. For the hadronic interaction in water, we used CALOR package based on the nuclear cascade model [106], because this package reproduces the pion interaction well above 0.5 GeV/c. But the reproducibility for the low energy pion with momentum less than 0.5 GeV/c is not enough for our experiment, and there is no package better than CALOR in simulating low energy pions. Thus we made our own code based on the result of πH_2O scattering experiment [107, 108, 109].

Cherenkov photon radiation is also treated in the GEANT package. But the tracking part of Cherenkov photons was developed by us for this experiment. For the short wave length, Rayleigh scattering is dominant because the mean scattering length is proportional to $1/\lambda^4$. Thus we take into account this scattering. For the longer wavelength, measured wavelength dependence of the light scattering and absorption is used. The attenuation

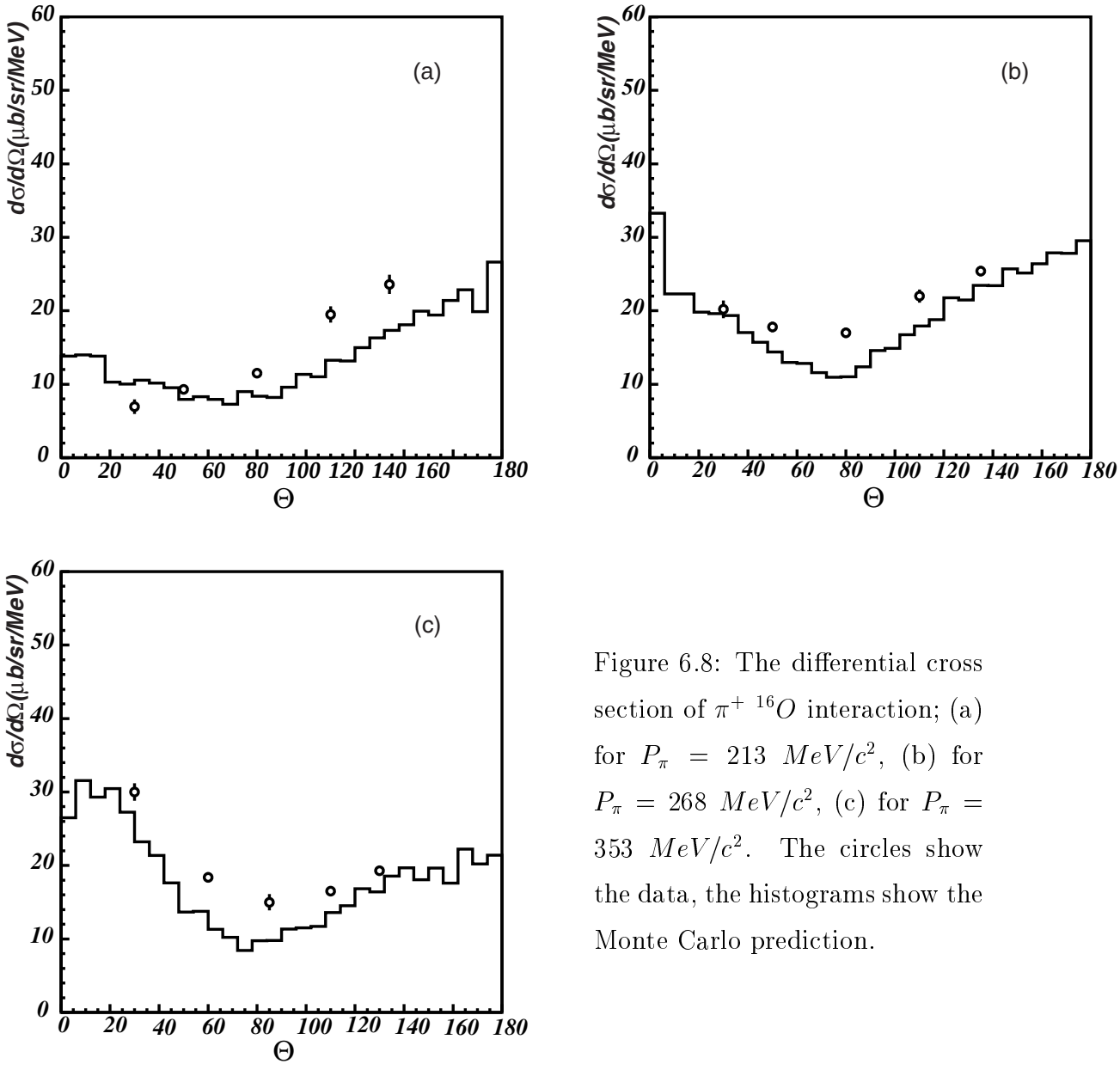

Figure 6.8: The differential cross section of $\pi^+ \, ^{16}O$ interaction; (a) for $P_\pi = 213 \; MeV/c^2$, (b) for $P_\pi = 268 \; MeV/c^2$, (c) for $P_\pi = 353 \; MeV/c^2$. The circles show the data, the histograms show the Monte Carlo prediction.

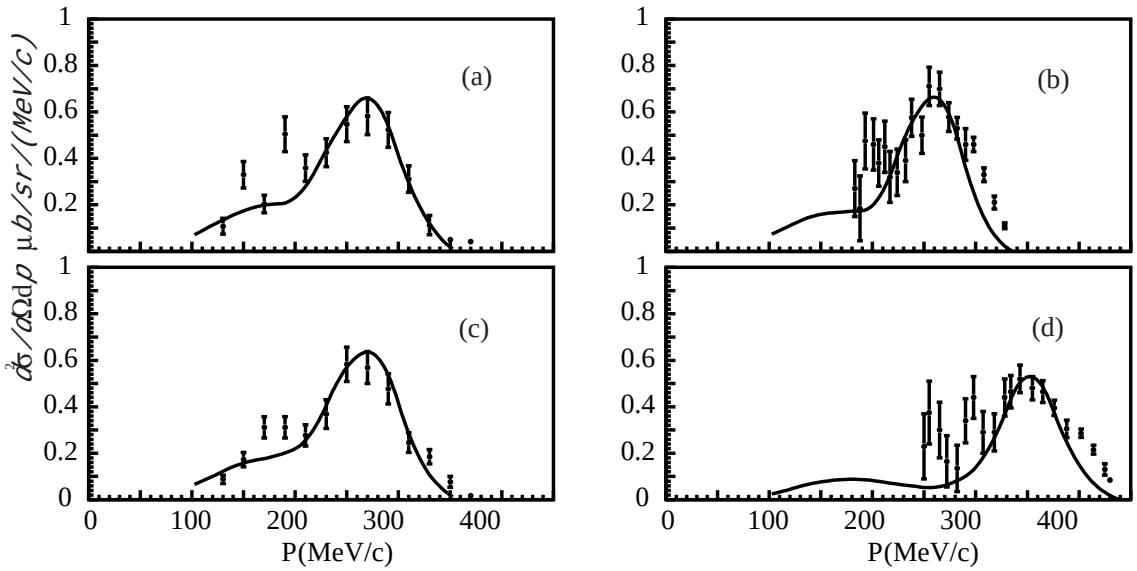

Figure 6.9: The differential cross section for the pion photo-production;(a) for $^{12}C\gamma \rightarrow \pi^- X(E_\gamma = 391\ MeV)$ [102],(b) for $^{12}\gamma \rightarrow \pi^- X(E_\gamma = 368\ MeV)$ [103], (c) for $^{12}C\gamma \rightarrow \pi^+ X(E_\gamma = 391\ MeV)$ [103], (d) for $^{12}C\gamma \rightarrow \pi^+ X(E_\gamma = 468 MeV)$ [102].

length, shown in Fig. 3.10, is used in our simulation program. Also shown are the results of direct measurement of water transparency.

The quantum efficiency of PMTs has been measured as shown in Fig. 2.5. Also, the collection efficiency of photo-electrons at the dynode was measured to be 70 %. Based on these results, Cherenkov photon detection part of the simulation was developed.

Chapter 7

Data summary

We observed 6982 (470) events for the fully contained (partially contained) sample with an exposure of 52 kton year. Also, we made 40 years (900 kton year equivalent) of Monte Carlo events and analyzed them in the same way as we did for the real data.

In this chapter, we summarize the final data sample for the real data and the Monte Carlo. Then the important information in this analysis; the number of ring, vertex position, momentum, and PID likelihood distribution are presented.

7.1 Data summary

Final event samples were made by the following criteria:

For fully contained events,

1. $E_{vis} > 30 MeV$
2. $D_{wall} > 2$ meters
3. Number of OD-clusters hits ≤ 9
4. $P_e > 100 MeV/c$ for e-like single-ring events, $P_\mu > 200 MeV/c$ for μ-like single-ring events

For partially contained events,

1. $D_{wall} > 2$ meters

		DATA	MC(Honda)	MC(Bartol)
sub-GeV	1R	3678	4371.6	4268.1
	e-like	1826	1754.0	1729.5
	μ-like	1852	2617.6	2538.6
	2R	1156	1389.1	1369.0
	$\geq$3R	300	481.7	480.8
multi-GeV	1R	790	901.3	917.6
	e-like	439	414.3	430.8
	μ-like	351	487.0	486.8
	2R	451	575.7	592.7
	$\geq$3R	416	503.8	525.8
PC		470	656.4	696.7

Table 7.1: Event summary. Sub-GeV(multi-GeV) indicates the event sample with $E_{vis} <$ $(>)1.33GeV$.

where D_{wall} is the distance between the event vertex and the nearest inner detector wall.

Table 7.1 summarizes the observed events and Monte Carlo predictions based on Honda and Bartol fluxes [13, 14]. Here we classify the events with $E_{vis} < (>)1.33GeV$ as the sub-GeV (multi-GeV) sample. E_{vis} is the energy of an electron that would produce the observed amount of Cherenkov light. $E_{vis} = 1.33GeV$ for muon events corresponds to $p_\mu \sim 1.4GeV/c$. The numbers of the Monte Carlo events were normalized to the detector exposure for comparison. The fraction of each interaction mode is summarized in Table 7.2.

7.2 Vertex position distribution

The vertex position distributions of neutrino events are expected to be uniform in the detector. Figure 7.1 and 7.2 show the vertex position distributions projected to the Z and the $R^2 = (X^2 + Y^2)$ directions with the Monte Carlo prediction. For the multi-GeV μ-like events of both data and Monte Carlo, the number of events with their vertex positions

			CC ν_e		CC ν_μ		NC	Total
			q.e. %	non-q.e. %	q.e. %	non-q.e. %	%	%
1R	sub-GeV	e-like	66.68	20.16	0.77	2.23	10.17	100
		μ-like	0.22	0.12	73.33	21.99	4.33	100
	multi-GeV	e-like	34.81	45.65	0.78	8.26	10.50	100
		μ-like	0.06	0.27	50.51	48.86	0.30	100
$\geq$ 2 R	sub-GeV		4.22	18.22	5.75	37.60	34.20	100
	multi-GeV		2.07	29.04	2.05	52.73	14.11	100
PC			0.27	1.66	14.95	82.26	0.87	100

Table 7.2: The fraction of each interaction mode for various types of events. These numbers are obtained based on Honda-flux without neutrino oscillation. q.e. indicates quasi-elastic interaction.

near the wall were small compared to the ones around the center. On the other hand, for the PC event sample, the event rate near the wall was higher than that around the center. This is because a fraction of muons near the wall can reach the anti-counter, and were identified as PC events.

We compared the shape of the distribution of the real data with these of the Monte Carlo prediction by using a χ^2 test. The results are summarized in Table 7.3. This table shows that all the distributions of the data were consistent with the corresponding distribution of the Monte Carlo.

7.3 Number of rings and PID distribution

The number of rings and PID play important role in this analysis. Therefore we need to confirm the reproducibility of our Monte Carlo. Figure 7.3 shows the number of rings for the data and Monte Carlo without neutrino oscillations. From this figure, it turned out that the Monte Carlo reproduced the shape of the number of rings distribution of the real data well. Figure 7.4 shows the PID likelihood distribution $L \equiv= \sqrt{P_{PID}(\mu)} - \sqrt{P_{PID}(e)}$ for single-ring events, where P_{PID} is defined in Eq. 5.23. Again, our Monte

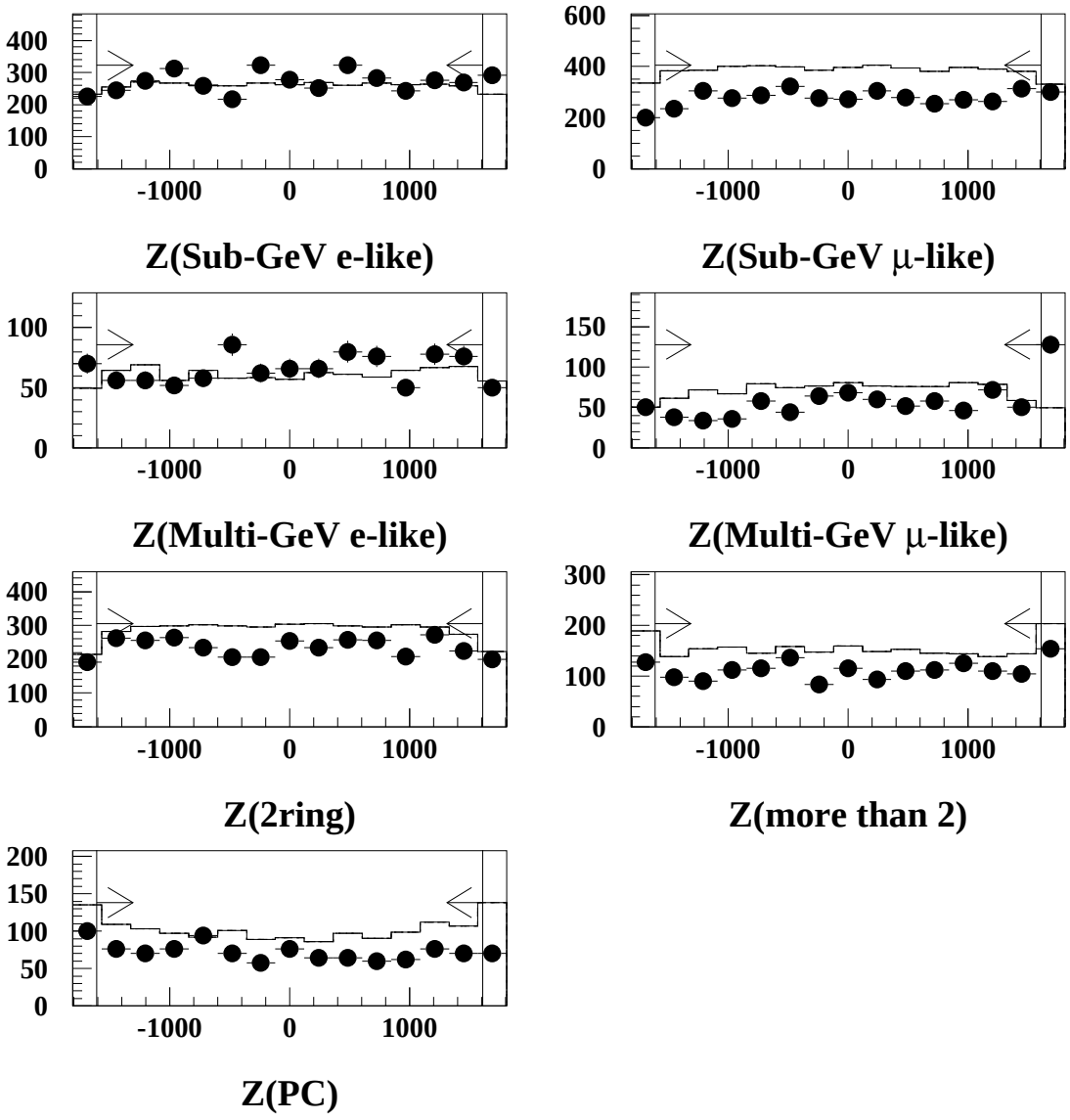

Figure 7.1: The vertex distribution projected to the Z direction. Only events with $R < 14.9m$ are plotted. The arrows indicates the fiducial volume.

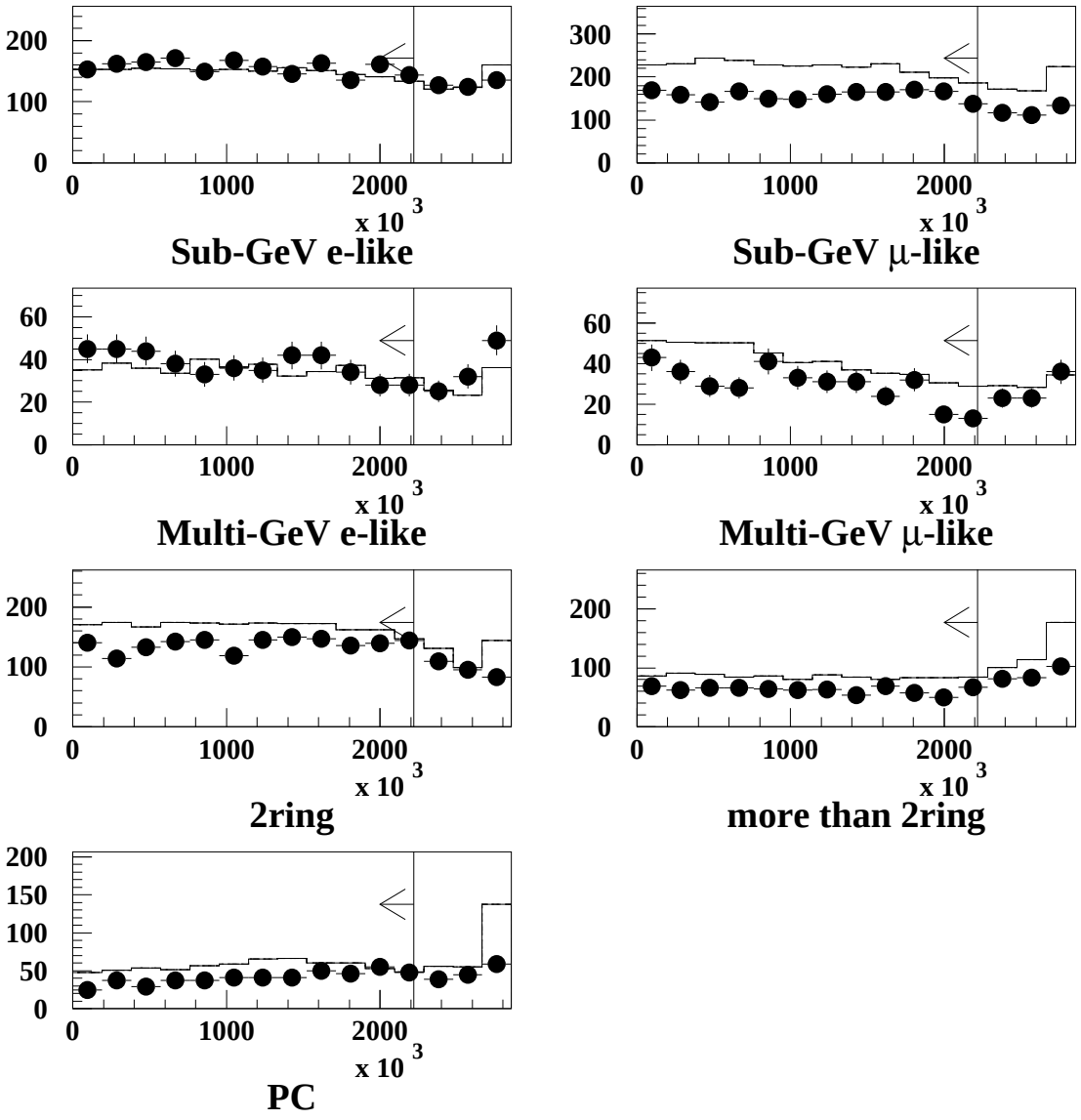

Figure 7.2: The vertex distribution projected to the R^2 direction. Only events with $|z| < 16.1m$ are plotted. The arrows indicates the fiducial volume.

			$\chi^2/d.o.f(\%)$	
			Z	R^2
1R	sub-GeV	e-like	23.8/14 (4.8)	9.6/14 (79.0)
		μ-like	17.7/14 (22.1)	11.8/14 (62.2)
	multi-GeV	e-like	18.8/14 (17.3)	22.2/14 (7.5)
		μ-like	17.2/14 (24.6)	22.0/14 (7.9)
2R			13.4/14 (49.5)	12.4/14 (57.4)
$\geq$3R			21.7/14 (8.5)	6.3/14 (95.8)
PC			13.7 /14 (44.2)	23.4/14 (5.4)

Table 7.3: χ^2 analysis of the vertex position distribution for events in the fiducial volume. Only the shape of the distributions is compared between the data and the Monte Carlo. The numbers in the parentheses shows the probability.

Carlo reproduced the shape of the distribution for e-like and μ-like events separately. We note that the relative height of the e-like and μ-like histograms is different between the data and the Monte Carlo, most probably due to neutrino oscillations.

7.4 Summary

We found that the vertex position distributions of the events inside the fiducial volume were consistent with the expectation from the atmospheric neutrino interaction.

We also found that various distributions such as numbers of rings are consistent with the atmospheric neutrino Monte Carlo. These distributions are almost independent of neutrino oscillations and confirm the data quality and the reproducibility of the Monte Carlo.

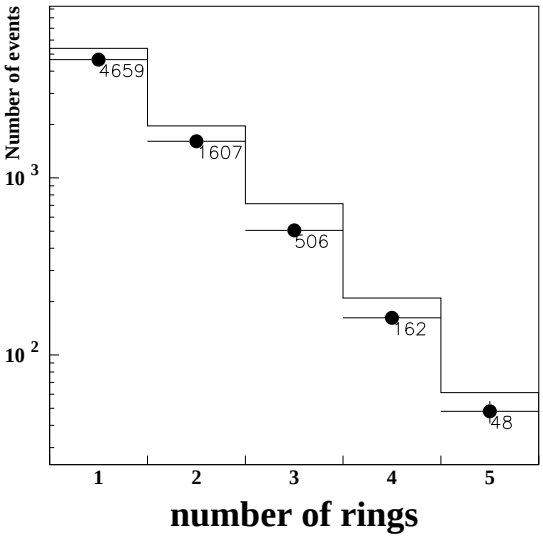

Figure 7.3: Number of ring distributions for FC events. The black circles show the distribution for the real data; the histogram for the Monte Carlo prediction without neutrino oscillation. The prediction was calculated based on the Honda flux [13].

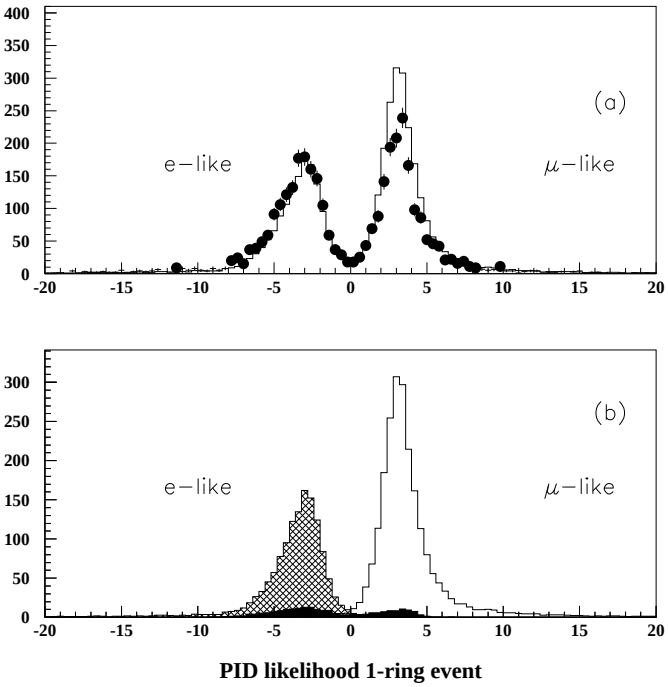

Figure 7.4: PID likelihood parameter ($L \equiv \sqrt{P_{PID}(\mu)} - \sqrt{P_{PID}(e)}$) distributions for FC single-ring events. In (a), the black circles show the real data, the histogram show the MC. In (b), the white histogram shows the L for $CC\nu_\mu$, the hatched one for $CC\nu_e$, black one for NC.

Chapter 8

Neutrino oscillation analysis using FC single-ring events

In this chapter, the results of $(e/\mu)_{data}/(e/\mu)_{MC}$ ratio and the zenith angle distribution studies are presented. Then a neutrino oscillation analysis using FC single-ring events is carried out. Both $\nu_\mu \to \nu_\tau$ and $\nu_\mu \to \nu_s$ oscillation hypotheses are tested. The allowed regions of neutrino oscillation parameters from this analysis are also shown.

8.1 μ/e ratio

If neutrinos oscillate, the observed atmospheric ν_μ/ν_e flux ratio should be different from that of the theoretical calculation. Although the uncertainty in the absolute flux of the atmospheric neutrino was estimated to be $\sim 30\%$ as mentioned in Chapter 1, the ratio $(\nu_\mu + \bar{\nu_\mu})/(\nu_e + \bar{\nu_e})$ was calculated within 5% uncertainty. This is because most neutrino is produced by the decay chain of $\pi^\pm \to \mu^\pm \overset{(-)}{\nu}_\mu$, $\mu^\pm \to e^\pm \overset{(-)}{\nu}_\mu \overset{(-)}{\nu}_e$. To study the ν_μ/ν_e flux ratio, we observed the μ/e ratio of the data and compared with the theoretical prediction. As seen from Table 7.2, the μ/e ratio approximates the ν_μ/ν_e ratio. The results were as follows: We used FC single-ring events with $E_{vis} < 1.33 (E_{vis} > 1.33) GeV$

for $R \equiv (\mu/e)_{data}/(\mu/e)_{MC}$ in the sub-GeV (multi-GeV) region.

$$R = \begin{cases} 0.680 \ ^{+\ 0.023}_{-\ 0.022} \ (stat.) \pm 0.05_{(sys.)} & E_{vis} < 1.33GeV \\ 0.680 \ ^{+\ 0.050}_{-\ 0.047} \ (stat.) \pm 0.09_{(sys.)} & E_{vis} > 1.33GeV \end{cases} \tag{8.1}$$

In both cases, R were significantly smaller than unity. R should be consistent with unity, if neutrinos do not oscillate. Therefore, these results confirmed the atmospheric neutrino anomaly. The systematic error in R is discussed in the next section.

8.2 Systematic error in R

In this section, we discuss the systematic errors in R. The sources of the systematic errors in R were separated into three parts: the uncertainties in the atmospheric neutrino flux; ones in the cross section of neutrinos off nucleus; ones related to reconstruction methods.

8.2.1 Systematic error in the atmospheric neutrino flux

The dominant source of the systematic errors related to the atmospheric neutrino flux is the uncertainty in the flux ratio of the atmospheric neutrino flavor, especially the $(\nu_\mu + \bar{\nu_\mu})/(\nu_e + \bar{\nu_e})$ ratio. Although the uncertainty in the absolute flux of the atmospheric neutrino was estimated to be 30%, the ratio $(\nu_\mu + \bar{\nu_\mu})/(\nu_e + \bar{\nu_e})$ was calculated within 5% uncertainty. This uncertainty changes R by $\delta R = 4.6\%$ (4.1 %) in the sub-GeV (multi-GeV) energy region.

In addition, we need to consider the uncertainties in $\nu_\mu/\bar{\nu_\mu}$ and $\nu_e/\bar{\nu_e}$ ratios, because the cross section for $\nu_{\mu,e}N$ interaction is roughly a factor of 2 larger than that of $\bar{\nu}_{\mu,e}N$. The uncertainty of $\nu_\mu/\bar{\nu_\mu}(\nu_e/\bar{\nu_e})$ ratio with neutrino energy $< 30GeV$ was estimated to be 5 (10) % in Ref.[13]. We found that sub-GeV (multi-GeV) R changes by 1.0 and 2.4 % (0.3 and 1.1 %) if we change the $\nu_\nu/\bar{\nu_\mu}$ and $\nu_e/\bar{\nu_e}$ ratios by 5 and 10 %, respectively.

Another source related to the atmospheric neutrino flux is the uncertainty of the energy spectrum of the primary cosmic-ray protons. The energy spectrum of the primary cosmic-ray protons is approximately proportional to $E^{-\gamma}$, where the power index, γ, is 2.71 ± 0.05 in the energy range around $10 \sim 10^6 GeV$ [13]. Thus the energy spectrum of the

atmospheric neutrinos is proportional to $E^{-\gamma}f(E)$, where $f(E)$ is a yield function which takes account of the energy dependence of decay probabilities and meson production cross sections. Therefore the uncertainty in the power index of the primary cosmic-ray flux is reflected in the neutrino energy spectrum. In order to estimate the systematic error, the spectrum has been changed by a factor of $E_\nu^{\pm 0.05}$. As a result, error in R, δR, for sub-GeV (multi-GeV) was evaluated to be 0.6 (1.6) %. Table 8.1 summarizes δR as we change the neutrino ratios and the spectra index within the uncertainty.

	uncertainty	Systematic error in R	
		sub-GeV	multi-GeV
$(\nu_\mu + \bar{\nu_\mu})/(\nu_e + \bar{\nu_e})$	5.0%	4.6%	4.1%
$\nu_\mu/\bar{\nu_\mu}$	5.0%	1.0%	0.3 %
$\nu_e/\bar{\nu_e}$	10.0%	2.4%	1.1%
$E^{-\gamma}$	± 0.05	0.6 %	1.6 %
total		5.3 %	4.5 %

Table 8.1: The systematic error in R related to the atmospheric neutrino flux.

8.2.2 Systematic error from the neutrino interaction cross sections

First, we discuss the uncertainty of the quasi-elastic interaction. In the case of a free proton target, the dominant uncertainty in this interaction mode is the value of the axial vector mass, M_A. We estimated this systematic error in R to be 0.9%(1.0%) in the sub-GeV(multi-GeV) energy range by comparing R with $M_A = 1.01GeV$ to R with $M_A = 1.01 \pm 0.1GeV$.

In the case of an Oxygen target, in addition to the uncertainty of M_A, we have to consider some uncertainties related to the nuclear model. Our neutrino interaction simulation considers the Pauli blocking by requiring that the momentum of a recoil nucleon must exceed the Fermi surface momentum, P_F, which is a function of the momentum of in-coming neutrino. We checked the parameter dependence of R by comparing R with

the one based on a different nuclear model whose P_F is constant($P_F = 250MeV$) and no nuclear potential. The difference of the two Rs was small. Moreover we checked the parameter dependence by changing P_F to 180 MeV. As the result, δRs were 3.3% and 0.9% for sub-GeV and multi-GeV, respectively. Table 8.2 summarizes δR as we change M_A and P_F. We estimated the systematic error originating from the uncertainty of M_A and nuclear effects to be 3.5(1.5) % in the sub-GeV(multi-GeV) energy region.

		Systematic error in R	
		sub-GeV	multi-GeV
M_A	$1.01 \pm 0.1GeV$	0.9 %	1.0 %
nuclear potential off	(P_F is $250MeV$)	0.5 %	0.1%
P_F	$250 \rightarrow 180MeV$	-3.3 %	-0.9 %
total		3.5 %	1.5%

Table 8.2: δR as simulation parameters in quasi-elastic interaction are changed. P_F is the Fermi momentum and M_A is the axial vector mass.

The relative contribution of each interaction mode in the μ-like sample is different from that of the e-like one as shown in Table 7.2. This difference makes R change with the change of the absolute value of each cross section. For example, we estimated the uncertainty in the absolute cross section of the single pion production was 30%. When the absolute cross section of the single-pion production in both samples increased by 30 %, the $(\mu/e)_{MC}$ in the multi-GeV region changed by 1.2%. Accordingly the systematic error coming from this uncertainty was estimated to be 1.2%. We estimated the systematic errors arising from the uncertainties of each neutrino cross section in the same way. Additionally, we considered the uncertainties in the NC/CC cross section ratio. These uncertainties of NC/CC ratio for all the cross section channel were estimated to be 20 %. These results are summarized in Table 8.3

Another source of the systematic error in R is the uncertainty of the simulation of the hadron interaction in water. We adapted CALOR as the hadron simulator to generate the Monte Carlo events. To estimate the uncertainty of the hadron simulation, we compared the result of another hadron simulator, FLUKA, with that of CALOR. The differences

mode		uncertainty	systematic error in R	
			sub-GeV	multi-GeV
q.e.	$CC + NC$	(*)	3.5%	1.5 %
	NC/CC	20%	$< 0.1\%$	$< 0.1\%$
1 pi	$CC + NC$	30%	$< 0.1\%$	1.4 %
	NC/CC	20%	0.6 %	0.2 %
c pi	$CC + NC$	30%	0.5 %	0.4 %
	NC/CC	20%	0.4 %	0.2 %
m pi	$CC + NC$	40%(**)	0.8 %	0.2 %
	NC/CC	20%	0.2 %	0.2 %
total			3.7 %	2.1%

Table 8.3: Systematic error in R coming from the cross section. q.e. : quasi-elastic interaction; 1 pi: single pion interaction; c pi: coherent pion interaction; m pi: multi pion interaction. (*) The uncertainties coming from q.e. are estimated in Table 8.2. (**) The uncertainty of multi-pion production is conservatively taken to be 40 % near the threshold energy region ($\sim GeV$).

in R between FLUKA and CALOR were 0.5 % and 1.0 % for sub-GeV and multi-GeV, respectively.

8.2.3 Systematic error related to the event reconstruction

The systematic errors in R related to the event reconstruction are caused by the uncertainties of the several parameters used in our Monte Carlo simulation. For example, one of the parameters is the timing resolution of each PMT. The vertex resolution obtained by TDCfit, which calculates the vertex position using the timing information, is strongly dependent on the timing resolution of each PMT. If our estimation of the timing resolution was not very accurate, then our Monte Carlo cannot reproduce the vertex resolution of the real data. To estimate these systematic errors, we used several reconstruction tools, and compared the obtained R. In the case of vertex position resolution, we used MSfit,

which obtains the vertex position using the Cherenkov charge pattern and is almost independent of the timing information. Comparing the result of the TDCfit and MSfit, we estimated the systematic errors related to the vertex reconstruction were 0.6% and 2.4% in the sub-GeV and multi-GeV energy region, respectively.

Next, we estimated the systematic error related to the ring counting based on the comparison to the results from two different versions of ring counting program and from the manual scanning. The differences in R between manual scanning and our ring counting program were estimated to be 3% and 10%, for sub-GeV and multi-GeV, respectively. The systematic error related to the ring counting was the largest in all the errors related to the event reconstruction.

According to the Monte Carlo study, the misidentification probability of particle identification for single-ring events was estimated to be 0.6% (1.2%) for sub-GeV (multi-GeV). The systematic error in R coming from this misidentification was estimated to be 1.2%(2.4%) for sub-GeV(multi-GeV) by simply doubling the misidentification probability.

The uncertainty of the energy scale causes the systematic error in R of 1.0% in sub-GeV region. However in multi-GeV region, the error was estimated to be 5.5%. These numbers were obtained by changing the p.e. numbers by $\pm 2.5\%$ for Monte Carlo events, where $\pm 2.5\%$ is the estimated uncertainty of the absolute energy scale of the detector.

The uncertainty of the reduction efficiency for FC events was negligible according to the Monte Carlo study.

The background contamination such as the flashing PMT events were considered as a source of the systematic error. The charge pattern made by the remaining flashing PMT events is diffuse like single-ring e-like events. And the cosmic μ induced neutrons coming from the surrounding rock collide with water and sometimes make π°s. Some of them with relatively high momentum are identified as single-ring e-like events, because their opening angle between two γs from π° decay is narrow and they tend to be identified as single-ring e-like events. Therefore these events were thought to be the candidate of e-like background events. The cosmic μs, whose vertex position was reconstructed inside the fiducial volume by misfit, were identified as single-ring μ, and the dominant background of μ-like events. The effects of these background are summarized in Table 8.4.

Finally, the systematic error due to the statistics of the Monte Carlo events was 0.8%

	Systematic error in R	
	sub-GeV	multi-GeV
flashing PMT events	0.5 %	0.3 %
cosmic-ray μ	0.1 %	0.1 %
cosmic-ray μ induced neutron	$< 0.1\%$	0.1 %
total	0.5 %	0.3 %

Table 8.4: Systematic error in R coming from the background contamination.

(1.5%) for sub-GeV (multi-GeV). The total systematic error in R was estimated to be 7.4% (13.0%) in the sub-GeV(multi-GeV) region. Table 8.5 summarizes the systematic error in R.

		sub-GeV (%)	multi-GeV (%)
atmospheric	neutrino ratio	5.3	4.2
neutrino flux	$E^{-\gamma}$	0.6	1.6
simulation	neutrino interaction	3.7	2.1
	hadron simulator	0.5	1.0
reconstruction	reduction	$\ll 1$	$\ll 1$
and	vertex position	0.6	2.4
data analysis	1ring/multi-ring separation	3	10
	μ/e separation	1.2	2.4
	energy calibration	1	5.5
	background contamination	0.5	0.3
M.C. statistics		0.8	1.5
total systematic error		7.4	13.0

Table 8.5: Summary of the systematic error in R

8.3 The $Up/Down$ ratio

Next, we discuss the $Up/Down$ ratio of FC single-ring sample. There is a large difference in the path-length between upward-going ($\sim$ 10,000 km) and downward-going neutrinos ($\sim$ 20 km). If the solution of the atmospheric neutrino anomaly is the neutrino oscillation, the evidence can be found in the zenith angle distribution. Figure 8.1 shows the $\cos\Theta$ distributions for e-like events and μ-like events, where Θ is the zenith angle of the particle direction, and $\cos\Theta = -1(1)$ corresponds to upward-going (downward-going). The angular correlation between the neutrino direction and the produced charged lepton direction for sub-GeV (multi-GeV) neutrinos is calculated to be $\sim 60^\circ$ ($\sim 20^\circ$) (RMS) as shown in Fig. 8.2. Therefore, the observed zenith-angle distributions correspond to the neutrino zenith angle distribution at high energy region. Figure 8.1 proves that the observed $\cos\Theta$ distributions for e-like events were in good agreement with the expected ones. For multi-GeV μ-like events, the observed number of upward-going events had obvious deficit compared with the Monte Carlo prediction, although the number of observed downward-going events was consistent with the predicted one.

For quantitative evaluation of a deficit of up-going μ-like events, we defined the $Up/Down$ ratio, where Up (Down) was the number of up-going (down-going) events with $-1 < \cos\Theta < -0.2$ ($0.2 < \cos\Theta < 1$). Horizontal-going events ($-0.2 < \cos\Theta < 0.2$) were excluded. Table 8.6 summarizes the $Up/Down$ ratio in sub-GeV and multi-GeV regions. The $Up/Down$ ratios for μ-like events in both sub-GeV and multi-GeV were significantly smaller than unity. Especially, the $Up/Down$ ratio of the multi-GeV μ like events deviated from unity by more than $5\,\sigma$. On the other hand, the observed $Up/Down$ ratios for e-like events were consistent with the expected ones within uncertainties. The systematic error in the $Up/Down$ ratio is discussed in the next section.

8.4 Systematic error in the $Up/Down$ ratio

Several sources of the systematic error in the $Up/Down$ ratio were considered. First, the systematic error in the $Up/Down$ ratio related to the calculation of the atmospheric neutrino flux was estimated.

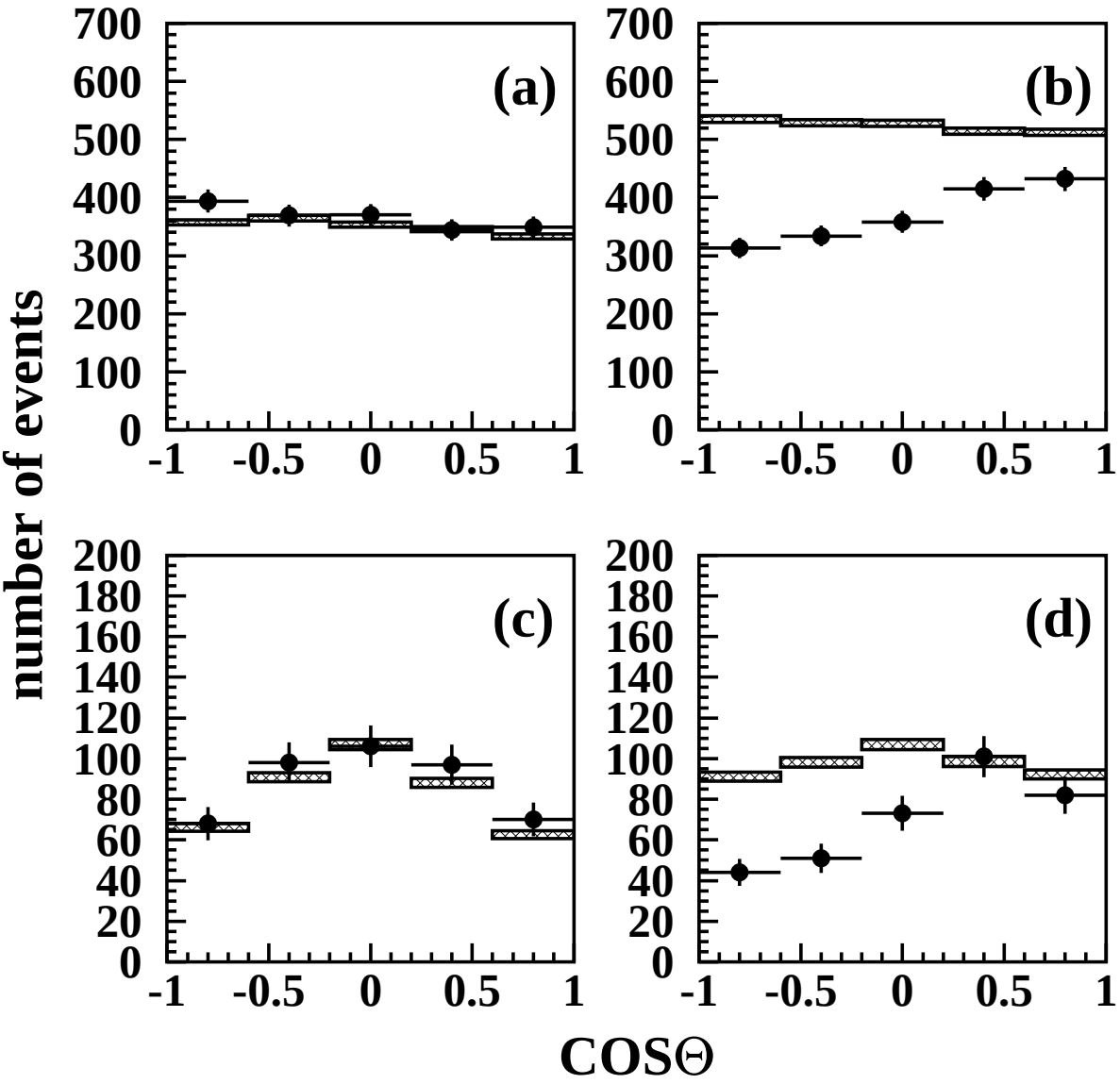

Figure 8.1: The zenith angle distributions; (a) for the sub-GeV e-like events, (b) for the sub-GeV μ-like events, (c) for the multi-GeV e-like events, and (d) for the multi-GeV μ-like events. $\cos\Theta$=1 means down-going. The histograms with the shaded error bars show the Monte Carlo predictions with their statistical error.

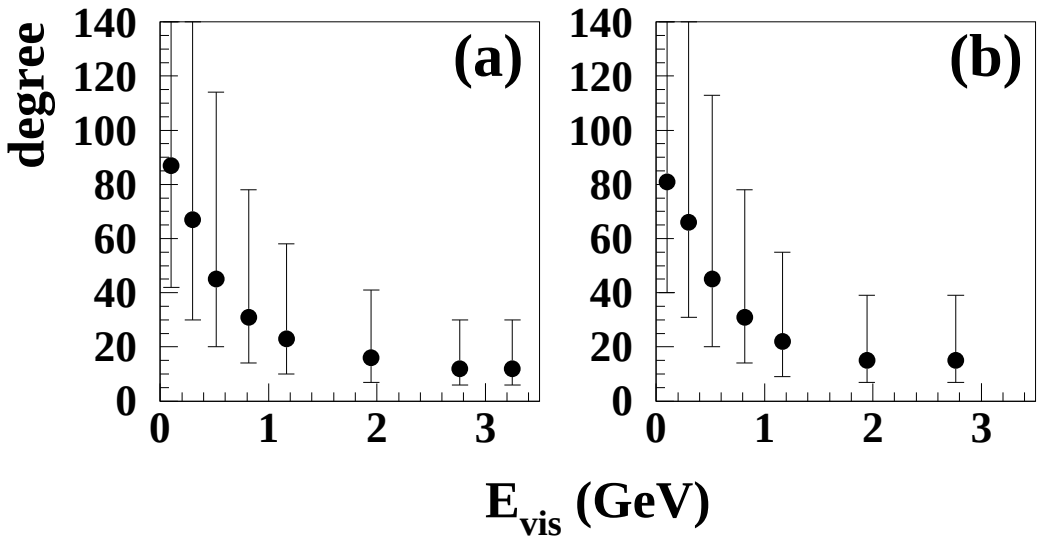

Figure 8.2: Angular correlation between the direction of the primary neutrinos and the reconstructed direction of the leptons as a function of the reconstructed momentum of leptons. The events are the FC single-ring events. The binning in this figure is the same as the one we use for an oscillation analysis shown in this section. (a) is for the e-like sample and (b) for the μ-like sample.

		DATA	M.C.
sub-GeV	e-like	$1.101\ ^{+0.059}_{-0.056}\ (stat.) \pm 0.01_{(sys.)}$	$1.065 \pm 0.014_{(stat.)} \pm 0.03_{(sys.)}$
	μ-like	$0.764\ ^{+0.041}_{-0.039}\ (stat.) \pm 0.003_{(sys.)}$	$1.037 \pm 0.011_{(stat.)} \pm 0.03_{(sys.)}$
multi-GeV	e-like	$0.994\ ^{+0.116}_{-0.103}\ (stat.) \pm 0.01_{(sys.)}$	$1.043 \pm 0.029_{(stat.)} \pm 0.03_{(sys.)}$
	μ-like	$0.519\ ^{+0.070}_{-0.062}\ (stat.) \pm 0.007_{(sys.)}$	$0.992 \pm 0.025_{(stat.)} \pm 0.015_{(sys.)}$

Table 8.6: The $Up/Down$ ratio of the FC single-ring sample. The slopes of Monte Carlo in sub-GeV region are due to the geo-magnetic field effects. The cut off rigidity at Super Kamiokande site is higher than the average. The event rate of the downward-gong events in sub-GeV region is, therefore, lower than that of upward-going events at the sub-GeV region.

As shown in Table 8.6, the expected $Up/Down$ ratios are close to unity. The up-down asymmetry of these ratios are due to the geo-magnetic field effect. The cut off rigidity at the Super Kamiokande site is higher than the average. Therefore the low-energy downward-going neutrino fluxes are lower than the upward-going ones. We compared two independent calculated fluxes [13, 14] for e-like and μ-like events to estimate the uncertainty from the flux calculation (which depends on the assumption of the cut off rigidity). The differences of the expected $Up/Down$ ratios between these calculations for sub-GeV e-like, sub-GeV μ-like, multi-GeV e-like, and multi-GeV μ-like events were 2.8 %, 3.2%, 1.6%, and 1.2%, respectively.

The second source of the systematic error is the "Mt. Ikenoyama effect". Neither calculation takes into account the existence of Mt. Ikenoyama over the Super Kamiokande detector. This effect is negligible at low energies. At high energies, however, a fraction of cosmic muons reach the ground before it decays, therefore we must consider the height of Mt. Ikenoyama: ~ 1 kilometer. The effect of Mt. Ikenoyama on the $Up/Down$ ratio was estimated to be 2.0(0.9) % for e-like (μ-like) events in the multi-GeV region. Here we note that this effect cannot explain upward-going neutrino deficit, because this effect reduces downward-going events, and makes the $Up/Down$ ratio larger.

Next, the systematic error related to the detector is discussed. The background contamination can cause the up-down asymmetry. We must consider the possible contamination by cosmic-ray muons. These events could be background to down-going μ-like events. In addition, the flasher events could be the background to e-like events. The systematic error in the $Up/Down$ ratio from these background contamination sources were estimated to be $< 1.0\%$, $< 0.2\%$, $< 0.5\%$, and $< 0.2\%$ for sub-GeV e-like, sub-GeV μ-like, multi-GeV e-like, and multi-GeV μ-like events, respectively. These numbers were obtained by assuming that the background contamination discussed in Sec. 8.2.3 may direct only to the upward-going or downward-going direction.

We estimated that the detector PMT gain could be different by 1.2% $\pm$0.6% between down-going particles and up-going particles by studying decay electrons from stopping cosmic ray muons. Figure 8.3 shows the zenith angle distribution of the mean reconstructed energy of the decay electrons. This gain difference caused $< \pm 0.1\%$, $\pm 0.2\%$, $\pm 0.9\%$, and $\pm 1.4\%$ $Up/Down$ systematic error for sub-GeV e-like events, sub-GeV μ-

like events, multi-GeV e-like events, and multi-GeV μ-like events, respectively. Table 8.7 summarizes the uncertainties in the $Up/Down$ ratio.

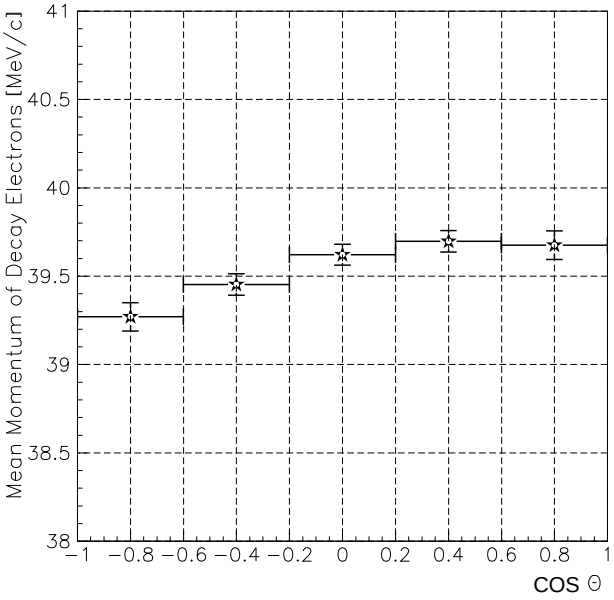

Figure 8.3: Mean reconstructed energy of the electrons from the decay of stopping cosmic ray muons as a function of $\cos\Theta$, where Θ is the zenith angle of the decay electron. The up-down difference of the detector gain is estimated to be ± 0.6 %.

8.5 Neutrino oscillation analysis

We examined the hypotheses of two-flavor $\nu_\mu \to \nu_\tau$ and $\nu_\mu \to \mu_s$ oscillation modes using a χ^2 comparison of data and Monte Carlo, allowing all important Monte Carlo parameters to vary weight by their expected uncertainties. For this analysis, we used fully contained single-ring events only. The matter effect [36, 37, 38, 59, 60, 61] is taken into account in the $\nu_\mu \to \nu_s$ analysis. This effect for $\nu_\mu \to \nu_s$ is different from the one for $\bar{\nu_\mu} \to \bar{\nu_s}$, and the interaction cross section and kinematics are different between ν_μ and $\bar{\nu_\mu}$. Therefore, for $\nu_\mu \to \nu_s$ oscillations, we calculated χ^2 on both assumptions of $\Delta m^2 > 0$ and $\Delta m^2 < 0$.

The data were binned by particle type, momentum, and $\cos\Theta$. A χ^2_{FC} is defined as:

$$\chi^2_{FC} = \sum_{\cos\Theta,p}^{65} \left(\frac{N_{data} - N_{MC}(\sin^2 2\theta, \Delta m^2, \epsilon_j)}{\sigma} \right)^2 + \sum_j \left(\frac{\epsilon_j}{\sigma_j} \right)^2 \qquad (8.2)$$

where the sum is over five bins equally spaced in $\cos\Theta$ and seven (six) momentum bins for e-like (μ-like) events. The statistical error, σ, accounts for both data statistics and the Monte Carlo statistics. N_{data} is the measured number of events in each bin. N_{MC} is

		sub-GeV		multi-GeV	
		e-like (%)	μ-like (%)	e-like (%)	μ-like (%)
for data	energy scale $\pm 0.6\%$	$< \pm 0.1$	± 0.2	± 0.9	± 1.4
	background contamination	$< \pm 1.0$	$< \pm 0.2$	± 0.5	$\pm < 0.2$
for MC	flux (Honda $\rightarrow$ Bartol)	± 2.8	± 3.2	± 1.6	± 1.2
	Mt. Ikenoyama effect	$\ll 1$	$\ll 1$	± 2.0	± 0.9

Table 8.7: Systematic errors in the *Up/Down* ratio. The systematic error from the energy scale is due to the up-down difference of the PMT gain by $\pm 0.6\%$. The cosmic ray muon and the flasher PMTs are considered as the source of the background. The systematic error related to the expected neutrino flux is obtained by the comparison of the independent calculations. 'Mt. Ikenoyama effect' means the deficit of the downward-going neutrino, which is caused by the fact that a fraction of downward-going muon reach Mt. Ikenoyama before it decays.

the weighed sum of Monte Carlo events:

$$N_{MC} = \frac{L_{data}}{L_{MC}} \times \sum_{MC events} w \tag{8.3}$$

L_{data} and L_{MC} are the data and Monte Carlo livetimes. For each Monte Carlo events, the weight, w, is given by:

$$w = (1+\alpha)(E_\nu^i/E_0)^\delta (1+\eta_{s,m}\cos\Theta) f_{e,\mu}(\sin^2 2\theta, \Delta m^2) \begin{cases} (1-\beta_s/2) & \text{sub-GeV } e\text{-like} \\ (1+\beta_s/2) & \text{sub-GeV } \mu\text{-like} \\ (1-\beta_m/2) & \text{mulit-GeV } e\text{-like} \\ (1+\beta_m/2) & \text{multi-GeV } \mu\text{-like} \end{cases} \tag{8.4}$$

where E_ν^i is the average neutrino energy in the i-th momentum bin; E_0 is an arbitrary reference energy (taken to be 2 GeV); η_s (η_m) is the up-down uncertainty of the event rate in the sub-GeV (multi-GeV) energy range. The factor $f_{e,\mu}$ weights events accounting for oscillation parameters, L/E_ν, and the matter effect. The parameter α is the overall normalization factor; $\beta_{s(m)}$ is related to the systematic error in the μ/e ratio in

sub-GeV(multi-GeV) energy region; δ is an ambiguity of the index of neutrino energy spectrum. The calculation of the neutrino production height is taken from [14], which accounts for the competing factors of production, propagation, and decay of muons and mesons through the atmosphere. The assigned uncertainties of these parameters, σ_j, and fitted values, are summarized in Table 8.8. A global scan was made on a $(\sin^2 2\theta, \log \Delta m^2)$ grid minimizing χ^2 with respect to α, β_s, β_m, δ, η_s, and η_m at each point. Figure 8.4 shows the allowed parameter regions. The uncertainty of L/E_ν, which was estimated to be $\pm 15\%$, was taken into account by expanding the allowed region in Δm^2 by $\pm 15\%$. This uncertainty mainly comes from the ambiguity of the production height of neutrinos in the atmosphere. The confidence levels were defined to be $\chi^2 = \chi^2_{min} + \Delta\chi^2$, where $\Delta\chi^2$ = 4.6 and 9.2 for the 90%C.L., and 99%C.L. allowed regions, respectively.

The best fit neutrino oscillation parameters to the three oscillation hypotheses were identical;$(\sin^2 2\theta, \Delta m^2) = (1.0, 3.0 \times 10^{-3} eV^2)$. The $\chi^2_{FC}/d.o.f$ at the best fit position of $\nu_\mu \to \nu_\tau$ oscillation was 48.9/62, and χ^2_{FC} for $\nu_\mu \to \nu_s$ oscillation was 47.8/62.[1]

The best fit values of the Monte Carlo parameters were all within their expected errors, see Table 8.8. These results mean that these hypotheses are all in good agreement with our data. The 90 % C.L. allowed parameter regions are summarized in Table 8.9 for the three oscillation assumptions.

8.6 Summary of the single-ring analysis

We confirmed the atmospheric neutrino oscillation by using $R \equiv (\mu/e)_{data}/(\mu/e)_{MC}$, and the $Up/Down$ ratio. Especially, the $Up/Down$ ratio of μ-like events cannot be explained by the uncertainties in the atmospheric neutrino flux and the event reconstruction.

The $\nu_\mu \to \nu_x (x = \tau, s)$ neutrino oscillation hypotheses were in good agreements with the data. Finally, in Fig. 8.5, we show the zenith angle distributions of the data tougher

[1]For the $\nu_\mu \to \nu_s$ oscillation analysis, the best fit positions and the χ^2 values parameters for both $(\Delta m^2 > 0)$ and $(\Delta m^2 < 0)$ were identical. The difference in the oscillation between the two cases is due to the difference in the sign of the potential of the matter effect (see Eq. 1.11). However, this difference disappears at $\sin^2 2\theta = 1$. According to Eq. 1.10, the effective mixing angle at $\sin^2 2\theta = 1$ is written as: $\sin^2 2\theta_m = \sin^2 2\theta/(\zeta^2 + 1)$. Therefore the behaviors of both oscillations are identical at $\sin^2 2\theta = 1$.

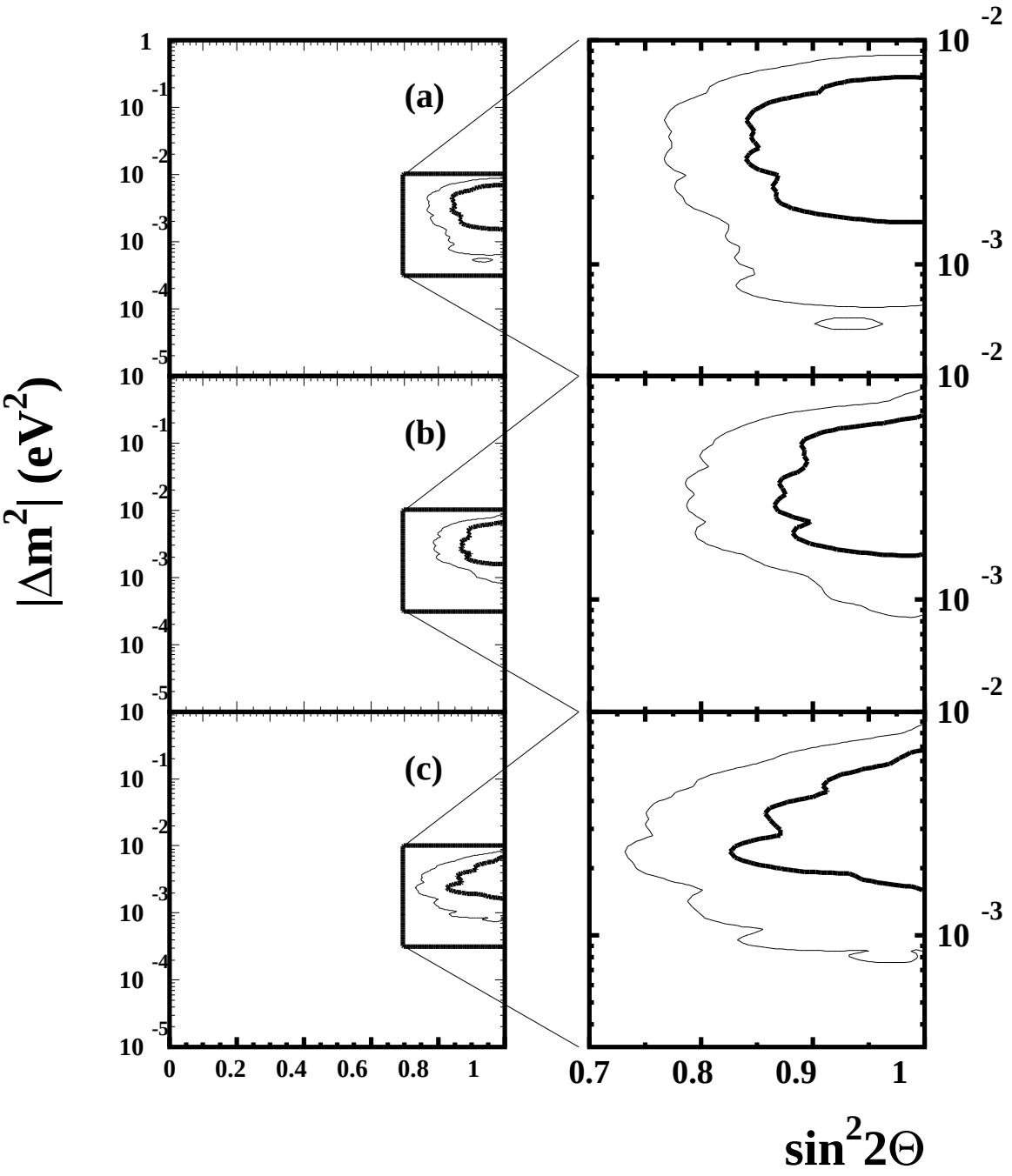

Figure 8.4: The allowed regions for each hypothesis from the FC single-ring events; (a) for $\nu_\mu \to \nu_\tau$ oscillation, (b) for $\nu_\mu \to \nu_s(\Delta m^2 > 0)$, and (c) for $\nu_\mu \to \nu_s(\Delta m^2 < 0)$. Thick (Thin) line shows 90%(99%) C.L.. The figures on the right show the magnified region ($0.7 < \sin^2 2\theta < 1, 10^{-3.5} < \Delta m^2 < 10^{-2}$) of the figures on the left. The behaviors of $\nu_\mu \to \nu_s$ vary according to the sign of Δm^2, as we had noted. However, in this analysis, the best fit positions for all cases are at $\sin^2 2\theta = 1$. Therefore the behavior of the $\nu_\mu \to \nu_s$ oscillation with $\Delta m^2 > 0$ is identical with $\Delta m^2 < 0$ at $\sin^2 2\theta = 1$.

Monte Carlo Fit Parameters		Best fit		uncertainty
		$\nu_\mu \to \nu_\tau$	$\nu_\mu \to \nu_s$	
α	overall normalization	4.7 %	5.7 %	(*)
β_s	sub-GeV μ/e ratio	0.6 %	1.2 %	7.4 %
β_m	multi-GeV μ/e ratio	5.0 %	6.6 %	13.0%
δ	E_μ spectral index	-0.013	-0.009	0.05
η_s	sub-GeV up-down	1.0 %	1.0 %	3.1 %
η_m	multi-GeV up-down	-0.4 %	-0.5 %	3.0 %

Table 8.8: Summary of Monte Carlo fit parameters for $\nu_\mu \to \nu_\tau$ and $\nu_\mu \to \nu_s$ oscillations. We calculated the χ^2 and fit parameters for both sign of Δm^2 for $\nu_\mu \to \nu_s$ oscillations. However, the best fit positions of $\nu_\mu \to \nu_s$ oscillation were both at $\sin^2 2\theta = 1$, so that χ^2 and fitting parameters for both cases were identical. (*) α was estimated to have 30 % uncertainty but was fitted as a free parameter.

	Δm^2 $(10^{-3} eV^2)$	$\sin^2 2\theta$
$\nu_\mu \to \nu_\tau$	$1.5 \sim 7$	$0.85 \sim 1$
$\nu_\mu \to \nu_s (\Delta m^2 > 0)$	$1.5 \sim 7$	$0.87 \sim 1$
$\nu_\mu \to \nu_s (\Delta m^2 < 0)$	$1.5 \sim 7$	$0.83 \sim 1$

Table 8.9: The 90 % allowed parameter regions for three oscillation hypotheses.

with the predictions of the two oscillation hypotheses for the best-fit parameters. As shown in this figure, both oscillation hypotheses were very similar, and reproduced the observed zenith angle distributions well. As a result, it is difficult to discriminate $\nu_\mu \to \nu_\tau$ and $\nu_\mu \to \nu_s$ oscillation hypotheses by using the FC single-ring events.

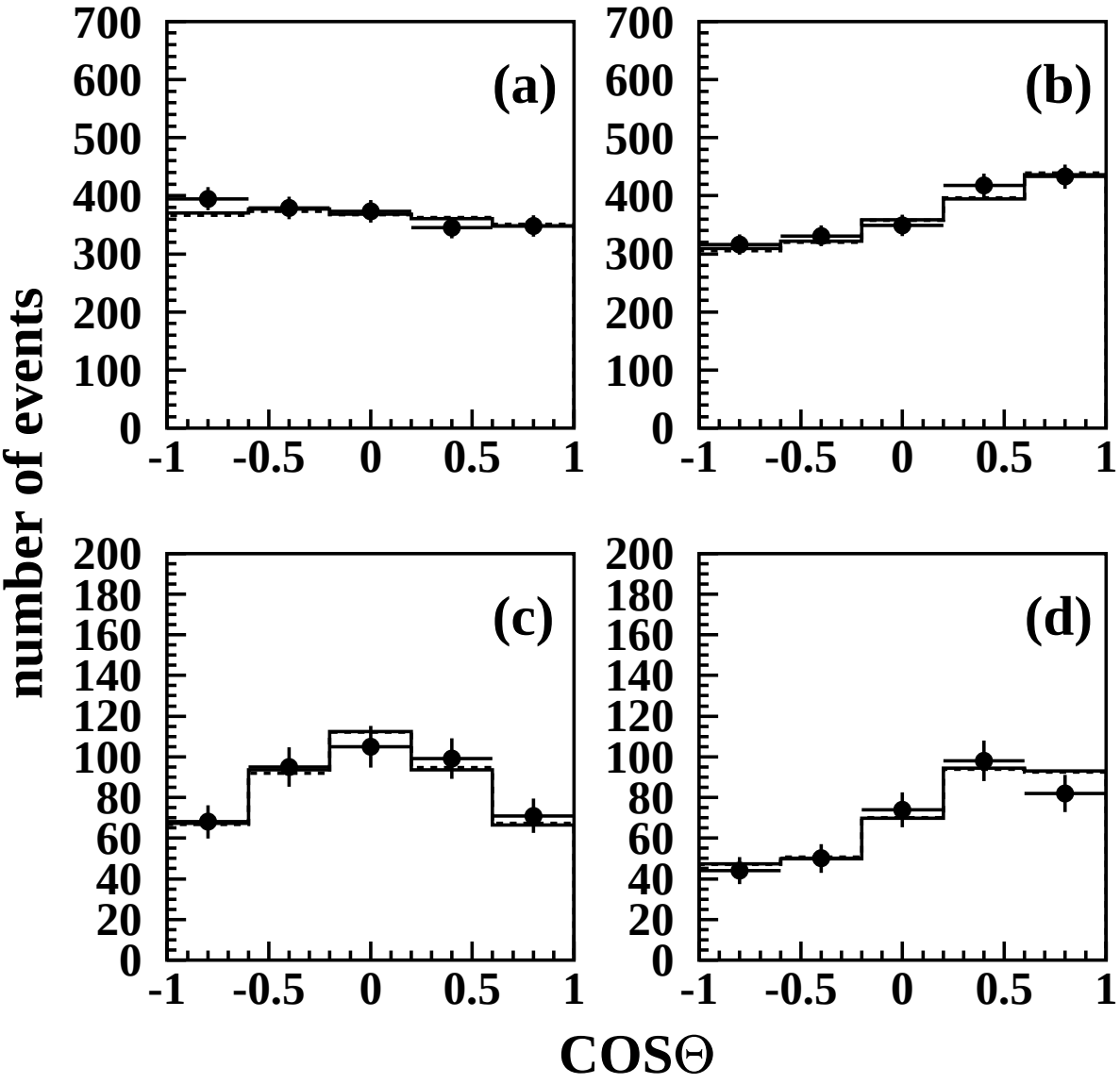

Figure 8.5: The zenith angle distributions with the Monte Carlo prediction for the two oscillations. The circles show the observed data, the solid line shows the distribution for $\nu_\mu \to \nu_\tau$, and the dashed line for $\nu_\mu \to \nu_s$ oscillations. For both oscillation hypotheses, $\Delta m^2 = 3.0 \times 10^{-3} eV^2$ and $\sin^2 2\theta = 1.0$ are assumed. The two expected distributions are so similar that the two histograms are not discriminated.

Chapter 9

Tests of $\nu_\mu \to \nu_\tau$ and $\nu_\mu \to \nu_s$ oscillations

The analysis of the FC single-ring events demonstrates that the $\nu_\mu \to \nu_x (x = \tau, s)$ oscillations can explain the atmospheric neutrino data, as described in the previous chapter. It also indicates that the difference in the expected signal among these hypotheses is too small in the FC single-ring sample to discriminate them. The motivation of this thesis is to distinguish the $\nu_\mu \to \nu_\tau$ and the $\nu_\mu \to \nu_s$ solutions of the atmospheric neutrino oscillation. We checked the consistency of the $\nu_\mu \to \nu_\tau$ and $\nu_\mu \to \nu_s$ oscillation hypotheses with two samples; the PC events, and the FC multi-ring ones.

9.1 Partially contained events

The $\nu_\mu \to \nu_\tau$ and $\nu_\mu \to \nu_s$ oscillation hypotheses at $\sin^2 2\theta = 1$ and $\Delta m^2 = 3 \times 10^{-3} eV^2$ are both in a good agreement with the data for FC single-ring events. However, $\nu_\mu \to \nu_s$ oscillation is suppressed by the matter effect at the high energy region [59, 60, 61], as described in Chapter 1. The mean neutrino energy of the multi GeV μ-like sample is $\sim 3GeV$ which is not so high that the difference of the two oscillation hypotheses due to the matter effect is small at $\Delta m^2 = 3 \times 10^{-3} eV^2$. On the other hand, the mean energy of the PC event sample is $\sim 10GeV$, therefore a significant matter effect is expected in the case of $\nu_\mu \to \nu_s$ and the study of the PC events may distinguish the two solutions.

Figure 9.1 shows the expected zenith angle distribution for PC events for both hypotheses with $\Delta m^2 = 1.5 \times 10^{-3}$ and $6.5 \times 10^{-3} eV^2$ at $\sin^2 2\theta = 1$. The differences in the upward-going events are due to the matter effect. In this section, we try to distinguish the two oscillation hypotheses by the *Up/Down* ratio of PC sample.

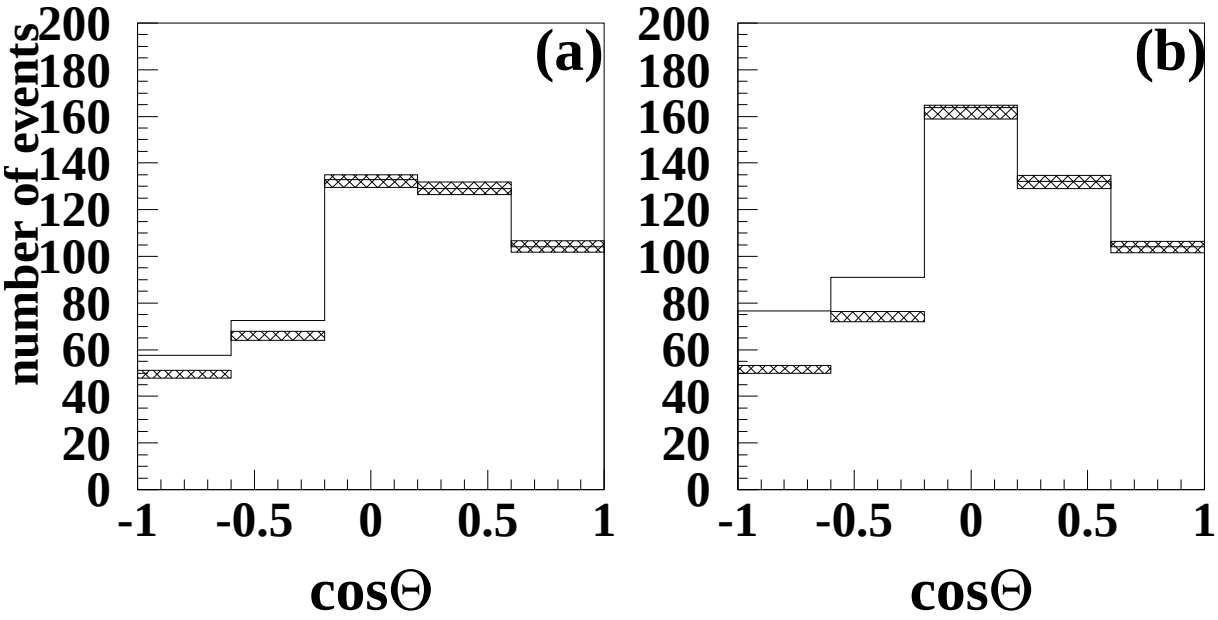

Figure 9.1: Expected zenith angle distribution for the PC events with neutrino oscillations at $\sin^2 2\theta = 1$. The event number is normalized by the livetime of the PC sample (52 kt·yr). The hatched histogram shows the expected distribution for $\nu_\mu \to \nu_\tau$ oscillation with its statistical error. The solid line is for $\nu_\mu \to \nu_s$ oscillation. (a) for $\Delta m^2 = 6.5 \times 10^{-3} eV^2$, (b) for $\Delta m^2 = 1.5 \times 10^{-3} eV^2$. The deficit of the upward-going events is larger for $\nu_\mu \to \nu_\tau$ than for $\nu_\mu \to \nu_s$, because the matter effect suppresses $\nu_\mu \to \nu_s$ neutrino oscillation at small Δm^2 region.

9.1.1 Event selection

At first, we discuss the event selection. Figure 9.1 illustrates that the study of the PC sample enables us to discriminate the two possibilities. However, at large Δm^2 region, the difference for the two oscillation hypotheses is small. Thus we need to select an event sample which shows a significant difference.

According to Eq. 1.10, $\nu_\mu \to \nu_s$ oscillation is suppressed at $\zeta \gg 1$ (see Eq. 1.16). This indicates that the study on the higher energy events has an analyzing power at larger Δm^2 region. Using the value of Δm^2 at the best-fit position obtained by FC single-ring analysis, the optimum neutrino energy to separate both oscillation hypotheses is $30 \sim 100GeV$. Therefore we need to select the high-energy event out of the PC sample, because the typical energy of the PC sample ($\sim 10GeV$) is lower than the optimum energy. Although we cannot measure the neutrino energy of PC events, we can know the lower limit of the energy by using total photo-electron ($Petot$), because $Petot$ is approximately proportional to the deposit energy by secondary particles in the inner detector (9 p.e. $\sim 1MeV$). Figure 9.2 shows the relation between the cut criterion on $Petot$ and the mean neutrino energy, $\bar{E_\nu}$. This figure demonstrates $\bar{E_\nu}$ is almost a liner function of the $Petot$ cut as the following:

$$\bar{E_\nu}(GeV) = 3.7 \times 10^{-4} \times Petot(p.e.) + 9.9 \tag{9.1}$$

From this relation, $\bar{E_\nu} = 30GeV$ corresponds to $Petot \sim 54,000 p.e.$

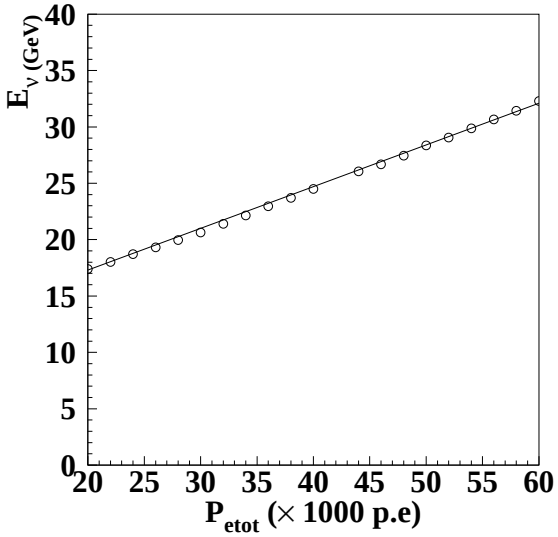

Figure 9.2: Relation between $\bar{E_\nu}$ and the cut criterion on $Petot$. The each circle shows the the mean energy of the events with more than $Petot$ and with $E_\nu < 100GeV$. The solid line shows the liner function(Eq. 9.1).

At this stage, we need to consider the fact that the ν_μ with short path length does not oscillate at such high-energies, even if $\nu_\mu \to \nu_\tau$ oscillation is the solution of the atmospheric neutrino oscillation. We, therefore, selected the events with the long path length by using the zenith angle information. In the case of upward-going events, the relation between the

neutrino path length, L_ν, and zenith angle, Θ, are expressed as $L_\nu = 2R_e|\cos\Theta|$, where R_e is the radius of the earth ($\sim 6400km$).

Additionally, we should take account of statistics of the PC event sample, because tight cuts decrease the number of the PC events. Therefore we decided the selection criteria from a Monte Carlo study considering the data statistics. As the result, the value of the $Petot$ cut was adopted to be $45,000p.e.$, which corresponds to $\bar{E}_\nu \sim 26GeV$. And the definition of upward (downward)-going events was set to be $\cos\Theta < -0.4 (> 0.4)$. In this definition, the shortest path length of the upward-going event is $\sim 5200km$, which is significantly longer than the typical oscillation length ($\sim 2000km$) for $\Delta m^2 = 3 \times 10^{-3}$. Therefore the upward-going ν_μ can oscillate into ν_τ, if the $\nu_\mu \to \nu_\tau$ oscillation occurs.

9.1.2 Summary of PC events

We summarize PC events with $Petot > 45,000p.e.$ in this subsection. Fig 9.3 shows the $Petot$ distribution for the data and MC. The MC reproduces the data distribution reasonably well. The cut is also indicated in the figure. The observed number of events with $Petot > 45,000p.e.$ was 176, and the expected one without neutrino oscillation was 234.6. Table 9.1 summarizes the fraction of each interaction mode in this sample. It is a very pure $CC\nu_\mu$ sample, and the contamination of NC and $CC\nu_e$ events is less than 1%.

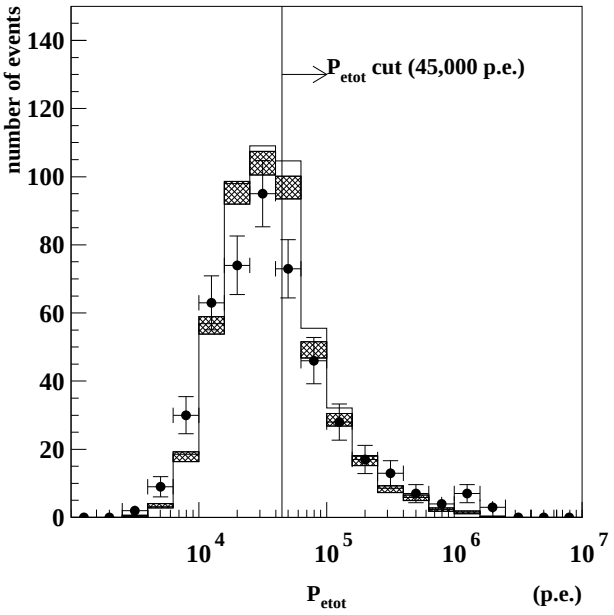

Figure 9.3: P_{etot} distribution of the PC sample. Crosses show the distribution for data, hatched histogram for $\nu_\mu \to \nu_\tau$, and solid one for $\nu_\mu \to \nu_s$. The number of events of Monte Carlo predictions are normalized by the PC livetime. Solid line shows $P_{etot} = 45,000p.e.$

$CC\nu_\mu$	q.e.	3.3 %
	1 π	7.5 %
	multi π	88.3 %
others		0.8%

Table 9.1: The fraction of each interaction mode in PC with $Petot > 45,000 p.e.$ This is estimated based on no-neutrino oscillation.

Figure 9.4 shows the observed zenith angle distribution of the PC events with $Petot > 45,000 p.e.$ and the expected distributions with and without neutrino oscillations. The expected distributions for $\nu_\mu \to \nu_\tau$ and $\nu_\mu \to \nu_s$ oscillations are for $\Delta m^2 = 3 \times 10^{-3} eV^2$ and $\sin^2 2\theta = 1$. This figure demonstrates that the $\nu_\mu \to \nu_\tau$ oscillation hypothesis reproduces the data well. The observed number of the upward(downward)-going events with $\cos\Theta < -0.4 (> 0.4)$ was 26(52). The $Up/Down$ ratio was:

$$Up/Down = \begin{cases} 0.50 \ {}^{+0.14}_{-0.11} \ (stat.) \pm 0.01_{(sys.)} & data \\ 0.94 \pm 0.04_{(stat.)} \pm 0.03_{(sys.)} & MC(no\ oscillation) \end{cases} \quad (9.2)$$

The $Up/Down$ ratio for the real data was significantly different from the Monte Carlo prediction, and was consistent with the $Up/Down$ ratio for the multi-GeV μ-like events.

9.1.3 Systematic error in the PC $Up/Down$ ratio

We discuss the systematic errors in the $Up/Down$ ratio of PC events. The considered sources of systematic error related to the data are the same as those for the FC $Up/Down$ ratio: background contamination and energy scale.

We estimated the contamination of the cosmic-ray muons as the background to the PC sample by using a χ^2 test. The χ^2 value was calculated by comparing the D_{wall} distribution of the data with that of the combined distribution of the Monte Carlo prediction and the stopping muon sample. Here, all sample satisfy $Petot$ cut ($Petot > 45,000 p.e.$) and zenith angle cut ($|\cos\Theta| > 0.4$). The obtained contamination of the cosmic-ray muon is 1.1 % at the best fit position, and 2.0 % at 1 σ level. Therefore we estimated the systematic error due to the cosmic-ray muon to be less than 2.0 %, because most of the cosmic-ray muon is downward-going. Figure 9.5 shows the D_{wall} distributions of the PC sample, the Monte Carlo prediction, and the stopping muon sample. In addition, the systematic error

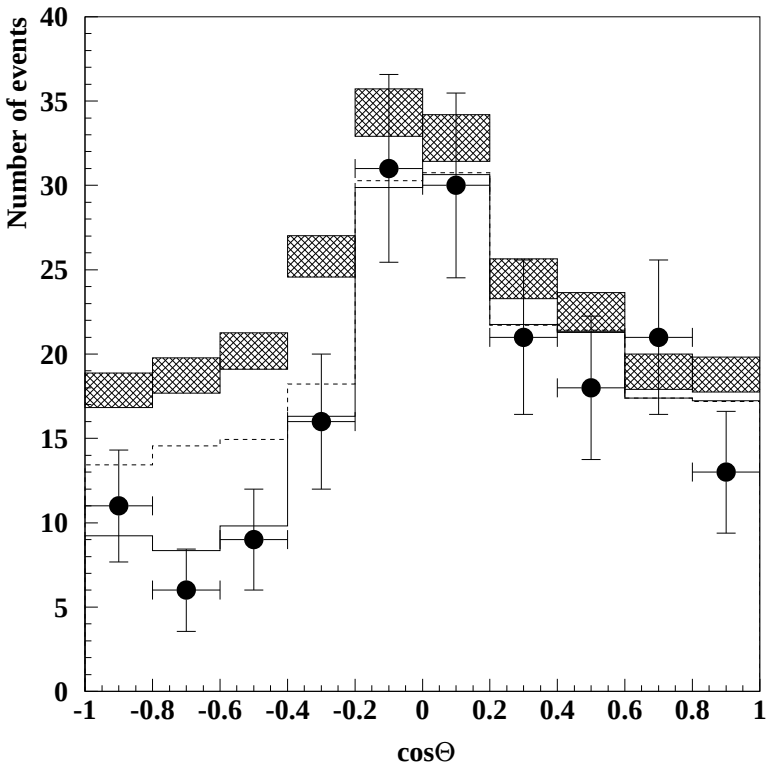

Figure 9.4: The zenith angle distributions for the PC events with $Petot > 45,000 p.e.$ The black circles show the distribution for the data. The hatched histogram shows the Monte Carlo prediction without oscillation with its statistical error. The prediction is normalized by the livetime of the PC data. The solid (broken) histogram shows the distribution for $\nu_\mu \to \nu_\tau$ ($\nu_\mu \to \nu_s$) oscillation at $\Delta m^2 = 3 \times 10^{-3}, \sin^2 2\theta = 1.0$. Both expected distriubtions share the same normalization fcator, 0.934, which was evalurated by the χ^2 test on the assumption of $\nu_\mu \to \nu_\tau$ oscillation. $\cos\Theta = -1(1)$ indicates upward(downward)-going.

arising from the possible up-down gain asymmetry of the Super-Kamiokande detector for the PC sample is estimated to be 0.9 %, which was estimated in a same way as we did for the FC single-ring sample (see Sec. 8.4).

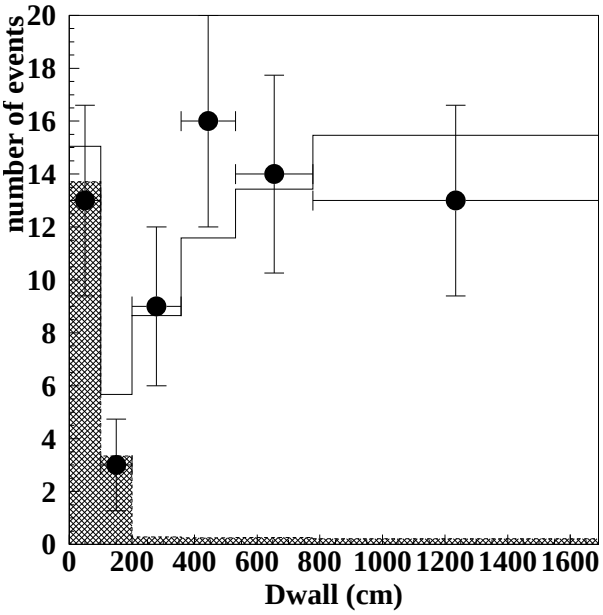

Figure 9.5: The D_{wall} distribution for the PC sample, the MC prediction and the stopping muon sample. All events were applied P_{etot} cut and zenith angle cut ($|\cos\Theta| > 0.4$). The black circles show the distribution for the observed events. The solid(hatched) histogram is for MC + stop muon sample(stopping muon) sample at the best fit + 1 σ level.

We estimated the systematic error with and without neutrino oscillation. The reason for this is that the difference in energy distribution between upward-going and downward-going events depends on neutrino oscillation. Here we used the oscillation parameter $(\sin^2 2\theta, \Delta m^2) = (1.0, 3 \times 10^{-3} eV^2)$. The comparison between the two independent flux calculations [13, 14] showed that the uncertainty coming from the ambiguity of the atmospheric neutrino flux was negligible.

The "Mt. Ikenoyama effect" was the main systematic source related to the Monte Carlo prediction, which was estimated to be 3.4 %. The systematic error from energy spectrum index of the atmospheric neutrinos was estimated to be $< 0.1\%$.

The systematic error from neutrino interaction cross section was also considered. The neutrino oscillation depends on the neutrino energy and changes the ratio of q.e./multi-pi between upward-going and downward-going events. Therefore the uncertainty in q.e./multi-pi ratio results in the uncertainty in $Up/Down$ ratio, when we take account of neutrino oscillation. This error was estimated to be the difference in $Up/Down$ ratio as we change the multi-pion production cross section by 10%. As the result, we estimated this error to be less than 0.3 %. However, the relatively large uncertainty from the neutrino interaction

source		systematic error (%)		
for data	background contamination	± 2.0		
	energy scale	± 0.9		
for MC		no-osc	$\nu_\mu \to \nu_\tau$	$\nu_\mu \to \nu_s$
	flux (Honda $\to$ Bartol)	$\ll \pm 0.1$	$\ll \pm 0.1$	$\ll \pm 0.1$
	'Mt. Ikenoyama effect'	± 3.4	± 3.4	± 3.4
	$E^{-\gamma}$	< 0.1	< 0.1	< 0.1
	neutrino interaction	0.3	0.3	0.3

Table 9.2: Systematic errors in the *Up/Down* ratio for the PC sample. The systematic error related to the Monte Carlo prediction is estimated with neutrino oscillation with $\Delta m^2 = 3 \times 10^{-3} eV^2$ and $\sin^2 2\theta = 1.0$.

cross section seems to be due to a statistic fluctuation of Monte Carlo we used to estimate. Although we have Monte Carlo events of 40 years equivalent, the number of events satisfying P_{etot} cut and zenith angle cut is only 2018. The statistical error of the difference in the q.e/multi-pi between upward-going and downward-going events is $\sim 3\%$. It means that the systematic error due to the neutrino cross section, 0.3 %, is consistent with the statistical error, because we change the q.e/multi-pi ratio by 10 %. As the result, 0.3 % error is likely to be due to the statistical error of our Monte Carlo, however we adapt this value for the systematic error coming from the uncertainty of neutrino cross section.

These systematic errors are summarized in Table 9.2.

9.1.4 Neutrino oscillation and the PC *Up/Down* ratio

We estimated the expected *Up/Down* ratio of the PC events for $\nu_\mu \to \nu_\tau$ and $\nu_\mu \to \nu_s$ oscillations at a parameter region $10^{-3.5} < \Delta m^2 < 10^{-2} eV^2$ and $\sin^2 2\theta = 1$. Figure 9.6 shows the observed *Up/Down* ratio, and the expected ones for both hypotheses. The observed ratio is consistent with that of $\nu_\mu \to \nu_\tau$ oscillation at $\Delta m^2 > 10^{-3} eV^2$ within the uncertainties. In contrast to this, the expected ratio for $\nu_\mu \to \nu_s$ oscillation is larger than the observed one at 1.5σ level at $\Delta m^2 \sim 2.5 \times 10^{-3} eV^2$.

We tried the consistency check of the $Up/Down$ ratio with both oscillation hypotheses by a χ^2 test using the $Up/Down$ ratio. A global scan was carried out at a parameter region $10^{-3.5} < \Delta m^2 < 10^{-2} eV^2$ and $\sin^2 2\theta > 0.7$, in which the 99 % allowed regions of neutrino oscillation parameters by the FC single-ring analysis are confined as shown in Fig. 8.4. The definition of χ^2_{PC} is as follows:

$$\begin{aligned} \chi^2_{pc} &= \left(Up_{data} - \alpha \;\; Up_{MC}\;(1+\frac{\epsilon}{2})\right)^2 /\sigma_U^2 \\ &+ \left(Down_{data} - \alpha \;\; Down_{MC}\;(1-\frac{\epsilon}{2})\right)^2 /\sigma_D^2 + \left(\frac{\epsilon}{\sigma_\epsilon}\right)^2 \end{aligned} \tag{9.3}$$

where $\sigma_U(\sigma_D)$ is the statistical error for upward(downward)-going events, α is a normalization factor, and ϵ is the systematic error in the $Up/Down$ ratio.

Figure 9.7 shows the 90 and 99 % C.L. contour maps obtained by the present PC analysis. The 90 and 99 % C.L. contour maps are obtained by a hypothesis test; if the χ^2 value defined in Eq. 9.3 is 2.71 (6.63), the probability that the observed large χ^2 value for 1 $d.o.f.$ is due to a statistical fluctuation is 10 (1) %. Figure 9.7 demonstrates the observed PC $Up/Down$ ratio is consistent with the expected one for $\nu_\mu \to \nu_\tau$ oscillation at $\Delta m^2 > 0.8 \times 10^{-3} eV^2$, which includes the 90 % C.L. allowed region obtained by the FC single-ring analysis completely. The fitting parametes, α and ϵ at the best fit position of the FC single-ring analysis are -10.0 % and -3.8 $\times 10^{-3}$%. Both values are smaller than their uncertainties. However the $\nu_\mu \to \nu_s$ oscillation is disfavored at 90 % C.L. at $\Delta m^2 < 2.8 \times 10^{-3} eV^2$. For this oscillation, α and ϵ at the best fit position are -21.6% and 0.11%, respectively.

9.2 Neutral current events

As described in Chapter 1, a ν_τ interacts with a nucleon via neutral current in the same way as a ν_μ dose, but by definition a ν_s dose not. Therefore the difference between the two oscillation models should be characterized by a behavior of the NC events. We studied the NC events by using the zenith angle distribution of FC multi-ring events. In the case of $\nu_\mu \to \nu_\tau$ oscillation, the zenith angle distribution of NC events should be approximately up-down symmetric. In the case of $\nu_\mu \to \nu_s$ oscillation, in contract to this,

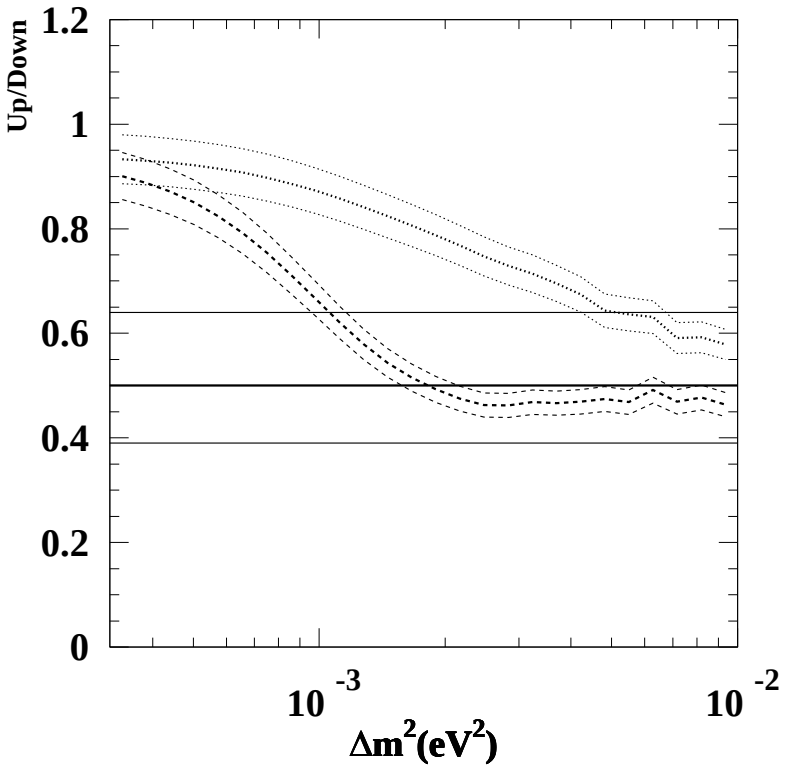

Figure 9.6: *Up/Down* for the PC sample as a function of Δm^2 at $\sin^2 2\theta = 1$. Each thick line shows the *Up/Down* ratio, and thin lines show the $\pm 1\sigma$ error. Broken curves show the expected values for $\nu_\mu \to \nu_\tau$ oscillation, and dotted curves for $\nu_\mu \to \nu_s$. The solid lines show the observed values.

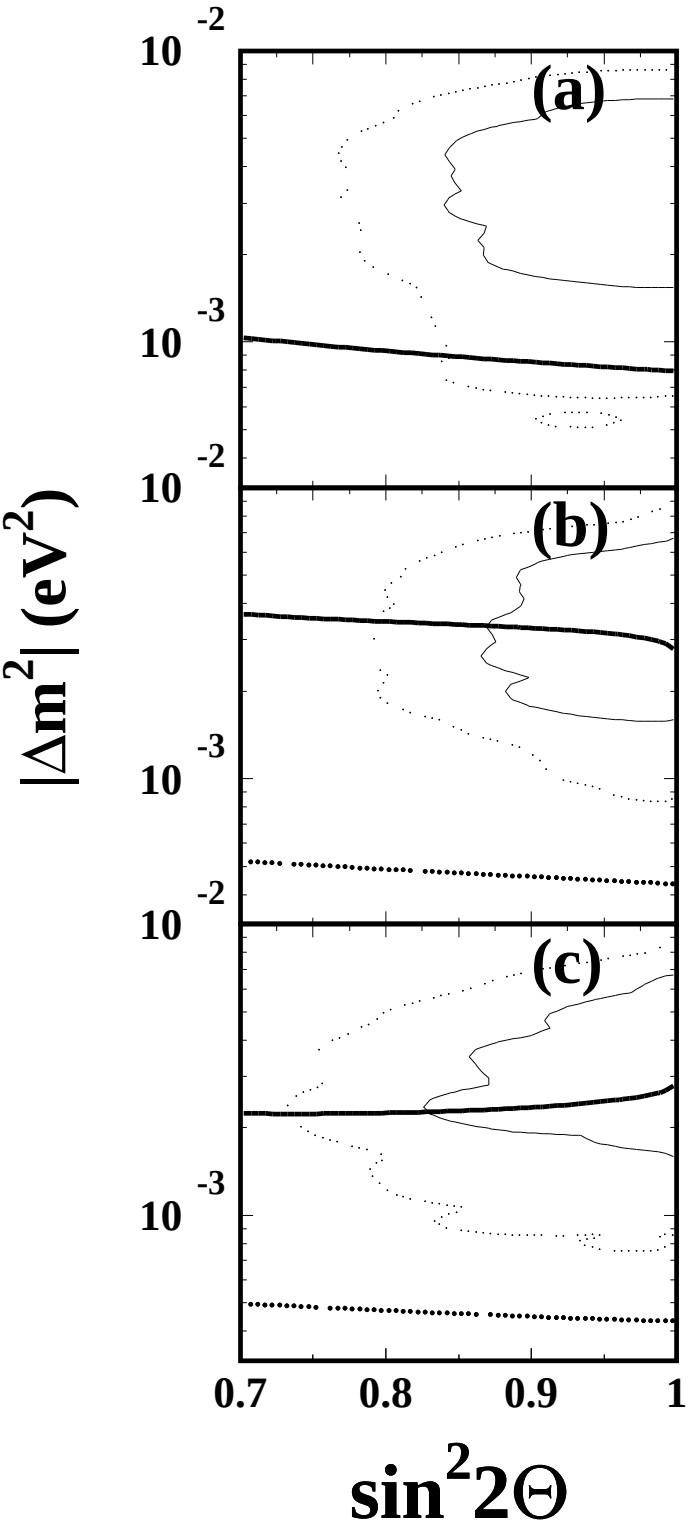

Figure 9.7: Contour maps using the PC *Up/Down* ratio; (a) for $\nu_\mu \to \nu_\tau$ oscillation, (b) for $\nu_\mu \to \nu_s(\Delta m^2 > 0)$, and (c) for $\nu_\mu \to \nu_s(\Delta m^2 < 0)$. Regions inside the thin solid(dotted) curves show the 90(99) % C.L. allowed parameter regions from the FC single-ring-analysis. Regions below the thick solid (dashed) curves are excluded at 90(99) % C.L. by the PC analysis.

the upward-going events produced via the NC interaction should have deficit compared to the downward-going ones. Thus the study of the NC $Up/Down$ ratio is also useful.

In some cases, π° events are used for NC study, because it is relatively easy to identify using invariant mass. However, π° events are not useful to compare the rates of upward-going and downward-going events. As described in Appendix B, most of the reconstructed π°'s are low energy. Most of them are produced via single π production. In this interaction, the Δ produced by the neutrino interaction immediately decays into N and π. The direction of emitted π is almost isotropic at the center of the mass system of the Δ resonance. Accordingly reconstructed π°'s barely keep the directional information of primary neutrinos. Therefore we tried another approach to select NC events.

In this section, we discuss the $Up/Down$ ratio of multi-ring events to discriminate $\nu_\mu \to \nu_\tau$ and $\nu_\mu \to \nu_s$ oscillation hypotheses. This study is almost independent of the uncertainty of the atmospheric neutrino flux and NC interaction cross section. The reason why we used the multi-ring sample to study NC will be presented in the section of the event selection.

For the FC multi-ring analysis, we should consider $CC\nu_\tau$ induced events, because most of ν_τ induced events are classified as multi-ring events. We made the MC ν_τ events, and analyzed them in the same way as we did for the real data. Table 9.3 summarizes the expected number of τ events in a year with neutrino oscillation with $\Delta m^2 = 5(1) \times 10^{-3} eV^2$ and $\sin^2 2\theta = 1$.

9.2.1 Event selection

As described in the previous section, the study on the PC $Up/Down$ ratio was useful at relatively small Δm^2. This study disfavored $\nu_\mu \to \nu_s$ oscillation at $\Delta m^2 \lesssim 3 \times 10^{-3} eV^2$ at 90 % C.L.

For $\Delta m^2 \gtrsim 3 \times 10^{-3} eV^2$ and for $E_\nu \lesssim (a\,few) GeV$, the matter effect is negligibly small. In this case, the neutrino oscillation probabilities are essentially the same between the $\nu_\mu \to \nu_\tau$ and $\nu_\mu \to \nu_s$ oscillation hypotheses. Therefore the study of the NC $Up/Down$ ratio is expected to be powerful even for $\Delta m^2 \gtrsim 3 \times 10^{-3} eV^2$.

In this study, we have to enrich NC events and reject $CC\nu_\mu$ events which show an

		Δm^2 (eV^2)	
		5×10^{-3}	1×10^{-3}
sub-GeV	1R	0.70	0.65
	e-like	0.55	0.50
	μ-like	0.15	0.15
	2R	0.75	0.50
	$\geq$3R	1.00	0.75
multi-GeV	1R	4.60	2.85
	e-like	3.95	2.30
	μ-like	0.65	0.55
	2R	4.50	2.35
	$\geq$3R	6.00	3.05

Table 9.3: The expected ν_τ induced events in the fiducial volume in one year exposure of the Super-Kamiokande detector.

up-down asymmetry. Therefore we applied two cuts, $Nring$ cut and PID_{max} cut.

First we introduce $Nring$ cut. Figure 9.8 (a) shows the number of ring distribution for the NC and all events. Figure 9.8 (b) shows that the fraction of NC events in multi-ring events is about 25 %, though single-ring events are mostly composed of CC events. Therefore we used multi-ring events to enrich NC events.

Next, PID_{max} cut is described, where PID_{max} is the PID result for the most energetic Cherenkov ring. Figure 9.9 illustrates the interaction producing multi-ring events for $CC\nu_\mu$ and NC interactions. In the case of NC interaction, we detect the Cherenkov light emitted by π. A π° produces more Cherenkov light than a $\pi^\pm$ of the same energy. A π° is identified as an e-like event (or a two e-like-ring event). Hence, the particle type of the most energetic ring, PID_{max}, is identified as e-like. In contract to this, for $CC\nu_\mu$ events, in most cases, μ produces most energetic ring, and PID_{max} is μ-like. Therefore we require that PID_{max} is e-like. Figure 9.10 (a) shows the likelihood function for the most energetic ring in the multi-ring sample. If the PID likelihood is positive(negative), a particle is μ-like(e-like). 2/3 of $CC\nu_\mu$ events are identified as μ-like as shown in Fig.

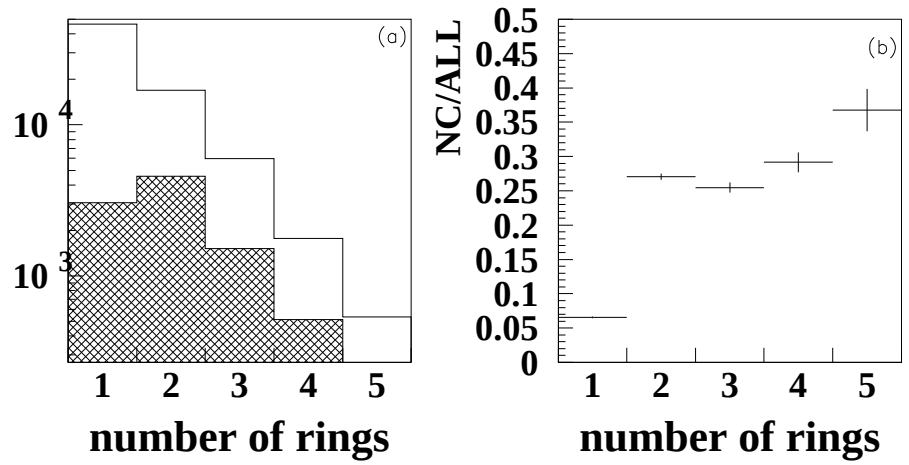

Figure 9.8: Number of ring distribution. (a) shows the number of ring distribution. Hatched (blank) histogram shows the NC(all) events. (b) shows the fraction of NC events.

9.10 (b), therefore PID_{max} cut is useful to reject $CC\nu_\mu$ events.

Finally we apply E_{vis} cut to reject the low energy events, and decide the definition of the upward (downward)-going events. Figure 9.11 shows the E_{vis} distribution of the events satisfy $Nring$ cut and PID_{max} cut. This figure shows our Monte Carlo with neutrino oscillation reproduces the data distribution.

Here, we define the direction of the reconstructed total momentum for the multi-ring events, $\vec{d_m}$:

$$\vec{d_m} = \frac{\sum_i \vec{p_i}}{|\sum_i \vec{p_i}|} \tag{9.4}$$

where $\vec{p_i}$ is the momentum of an electron that would produced the observed amount of Cherenkov light of the i-th ring. Figure 9.12 shows an angular correlation between the $\vec{d_m}$ and the neutrino direction as a function of the visible energy, E_{vis}.

The angular correlation between the direction of the primary neutrino and the reconstructed one gets worse with lowering the neutrino energy. We, however, only use the $Up/Down$ ratio, and the angular correlation is not required to be very good. Of course the requirement to the angular correlation is dependent on the definition of the upward (downward)-going events. Therefore we decided the criteria of E_{vis} cut and the upward (downward)-going events from the Monte Carlo study in the similar way as we did in PC

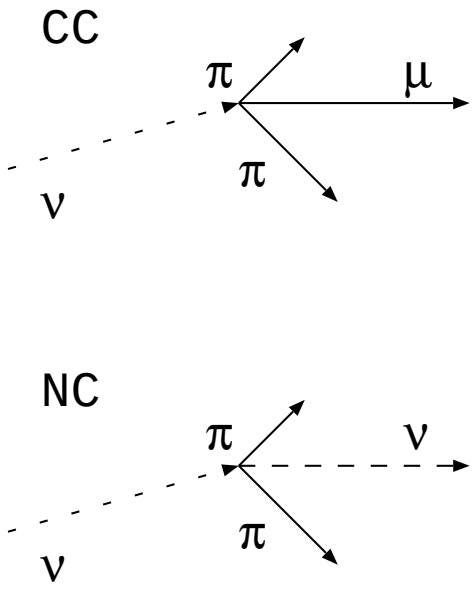

Figure 9.9: Illustration of multi-ring events. Solid lines show the particles which produce Cherenkov ring. Dashed lines show ν and they are invisible.

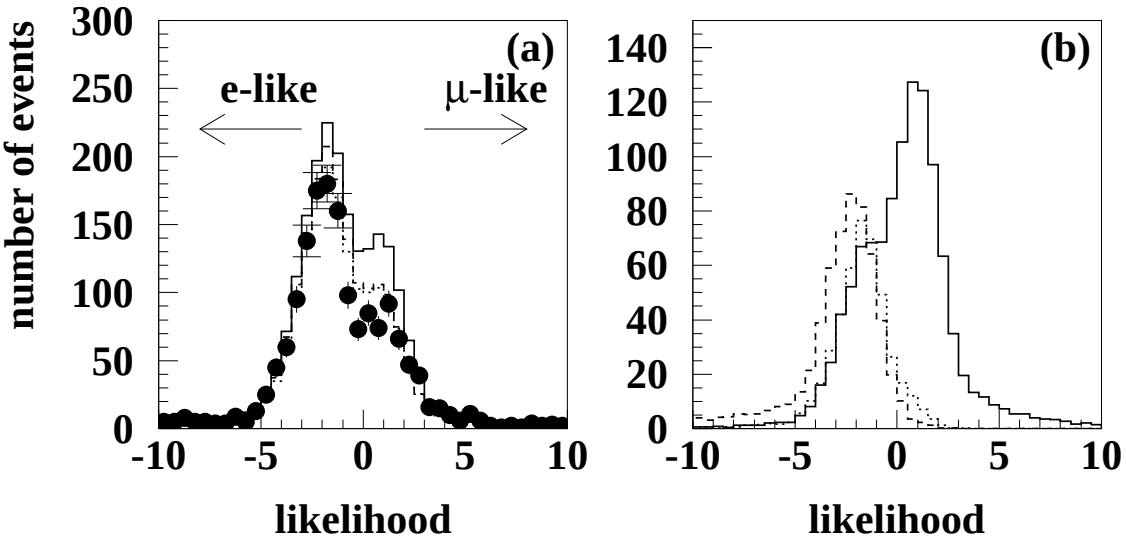

Figure 9.10: The PID likelihood distribution for the most energetic ring, PID_{max}, of multi-ring events. In (a), black circles are the data, solid, broken, and dotted histogram are the MC prediction for no-oscillation, $\nu_\mu \to \nu_\tau(\Delta m^2 = 3 \times 10^{-3}, \sin^2 2\theta = 1.0)$, and $\nu_\mu \to \nu_s(\Delta m^2 = 3 \times 10^{-3}, \sin^2 2\theta = 1.0)$, respectively. In (b), solid histogram shows PID_{max} for $CC\nu_\mu$ event, broken for $CC\nu_e$, dotted for NC. The e-like events due to $CC\nu_\mu$ in (b) are mainly multi-hadron production events with many Cherenkov rings overlapped.

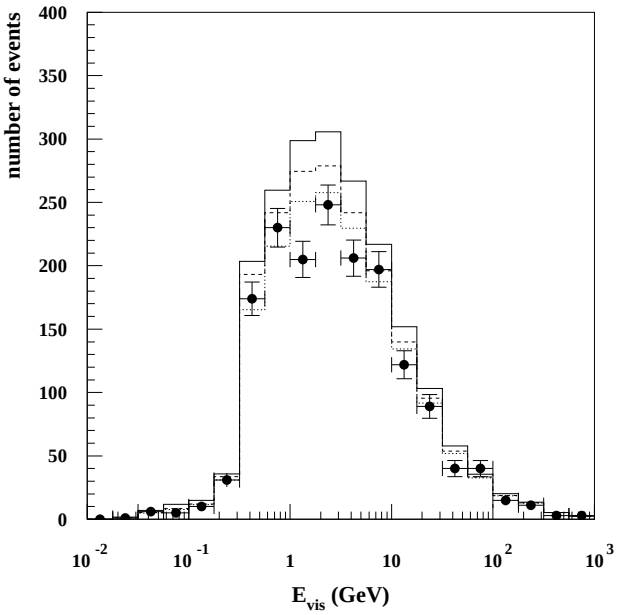

Figure 9.11: E_{vis} distribution. All samples are applied $Nring$ and PID_{max} cut. Black circles are the data. Solid, broken, and dotted histogram are the MC prediction for no-oscillations, $\nu_\mu \to \nu_\tau(\Delta m^2 = 3 \times 10^{-3}, \sin^2 2\theta = 1.0)$, and $\nu_\mu \to \nu_s(\Delta m^2 = 3 \times 10^{-3}, \sin^2 2\theta = 1.0)$, respectively.

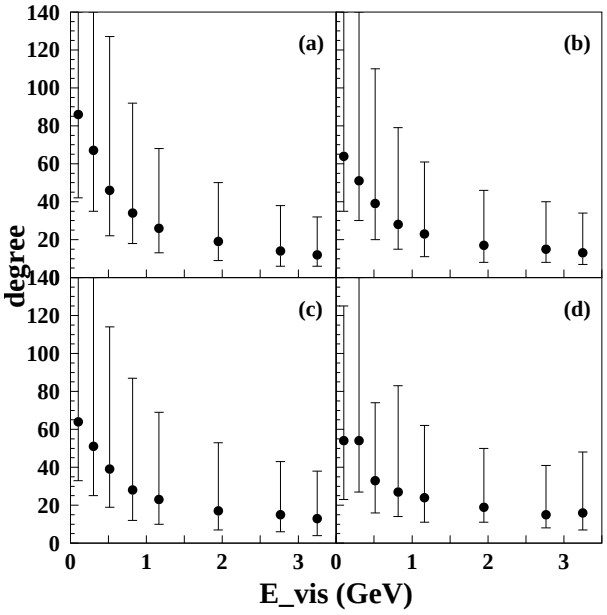

Figure 9.12: The angular correlation between the reconstructed direction, $\vec{d_m}$, and the neutrino direction as a function of E_{vis}. (a) shows the correlation for $CC\nu_e$ induced events; (b) for $CC\nu_\mu$; (c) for NC; (d) for $CC\nu_\tau$.

mode	$\nu_\mu \to \nu_\tau$	$\nu_\mu \to \nu_s$
$CC\nu_\mu$	17 %	20 %
$CC\nu_e$	48 %	54 %
$CC\nu_\tau$	3 %	-
NC	32 %	26 %

Table 9.4: Summary of multi-ring events satisfying the multi-ring cuts. The fraction for each component is calculated on the assumption of $\Delta m^2 = 3 \times 10^{-3} eV^2$ and $\sin^2 2\theta = 1$.

$Up/Down$ analysis. We set the cut values so that a statistically maximum separation is obtained at $\sin^2 2\theta = 1.0$ and $\Delta m^2 \sim 7 \times 10^{-3} eV^2$ which is the upper limit of allowed Δm^2 region from the FC single-ring analysis. In this analysis, we considered the matter effect and the contribution of $CC\ \nu_\tau$ events. As the result, we adopted $E_{vis} > 400 MeV$ and $\cos\Theta < -0.4 (> 0.4)$ for the definition of upward (downward)-going events.

In summary, we applied the following cuts to study the $NC\ Up/Down$ ratio.

1. Nring > 1
2. PID_{max} is e-like.
3. $E_{vis} > 400 MeV$

The number of the observed events satisfying the above criteria was 1173, of which 324(310) were upward(downward)-going events. And the corresponding number of events in the Monte Carlo is 1465.0 for no neutrino oscillation. Figure 9.13 shows the zenith angle distribution of the events satisfying the above condition. Table 9.4 summarizes the fraction of each interaction mode satisfying the above cuts. Those cuts enrich NC events and reduce $CC\ \nu_\mu$ ones.

We calculated the $Up/Down$ ratio of the multi-ring events as:

$$Up/Down = \begin{cases} 1.05\ ^{+\,0.09}_{-\,0.08}\ _{(stat.)} \pm 0.006_{(sys.)} & data \\ 1.00 \pm 0.02_{(stat.)} \pm 0.03_{(sys.)} & MC(no\ oscillation) \end{cases}$$

9.2.2 Systematic error in $Up/Down$ ratio for multi-ring sample

We estimated the systematic error in the $Up/Down$ ratio for the multi-ring sample in the same way as we did for the PC sample. First, we checked the systematic errors for the

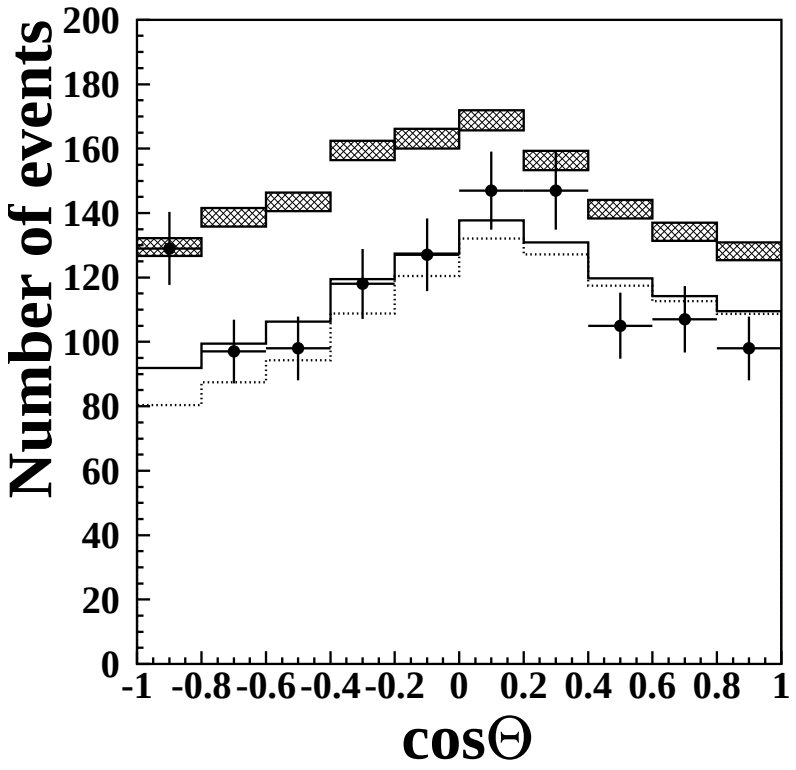

Figure 9.13: Zenith angle distributions of the multi-ring events satisfying the PID_{max} and the E_{vis} cuts. The black circles show the distribution for the data. The hatched histogram shows the Monte Carlo prediction with no-oscillation with its statistical error. The prediction is normalized by the livetime of the FC data. The broken(dotted) histogram shows the distribution for $\nu_\mu \to \nu_\tau$ ($\nu_\mu \to \nu_s$) oscillation at $\Delta m^2 = 3 \times 10^{-3}, \sin^2 2\theta = 1.0$. Both expected distributions share the same normalization factor, 0.862, which obtained by the χ^2 test on the assumption of $\nu_\mu \to \nu_\tau$ oscillation. $\cos\Theta = -1(1)$ indicates upward(downward)-going.

observed $Up/Down$ ratio. The background contamination was estimated as follows. As mentioned in the FC analysis (Sec. 8.2.3), the possible background sources were cosmic-ray stopping muons and flashing PMT's for single-ring events. Among them only, "flashing PMT" events were considered as a possible source of the background to the multi-ring sample, because cosmic-ray muons are almost always single-ring events. Even if they are classified as multi-ring sample, they are rejected by the PID_{max} cut. We analyzed these "flashing PMT" events in the same way we did for the data to study the behavior of them. These events were all typical "flashing PMT" event and were rejected by eye-scanning. We estimated the upper limit of the contamination of these events in multi-ring sample as the following, on the assumption these events may not be rejected by the eye-scanning. The upper limit of the contamination of these "flashing PMT" events in the fiducial volume were estimated to be 0.5% for single-ring e-like events(See Sec. 8.2.3). Therefore, the number of these events in FC single-ring e-like sample is estimated to be 11.3 events. The ratio of (multi)/(single-e) of the "flashing PMT" events is 0.094, therefore the expected number of contamination of "flashing PMT" events in multi-ring sample is 1.1 events. As the result, the upper limit of the contamination of "flashing PMT" events in multi-ring events is estimated to be 0.09 %. Figure 9.14 shows the D_{wall} distribution of multi-ring events, and it illustrates no excess due to the background contamination in the multi-ring events.

The possible gain asymmetry of the detector for upward-going was estimated to caused 0.4 % uncertainty in the $Up/Down$ ratio.

Next, we considered the systematic errors related to the Monte Carlo prediction. We assumed the neutrino oscillation in the same way we did for PC events. The difference between the two independent calculations [13, 14] was 0.8%. The "Mt. Ikenoyama" effect caused 2.6 % uncertainty in the $Up/Down$ ratio. Moreover, we estimated the uncertainty due to the energy index of the primary neutrino flux. This value is $< 0.1\%$ for all cases.

We considered the uncertainty related to the neutrino cross section. The uncertainty was defined as the change of $Up/Down$, when we increase the NC cross section by 20%. In the case of no-oscillation, the uncertainty is 0.3%. The main cause of this error was mainly the statistical fluctuation of our Monte Carlo, though the uncertainty of the neutrino cross section should be canceled by taking the $Up/Down$ ratio for no neutrino oscillation. In

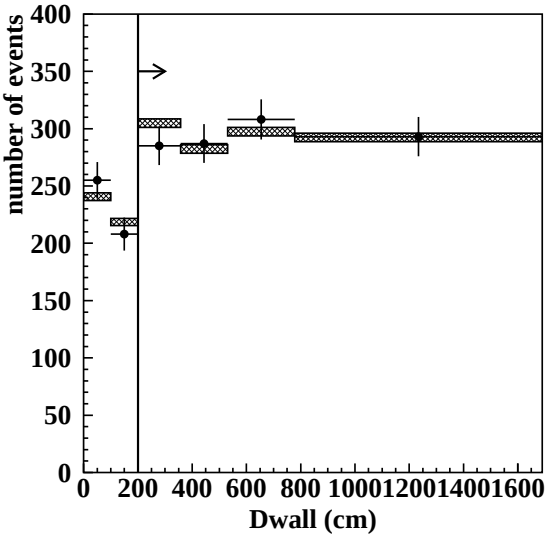

Figure 9.14: The D_{wall} distribution for the FC multi-ring events; black circles for the data, histogram for the Monte Carlo prediction. The event number of the Monte Carlo prediction is normalized by that of the PC sample. Solid line shows the D_{wall} cut criterion.

the case of oscillation ($\Delta m^2 = 3 \times 10^3 eV^2, \sin^2 2\theta = 1.0$), the up-down symmetry is broken by the deficit of upward-going events. The uncertainty is 0.9% and 0.3% for $\nu_\mu \to \nu_\tau$ and $\nu_\mu \to \nu_s$ hypotheses, respectively. Although these values also contain the MC statistical error, dominant uncertainty is thought to be due to the uncertainty of the neutrino interaction cross section.

As a result, we confirmed that the study of up-down asymmetry is almost independent of the uncertainties related to the neutrino cross section or neutrino fluxes. These systematic errors are summarized in Table 9.5.

9.2.3 Neutrino oscillation and the multi-ring $Up/Down$ ratio

We calculated the expected $Up/Down$ ratio for both oscillation hypotheses. Figure 9.15 shows the expected $Up/Down$ ratio as a function of Δm^2, where we assume $\sin^2 2\theta = 1$. The matter effect is taken into account for $\nu_\mu \to \nu_s$.

The data disfavored $\nu_\mu \to \nu_s$ hypothesis at $\Delta m^2 \sim 10^{-2} eV^2$ by about 3 σ. $\nu_\mu \to \nu_\tau$ hypothesis was away from the data by $1.5 \sim 2.0$ σ. However, the agreement between the data and $\nu_\mu \to \nu_\tau$ hypothesis is better than that between the data and $\nu_\mu \to \nu_s$ hypothesis.

We calculated χ^2_{multi} values for both hypotheses. The definition of χ^2_{multi} is the similar

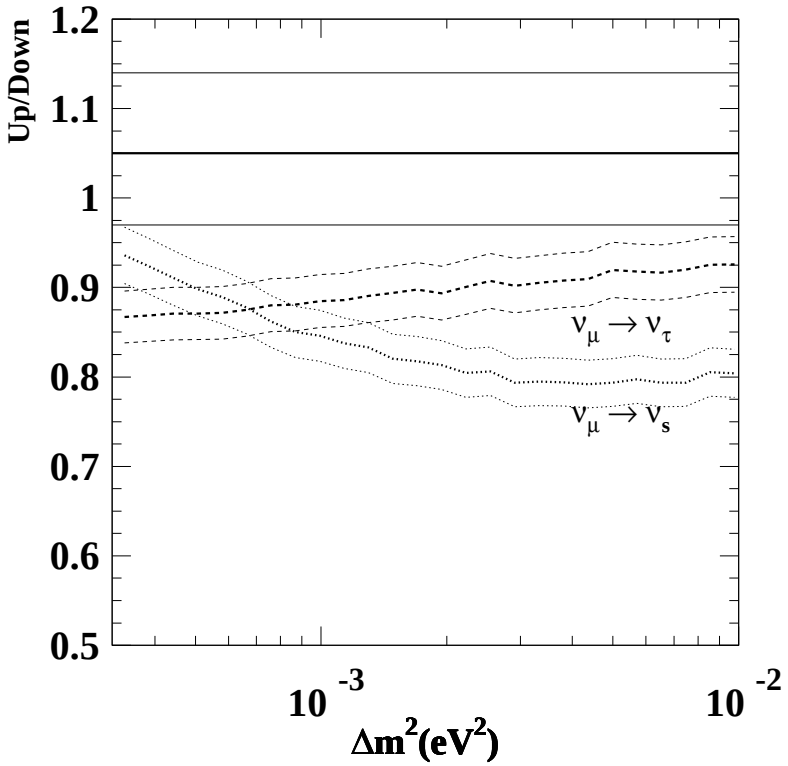

Figure 9.15: *Up/Down* for the multi-ring sample as a function of Δm^2 at $\sin^2 2\theta = 1$. Each thick line shows the *Up/Down* ratio, and thin lines show $\pm 1\sigma$ error. Broken lines show the expected values for $\nu_\mu \rightarrow \nu_\tau$ oscillation, and dashed lines for $\nu_\mu \rightarrow \nu_s$. The solid lines show the observed values.

source		systematic error (%)		
for data	background contamination	$< \pm 0.3$		
	energy scale	± 0.4		
for MC		no-osc	$\nu_\mu \to \nu_\tau$	$\nu_\mu \to \nu_s$
	flux (Honda $\to$ Bartol)	± 0.8	± 0.8	± 0.8
	'Mt. Ikenoyama effect'	± 2.6	± 2.6	± 2.6
	$E^{-\gamma}$	$< \pm 0.1$	$< \pm 0.1$	$< \pm 0.1$
	neutrino interaction	0.3	0.9	0.3

Table 9.5: Systematic errors in the $Up/Down$ ratio for the multi-ring sample. The systematic error related to the Monte Carlo prediction is estimated with neutrino oscillation with $\Delta m^2 = 3 \times 10^{-3} eV^2$ and $\sin^2 2\theta = 1.0$. Assuming that these "flashing PMT" events may have a strong directionality, the uncertainty in the $Up/Dwon$ ratio due to background contamination should be less than 0.3%.

to χ^2_{PC}.

$$\begin{aligned} \chi^2_{multi} &= \left(Up_{data} - \alpha \;\; Up_{MC}\;(1 + \frac{\epsilon}{2})\right)^2 / \sigma_U^2 \\ &+ \left(Down_{data} - \alpha \;\; Down_{MC}\;(1 - \frac{\epsilon}{2})\right)^2 / \sigma_D^2 + \left(\frac{\epsilon}{\sigma_\epsilon}\right)^2 \end{aligned} \tag{9.5}$$

where $\sigma_U(\sigma_D)$ is the statistical error for upward(downward)-going events, α is a normalization factor, and ϵ is the systematic error in the $Up/Down$ ratio.

Figure 9.16 shows the 90 and 99 % C.L. contour maps obtained by the multi-ring analysis. The observed $Up/Down$ ratio does not conflict with $\nu_\mu \to \nu_\tau$ oscillation for $\Delta m^2 > 2 \times 10^{-3} eV^2$. The fitting parameters, α and ϵ at the best fit position of the FC single-ring analysis are -16.0 % and -1.7 %, respectively. Both values are within their uncertainties. On the other hand, $\nu_\mu \to \nu_s$ oscillation is disfavored at 99% C.L for a significant fraction of the allowed region obtained by the FC single-ring analysis.

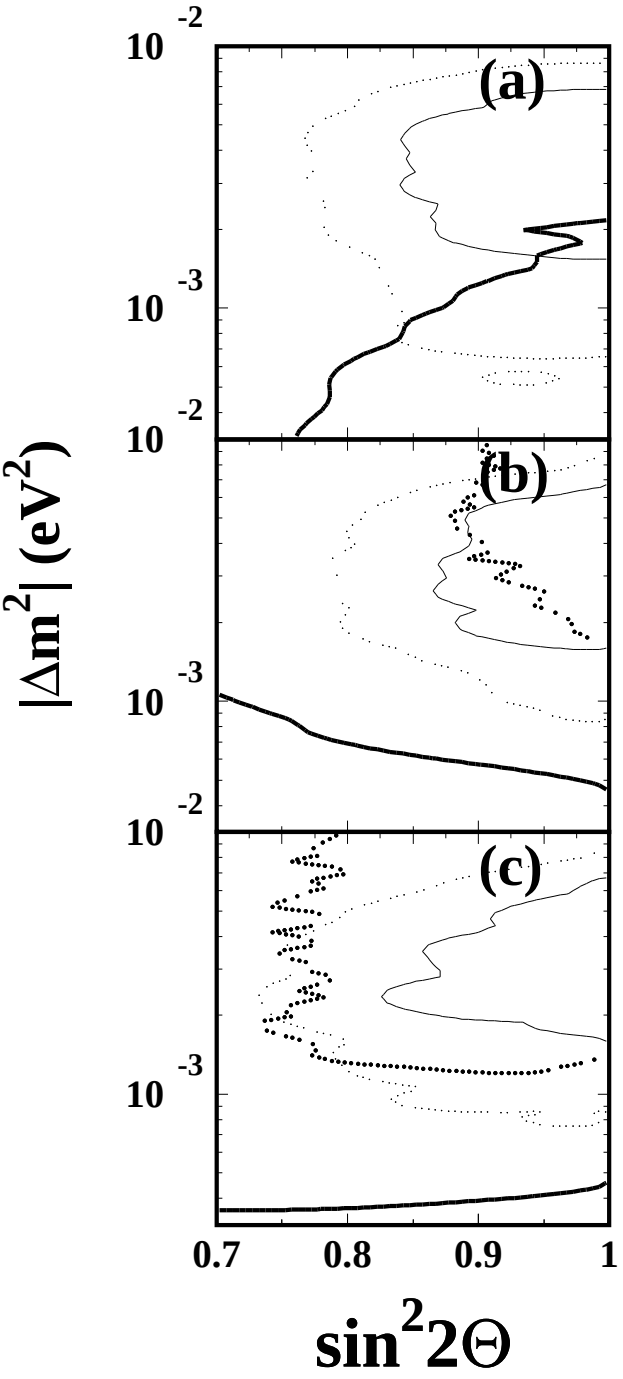

Figure 9.16: Contour maps using the multi-ring *Up/Down* ratio; (a) for $\nu_\mu \to \nu_\tau$ oscillation, (b) for $\nu_\mu \to \nu_s(\Delta m^2 > 0)$, and (c) for $\nu_\mu \to \nu_s(\Delta m^2 < 0)$. Regions inside the thin solid(dotted) curves show the 90(99) % C.L. allowed parameter regions from the FC single-ring analysis. For $\nu_\mu \to \nu_\tau$, region below the thick solid curve is excluded at 90% C.L. by the multi-ring analysis. For $\nu_\mu \to \nu_s$, regions above the thick solid (dashed) curves are excluded at 90(99) % C.L. by the multi-ring analysis.

9.3 Combined analysis

In this thesis, we studied the distinction of $\nu_\mu \to \nu_\tau$ from $\nu_\mu \to \nu_s$ by the PC events and FC multi-ring events. In the case of $\nu_\mu \to \nu_\tau$ oscillations, the $Up/Down$ ratios of the PC and FC multi-ring samples are both consistent with the observed ones within uncertainties as we have shown. However the multi-ring $Up/Down$ ratio disfavors a significant fraction of the parameter region allowed by the FC single-ring analysis at 99 % C.L. And the PC $Up/Down$ ratio supports the result of the multi-ring analysis.

Finally, we show a result of a combined analysis of the PC and multi-ring analyses. The definition of χ^2 for combined analysis is:

$$\chi^2_{cmb} = \chi^2_{PC} + \chi^2_{multi} \tag{9.6}$$

Figure 9.17 shows the 90 and 99 % C.L. contour maps of χ^2_{cmb} for each oscillation hypothesis. Here 90 and 99 % C.L. are defined to be at $\chi^2_{cmb} = 4.61$ and 9.21, since χ^2_{cmb} has 2 d.o.f. The combined analysis demonstrates that the $Up/Down$ ratios of PC and FC multi-ring samples are consistent with FC single-ring analysis for $\nu_\mu \to \nu_\tau$, and indicates that $\nu_\mu \to \nu_\tau$ oscillation is the solution of the atmospheric neutrino oscillation. For $\nu_\mu \to \nu_s$, in contract to this, there is almost no allowed region at 99 % C.L in the 90 % C.L. allowed region obtained by the FC single-ring analysis.

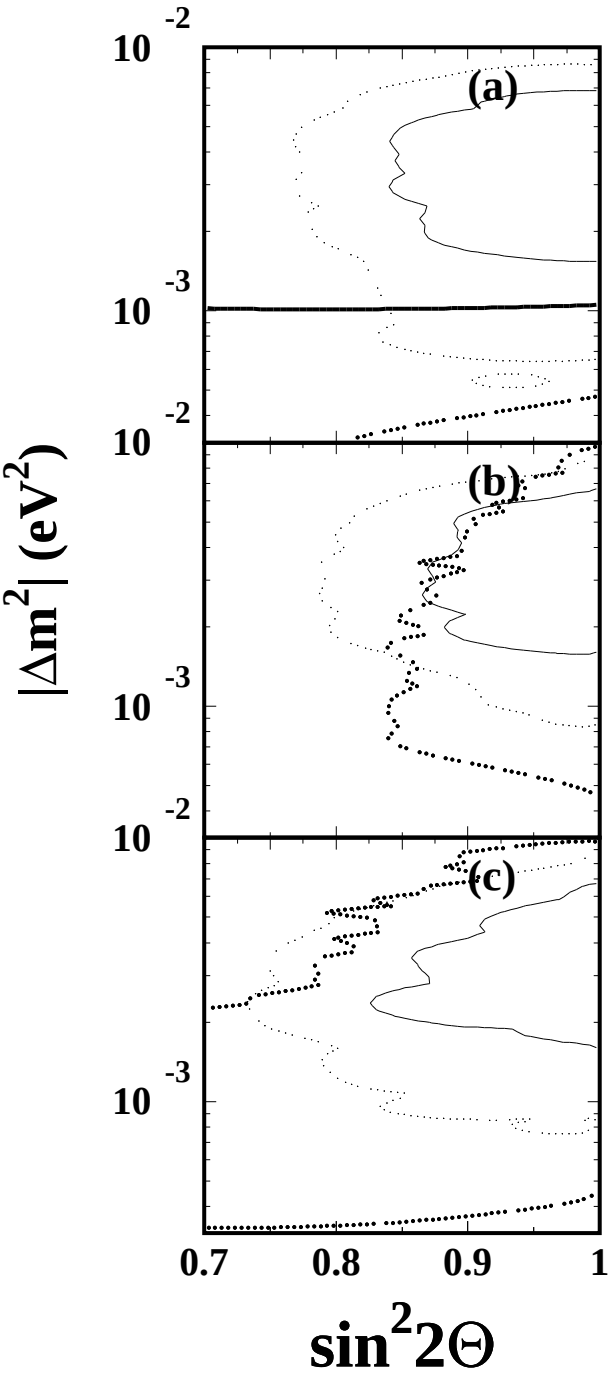

Figure 9.17: Contour maps obtained by the combined analysis of PC and multi-ring events; (a) for $\nu_\mu \to \nu_\tau$ oscillation, (b) for $\nu_\mu \to \nu_s(\Delta m^2 > 0)$, and (c) for $\nu_\mu \to \nu_s(\Delta m^2 < 0)$. Regions inside the thin solid(dotted) curves show the 90(99) % C.L. allowed parameter regions from the FC single-ring analysis. For $\nu_\mu \to \nu_\tau$ hypothesis, a regions below the thick solid (dashed) curves is excluded at 90(99) % C.L. by the combined analyses. For $\nu_\mu \to \nu_s$ hypothesis, a region surrounded by dashed curves are excluded at 99 % C.L. All the regions in $\sin^2 2\theta > 0.7$ and $3 \times 10^{-4} < \Delta m^2 < 1 \times 10^{-2}$ are excluded at 90% C.L.

Chapter 10

Conclusion

We measured the atmospheric neutrino events in Super-Kamiokande. We observed 6982 (470) events for the fully contained (partially contained) sample with an exposure of 52 kton year.

We obtained the $(\mu/e)_{data}/(\mu/e)_{MC}$ ratio, R, and the Up/Down ratio from the FC single-ring events:

$$
\begin{aligned}
R &= \begin{cases} 0.68 \ ^{+\,0.023}_{-\,0.022} \ (stat.) \pm 0.05_{(sys.)} & \text{sub-GeV} \\ 0.68 \ ^{+\,0.050}_{-\,0.047} \ (stat.) \pm 0.09_{(sys.)} & \text{multi-GeV} \end{cases} \\
Up/Down &= \begin{cases} 1.101 \ ^{+\,0.059}_{-\,0.056} \ (stat.) \pm 0.011_{(sys.)} & \text{sub-GeV } e\text{-like} \\ 0.764 \ ^{+\,0.041}_{-\,0.039} \ (stat.) \pm 0.002_{(sys.)} & \text{sub-GeV } \mu\text{-like} \\ 0.994 \ ^{+\,0.116}_{-\,0.103} \ (stat.) \pm 0.010_{(sys.)} & \text{multi-GeV } e\text{-like} \\ 0.519 \ ^{+\,0.070}_{-\,0.062} \ (stat.) \pm 0.007_{(sys.)} & \text{multi-GeV } \mu\text{-like} \end{cases}
\end{aligned}
\tag{10.1}
$$

We found that these data can be consistently explained by either $\nu_\mu \to \nu_\tau$ or $\nu_\mu \to \nu_s$ oscillations. According to the FC single-ring analysis, the best fit parameters to the two oscillation hypotheses are $(\sin^2 2\theta, \Delta m^2) = (1.0, 3 \times 10^{-3})$ for both $\nu_\mu \to \nu_\tau$ and $\nu_\mu \to \nu_s$ oscillations. And the observed data are in good agreement with both hypotheses with $\sin^2 2\theta > 0.83$ and $1.5 \times 10^{-3} < \Delta m^2 < 7 \times 10^{-3} eV^2$ at 90% C.L.

Then we tried to discriminate $\nu_\mu \to \nu_\tau$ and $\nu_\mu \to \nu_s$. We studied the distinction of

the two hypotheses by using the PC sample and FC multi-ring sample. The study of the PC events showed that there is a significant difference in the expected Up/Down ratio between the two hypotheses due to the matter effect. We obtained that the Up/Down ratio of the PC events with $Potot > 45,000 p.e.$ was:

$$Up/Down = 0.50 \ {}^{+\,0.135}_{-\,0.109} \ (stat.) \pm 0.01(sys.) \tag{10.2}$$

This result disfavored the $\nu_\mu \to \nu_s$ oscillation hypothesis at small Δm^2 of $\lesssim 3.0 \times 10^{-3} eV^2$ at 90 % C.L.

For the study of FC multi-ring events, we also used the $Up/Down$ ratio in the same way we did for PC sample to distinguish the two hypotheses. The $Up/Down$ ratio of the FC multi-ring sample was

$$Up/Down = 1.05 \pm \ {}^{+\,0.09}_{-\,0.08} \ (stat.) \pm 0.006_{(sys.)} \tag{10.3}$$

This result disfavored $\nu_\mu \to \nu_s$ oscillation hypothesis at 99% C.L. for a significant faction of the allowed region at 90 % C.L. obtained by the FC single-ring analysis.

Finally, by the combined analysis of the PC and multi-ring events, we conclude that the $\nu_\mu \to \nu_s$ oscillation hypothesis as the solution of the atmospheric neutrino problem is disfavored at 99 % C.L. for most of the region indicated by the FC single-ring analysis.

Appendix A

Upward through-going muon

A.1 Outline

As described in Chapter 1, $\nu_\mu \to \nu_s$ neutrino oscillation is suppressed by the MSW effect at a high energy region. We studied this effect by using the PC sample, and found that $\nu_\mu \to \nu_s$ oscillation is disfavored at 90 % C.L. at $\Delta m^2 < 3 \times 10^{-3} eV^2$ as described in Sec. 9.1.

This suppression by the matter effect depends on Δm^2 and the neutrino energy. In the PC up/down analysis, we selected the high-energy PC events by applying the total photo-electron cut. A still tighter cut is required to distinguish the both hypotheses at larger Δm^2 region. However we loose the statistics of the PC sample rapidly with the tighter cut. Therefore we need an event sample with higher neutrino energy and higher statistics.

Super-Kamiokande can detect the through-going muon produced by the high energy ν_μ in the surrounding rock. The typical neutrino energy of this sample is $\sim 100 GeV$, and the number of events of this sample is a factor 6 more than that of upward-going PC sample. Therefore this sample is useful to discriminate the two oscillation hypotheses by using the matter effect at $\Delta m^2 \sim 0.01 eV^2$ [59, 60, 61].

In the analysis, we use the upward through-going muons. This reason is that most of downward through-going events are the cosmic ray muons, and that it is impossible to select the neutrino-induced events out of the downward-going sample.

In this thesis, we don't describe the event reconstruction procedure, because the details of it are described in [110].

A.2 Event summary

We observed 1028 upward through-going muons during 923 detector live days. The expected background due to cosmic ray muons is 7.4 events and this background is subtracted from the bin $-0.1 < \cos\Theta < 0$ in the following analysis. From this data sample, the flux of the through-going muon was calculated to be $1.70 \pm 0.05 \pm 0.02 \times 10^{-13} cm^{-2} s^{-1} sr^{-1}$. The expected flux without neutrino oscillation was $1.84 \pm 0.41 \times 10^{-13} cm^{-2} s^{-1} sr^{-1}$ based on Honda-flux [13]. This expected flux was obtained by the numerical analysis. Figure A.1 shows the zenith angle distribution of through-going muon flux with the calculated zenith angle distribution based on the Honda flux [13].

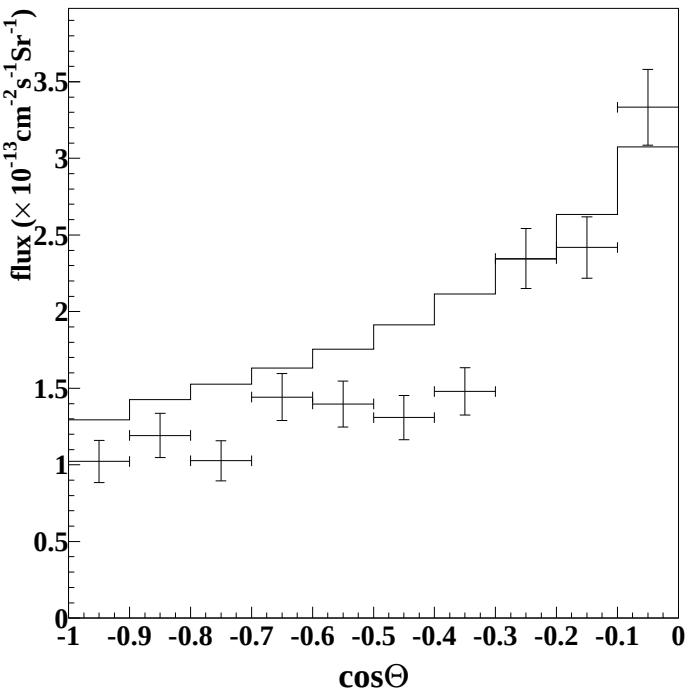

Figure A.1: The zenith angle distribution of the upward through-going muon flux. X axis shows the zenith angle. -1(0) indicates upward-going (horizontal-going). The pluses show the observed flux with the statistical error. The histogram shows the calculated flux based on the Honda flux [13].

A.3 Vertical/horizontal ratio

The calculated flux of the upward through-going muons has $\sim 20\%$ uncertainty mostly due to the uncertainty in the absolute cosmic ray flux. In order to compare the data with the expected flux for both oscillation hypotheses, we use the vertical/horizontal ratio. Taking this ratio, it is possible to carry out the analysis without any large systematic error. Figure A.2 (a) shows the expected flux as a function of the zenith angle for both oscillation hypotheses, and Fig. A.2 (b) shows the oscillation/non-oscillation flux ratio, which is the survival probability of ν_μ. The oscillation parameter I used for this calculation is $\Delta m^2 = 3 \times 10^{-3} eV^2$ with $\sin^2 2\theta = 1$.

Fig A.2 (b) illustrates that the expected flux for $\nu_\mu \rightarrow \nu_s$ is close to that of no-oscillation rather than that of $\nu_\mu \rightarrow \nu_\tau$ oscillation. This is due to the suppression of $\nu_\mu \rightarrow \nu_s$ oscillation by the matter effect. Let us define the events with $\cos\Theta < -0.4 (> -0.4)$ to be $Vertical$-going ($Horizontal$-going). The difference in the oscillation probability between the two hypotheses is remarkable in the $Vertical$-going sample, while the difference in the $Horizontal$-going sample is very small. Therefore we decided to use $Vertical/Horizontal$ ratio for the consistency check of the oscillation mode determination.

The $Vertical/Horizontal$ ratio for data and the calculated flux is:

$$Vertical/Horizontal = \begin{cases} 0.771 \pm 0.049_{(stat.)} \pm 0.007_{(sys.)} & data \\ 0.934 \pm 0.018_{(sys.)} & MC(no\ oscillation) \end{cases} \quad \text{(A.1)}$$

We estimated the systematic error as the following. First, we show the error related to the observed events. Here we considered the background contamination, the event reduction, and the angular correlation. The number of contamination by the cosmic ray muon in this bin is estimated to be 7.4 ± 0.7 events in the most horizontal bin with $\cos\Theta > -0.1$. Thus the uncertainty in the $Vertical/Horizontal$ ratio due to the backgrounds was estimated to be < 0.1 %. The reduction efficiency was estimated from the Monte Carlo study. We applied the reduction program, which is the same as we did for the data, for the Monte Carlo events. The reduction efficiency was slightly lower near the horizontal direction. This effect caused $\pm 0.92\%$ uncertainty in the $Vertical/Horizontal$

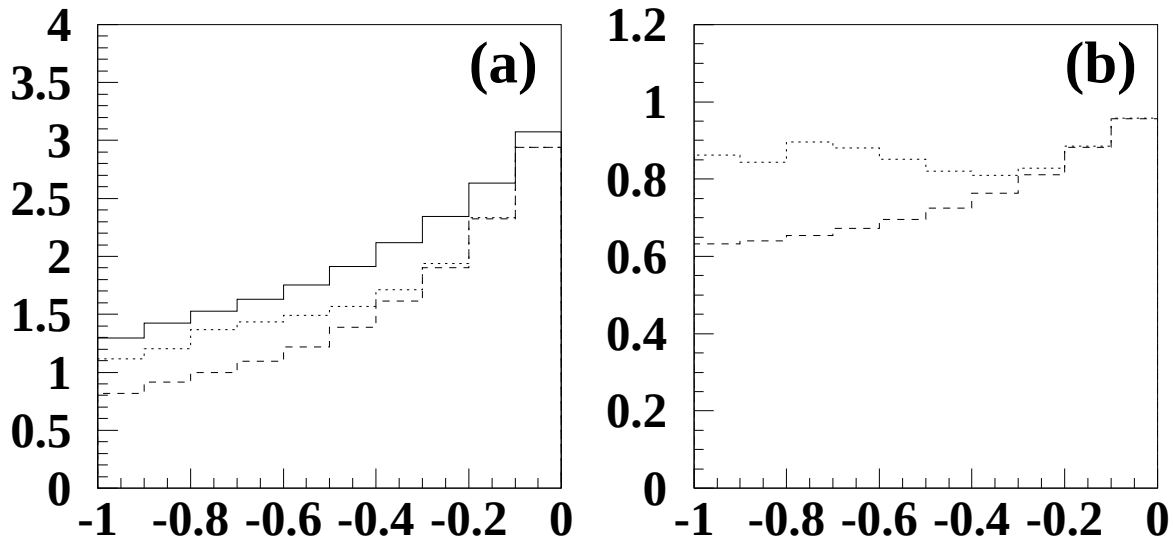

Figure A.2: Figure (a) shows the expected zenith angle distribution of the upward through-going muon flux. The solid line shows the calculated flux without neutrino oscillation. The dashed line shows the expected flux for $\nu_\mu \rightarrow \nu_\tau$ oscillation with $\Delta m^2 = 3 \times 10^{-3} eV^2$ and $\sin^2 2\theta = 1$. The dotted line is for $\nu_\mu \rightarrow \nu_\tau$ oscillation. Both fluxes are based on the Honda flux [13]. Figure (b) shows the survival probability of ν_μ as a function of the zenith angle. The dashed line shows the expected flux for $\nu_\mu \rightarrow \nu_\tau$ oscillation. The dotted line is for $\nu_\mu \rightarrow \nu_\tau$ oscillation. The strange structure of $\nu_\mu \rightarrow \nu_s$ at $\cos\Theta \sim -0.8$ is caused by the effect that the neutrinos passing through the core of the Earth.

ratio. For the through-going muon analysis, we assume that the detected muon direction is same as that of the primary neutrino. However, we need to consider the uncertainty of the angular correlation between the observed muon and that of the primary neutrino, which is resulted from the multiple scattering of muon in the rock and from the angular resolution of the reconstruction method. We estimated this angular correlation to be 4.1°. The error in the ratio due to the angular correlation is estimated to be 0.21%, as we changed the angular correlation. We also considered the time variations of the water transparency and the PMT gains. The errors caused by these variations are negligible.

Next, we discuss the error related to the calculated flux. Although the uncertainty of the absolute flux of the expected flux is canceled by taking the ratio, the uncertainty depending on the zenith angle distribution is not. We considered the K/π ratio, and the structure of the atmosphere as the source of the uncertainty depending on the zenith angle. According to the private communication with Honda, we estimated this error to be 1.5 %. This error is very preliminary, however we adopted this value. Another source is the uncertainty of the energy spectral index of the primary cosmic ray. The higher energy neutrino can be produced in the horizontal direction than in the vertical one, because the decay path length for the vertical-going cosmic-pion in the atmosphere becomes longer than the interaction length with increasing pion energy. Therefore the uncertainty of the energy shape is the source of the systematic error in the Vertical/Horizontal ratio. This error is dependent on the neutrino oscillation, because the oscillation changes with the energy of the neutrino. We estimated this error to be 1.0 %, 0.5 %, and 1.0% for no-oscillation, $\nu_\mu \to \nu_\tau$, and $\nu_\mu \to \nu_s$ oscillation, respectively. The reason of relatively small error for $\nu_\mu \to \nu_\tau$ oscillation is that the energy shape for the vertical-going neutrino is close to that for the horizontal-going one, as the low energy neutrinos disappear due to the neutrino oscillation. Here the oscillation parameter we used for the estimation is $(\Delta m^2, \sin^2 2\theta) = (3 \times 10^{-3} eV^2, 1.0)$, which is the best-fit parameter set by the FC single-ring analysis.

Table A.1 summarizes the systematic errors related to the Vertical/Horizontal ratio.

The expected the *Vertical/Horizontal* ratios for both hypotheses are illustrated in Fig. A.3.

data	background	0.1 %
	detection efficiency	0.21%
	reduction efficiency	0.92%
	the gain of PMT	$\ll 1\%$
	water transparency	$\ll 1\%$
calculated flux	π/K ratio and the atmosphere model	1.5 %
	flux ($Honda \rightarrow Bartol$)	0.5 %
	spectral index	1.0 % (*no oscillation*)

Table A.1: Summary of the systematic error in the $Vertical/Horizontal$ ratio.

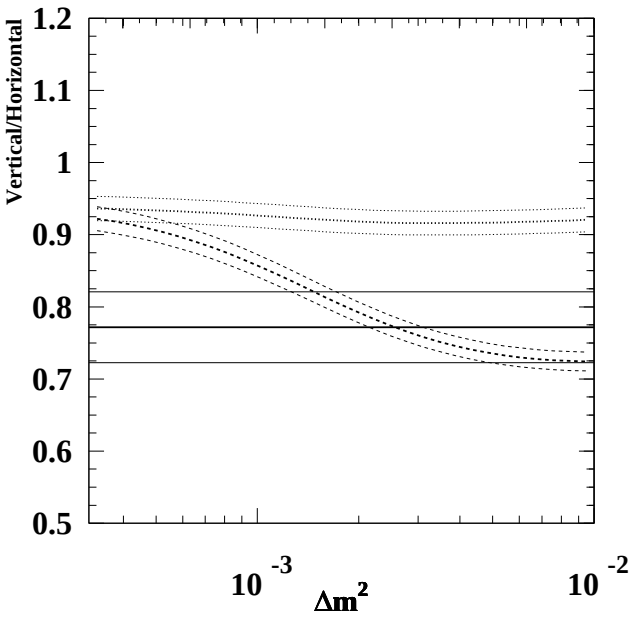

Figure A.3: The expected Vertical/Horizontal ratio as the function of Δm^2 with $\sin^2 2\theta = 1$. Broken (dotted) line shows the ratio for the $\nu_\mu \rightarrow \nu_\tau (\nu_\mu \rightarrow \nu_s)$ oscillation. Solid line illustrates the observed ratio, and thin lines are $\pm$ 1 σ of the data.

A.4 χ^2 analysis

We carried out the consistency check of the through-going muon sample by using a χ^2 test. The definition of the χ^2 is:

$$\chi^2 = \frac{((Vertical/Horizontal)_{data} - (Vertical/Horizontal)_{MC})^2}{\sigma^2_{stat.} + \sigma^2_{sys.}} \tag{A.2}$$

Figure A.4 shows the contour map of the 90 and 99 % C.L. exclusions. χ^2 of $\nu_\mu \to \nu_\tau$ oscillation at the best-fit position of FC single-ring analysis is 0.1/1, and the through-going muon data is in good agreement with the $\nu_\mu \to \nu_\tau$ oscillation hypothesis. On the contrary, χ^2 for $\nu_\mu \to \nu_s$ oscillation hypothesis is 7.45/1, and $\nu_\mu \to \nu_s$ hypothesis is again disfavored at 99 % C.L. there.

A.5 Conclusion of Upward-going muon analysis

The through-going muon data are again consistent with $\nu_\mu \to \nu_\tau$ oscillation, and disfavor $\nu_\mu \to \nu_s$ oscillation at 99 % C.L. at the best fit position obtained by the FC single-ring analysis.

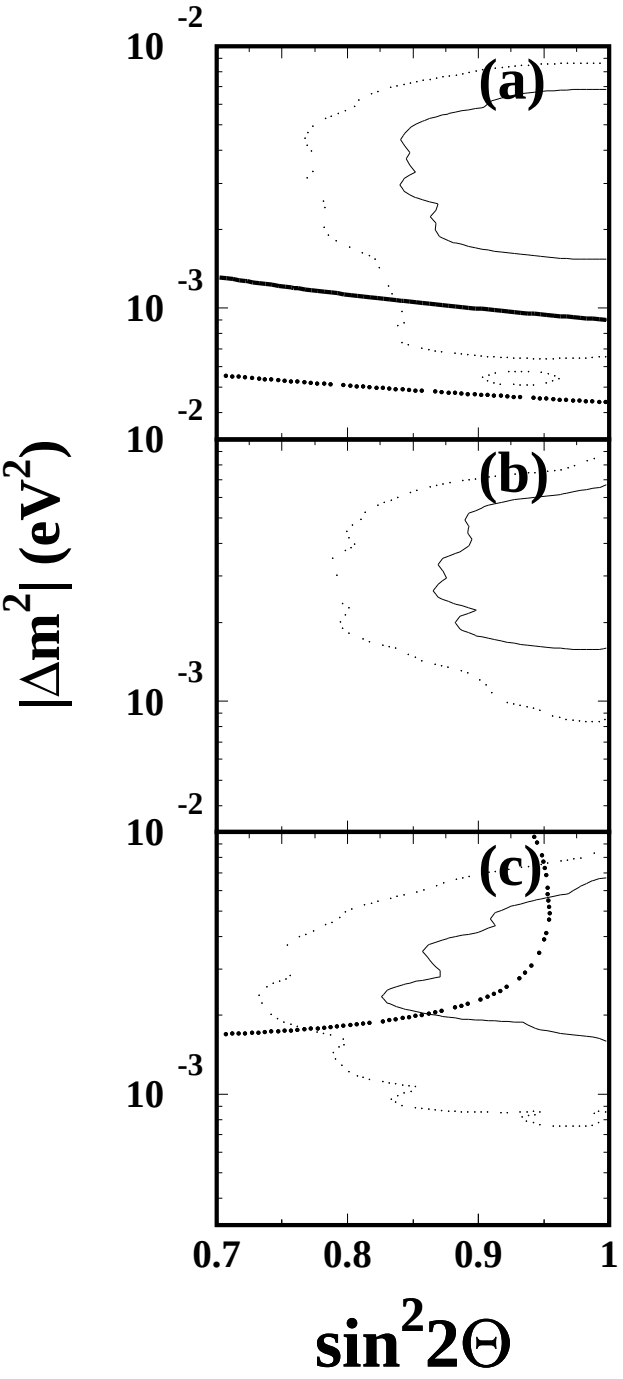

Figure A.4: Contour maps using the *Vertical/Horizontal* ratio of the through-going muons; (a) for $\nu_\mu \to \nu_\tau$, (b) for $\nu_\mu \to \nu_s(\Delta m^2 > 0)$, and (c) for $\nu_\mu \to \nu_s(\Delta m^2 < 0)$. Regions inside the thin solid (dotted) curves show the 90(99)% C.L. allowed parameter regions obtained by the FC single-ring analysis. For $\nu_\mu \to \nu_\tau$ and $\nu_\mu \to \nu_s(\Delta m^2 < 0)$, regions below the thick solid (dashed) curves are excluded at 90(99)% C.L. by the upward through-going muon analysis. For $\nu_\mu \to \nu_s(\Delta m^2 > 0)$, all regions in this figure are excluded at 99% C.L.

Appendix B

π° events

We also used π° events in order to study the event rate of the neutral current events. Generally π° is produced and decay as the following:

$$\begin{aligned} \nu + N \rightarrow \nu + N + \quad & \pi^\circ \\ & \pi^\circ \quad \rightarrow \gamma + \gamma \end{aligned}$$

We can identify the π° events by using the invariant mass using these γs. At the low momentum region of $p_{\pi^\circ} \lesssim 500 MeV/c$, 2 γs from a π° are clearly detected as two e-like rings with a reasonable efficiency. We selected π° by the following criteria:

1. 2 ring events
2. both rings are e-like
3. no electron signal from the decay of μ
4. $90 MeV/c^2 < M_{\gamma\gamma} < 190 MeV/c^2$

where $M_{\gamma\gamma}$ is an invariant mass defined as:

$$M_{\gamma\gamma} = \sqrt{2 p_{\gamma 1} p_{\gamma 2} (1 - \cos\theta_\gamma)} \tag{B.1}$$

where θ_γ is the opening angle between the directions of two rings and p_γ is the reconstructed momentum. The criterion 3 is requested to reject the events containing a muon

or a charged pion. Figure B.1 shows the $M_{\gamma\gamma}$ distribution of the events satisfying above criteria 1,2, and 3. This figure proves that the condition 4 is reasonable.

Figure B.2 shows the relation between the detection efficiency and the momentum of π° . The θ_γ decreases with increasing momentum of π° , therefore it is difficult to identify the high momentum π° as 2 rings events. This is the main reason that the detection efficiency of the π° decreases with the increasing momentum.

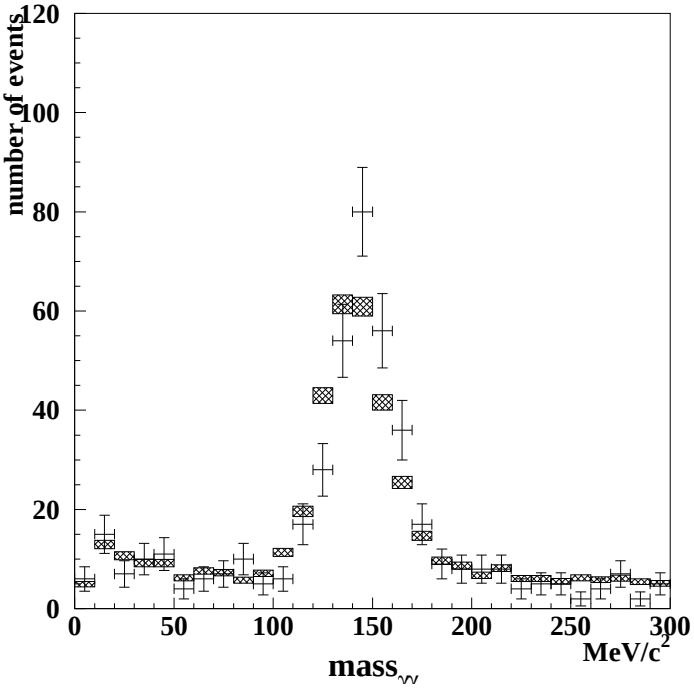

Figure B.1: $M_{\gamma\gamma}$ distribution of the events satisfying 2ring, e-like, and no decay-e cuts. The histograms with the shaded error bars show the Monte Carlo predictions with their statistical error without the neutrino oscillation.

The events satisfying the above criteria are called "π° -like" events. We observed 308 π° -like events, and the expected number from the Monte Carlo study was 294.7 events for the no-oscillation case.

The fraction of each interaction mode in the π° -like sample is summarized in Table B.1. About 80% of these π° -like events were estimated to be due to neutral current events.

B.1 π° event rate

In order to distinguish between $\nu_\mu \rightarrow \nu_\tau$ and $\nu_\mu \rightarrow \nu_s$, we checked the rate of π° -like events. We need to normalize π° -like events by using something produced by the

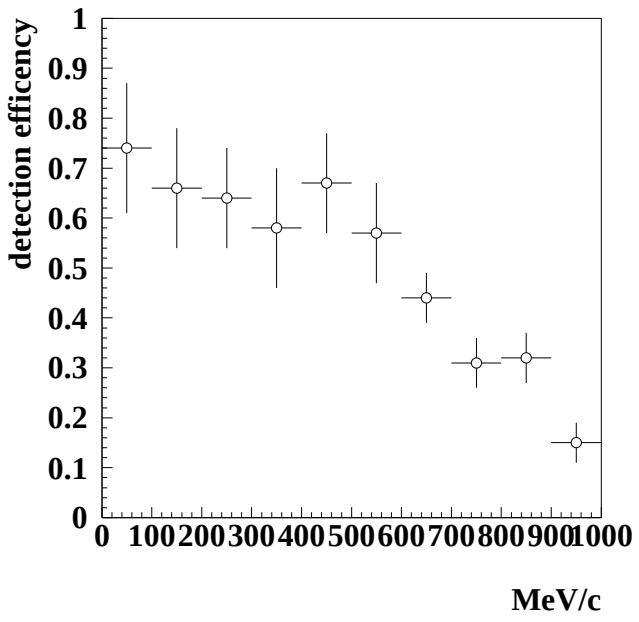

Figure B.2: Detection efficiency of π° as a function of its momentum. At high momentum, the opening angle between 2γ's, into which a π° decays, becomes small. Therefore it is difficult to identify a π° as a 2 rings event. As a result, the detection efficiency of the high momentum π° is lower than that of low momentum π° .

NC	single π°	43.3 %
	coherent π°	20.3 %
	multi π	13.3 %
	others	6.9 %
CC	ν_e	11.1 %
	ν_μ	5.1 %

Table B.1: Fraction of the each interaction mode in the π° sample. CC: charged current interaction; NC: neutral current interaction. Others include NC single $\pi^\pm$ and NC q.e. events. Most of NC single $\pi^\pm$ events identified as π°-like events are due to charge exchange in Oxygen.

atmospheric neutrino interaction to cancel 30 % uncertainty of the absolute flux of the atmospheric neutrinos. Here we used the FC single e-like events for normalization, because the number of e-like events is least affected by neutrino oscillations in the case of these neutrino oscillations modes. We defined a double ratio for the π°/e ratio:

$$R_{\pi^\circ} \equiv (\pi^\circ/e)_{data}/(\pi^\circ/e)_{MC} \tag{B.2}$$

If the $\nu_\mu \to \nu_\tau$ oscillation is the solution of the atmospheric neutrino oscillation, $R_{\pi^\circ} \sim 1$ for any Δm^2. This is because the number of the CC ν_e events and NC events, which are dominant components of e and π° -like samples, are independent of oscillation. On the other hand, in the case of $\nu_\mu \to \nu_s$ oscillation, the number of π° events decreases by ~ 20 % at $\Delta m^2 \sim 5 \times 10^{-3} eV^2$. The R_{π° was obtained as:

$$R_{\pi^\circ} = 1.00 \pm 0.06_{(stat.)} \pm 0.19_{(sys.)} \tag{B.3}$$

R_{π° is just unity, this means the π°/e ratio favors $\nu_\mu \to \nu_\tau$ oscillation. However, the data is consistent with the $\nu_\mu \to \nu_s$ oscillation hypothesis too, because R_{π° unfortunately has the large systematic uncertainty. Figure B.3 shows the expected R_{π° as a function of Δm^2, where we assume $\sin^2 2\theta = 1$. This figure shows that both hypotheses are consistent with R_{π° in all region ($3 \times 10^{-3} < \Delta m^2 < 1 \times 10^{-2}$), which is obtained by the FC single-ring analysis. As the result, we can't discriminate between the two oscillation hypotheses. The dominant systematic error in R_{π° arises from the uncertainty of the neutrino cross section as described below.

B.2 Systematic error in the π° ratio

We checked the systematic error in R_{π° in the same way as we did for R. The main sources of the systematic error are described below.

First, the systematic errors related to the atmospheric neutrino flux are described. The cross section via the neutral current interaction is independent of the neutrino flavors. Thus, the event rates of π° is independent of the uncertainty in the $(\nu_\mu+\bar{\nu_\mu})/(\nu_e+\bar{\nu_e})$ ratio. However, this uncertainty changes the e-like event rates. The systematic error in R_{π° due to the 5 % uncertainty of $(\nu_\mu + \bar{\nu_\mu})/(\nu_e + \bar{\nu_e})$ ratio is estimated to be 1.1%. Similarly, we

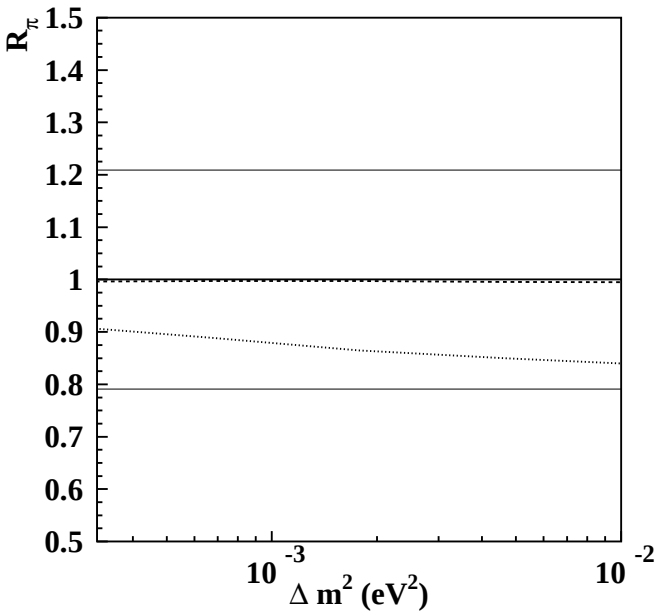

Figure B.3: Expected $R_{\pi\circ}$ as a function of Δm^2 for $\nu_\mu \rightarrow \nu_\tau$ and $\nu_\mu \rightarrow \nu_s$ oscillation. Solid thick line shows for data, solid thin lines are for the $\pm 1\,\sigma$ error of the data, broken line for $\nu_\mu \rightarrow \nu_\tau$, and dotted line for $\nu_\mu \rightarrow \nu_s$.

checked the systematic error arising from uncertainties in $\nu_\mu/\bar{\nu_\mu}$ and $\nu_e/\bar{\nu_e}$. These errors are summarized in Table B.2. The total systematic error related the atmospheric neutrino flux is estimated to be 2.5 %.

	uncertainty	systematic error in $R_{\pi\circ}$
$(\nu_\mu + \bar{\nu_\mu})/(\nu_e + \bar{\nu_e})$	5 %	1.1 %
$\nu_\mu/\bar{\nu_\mu}$	5 %	0.9 %
$\nu_e/\bar{\nu_e}$	10 %	2.0 %

Table B.2: The systematic error in $R_{\pi\circ}$ related to the uncertainty of the atmospheric neutrino flux.

The dominant source of the systematic errors in $R_{\pi\circ}$ is the uncertainty in the neutrino cross sections. The uncertainties of the absolute cross section around $\sim GeV$ region were estimated to be 10 %, 30%, 30%, and 40% for quasi-elastic, single pion, coherent pion, and multi pion interaction, respectively. The uncertainties of the NC/CC ratio were estimated to be 20 % for all interaction modes. The systematic error coming from the uncertainty in the cross section is summarized in table B.3 The total systematic error arising from the uncertainties of the neutrino interactions is estimated to be 15.8 %.

In addition, we independently estimated the systematic error by comparing the π°/e

mode		uncertainty	systematic error in R_{π°
q.e.	CC+NC	10%	6.0%
	NC/CC	20%	$< 0.1\%$
1 pi	CC+NC	30%	9.7%
	NC/CC	20%	7.7%
c pi	CC+NC	30%	4.6%
	NC/CC	20%	3.3%
multi pi	CC+NC	40%	4.4%
	NC/CC	20%	2.9%
total systematic error			15.8%

Table B.3: Systematic error in R_{π° coming from the cross section. q.e : quasi-elastic interaction; 1 pi: single pion interaction; c pi: coherent pion interaction; multi pi: multi pion interaction

ratios calculated by 3 independent neutrino interaction simulations. The maximum difference among these results was 17 %. Accordingly, our estimation of the systematic error is reasonable.

Next we considered the uncertainty related to the nuclear effect. δR_{π° was 7 %, when we changed the mean fully path of the π° in the oxygen nucleus by 50 %. Therefore the systematic error related to the nuclear effect was estimated to be 7%.

The systematic error related to the event reconstruction was estimated by comparing the result of manual scan with the automatic event reconstruction. This comparison resulted the systematic error related to the reconstruction method is 7 %.

Finally, the statistical error of Monte Carlo was 2.2 %. The total systematic error for R_{π° was estimated to be 19 %. Table B.4 summarizes the systematic error for R_{π°.

B.3 The future plan of the R_{π° study

We showed the result of the π°/e ratio, however this study doesn't enable us to discriminate between the two oscillation hypotheses due to the large systematic error. We need

atmospheric neutrino flux		2.5 %
cross section	neutrino interaction	15.8%
	nuclear interaction	7 %
event reconstruction method		7 %
Monte Carlo statistic		2.2%
total systematic error		19 %

Table B.4: Summary of the systematic error of R_{π°

to reduce this systematic error.

From April '99, K2K(KEK to Kamioka) experiment started, which is a long baseline neutrino experiment. In this experiment, 1 kton water Cherenkov tank is used as the front detector. The aim of this detector is to check the behavior of the water Cherenkov detector. The data analysis of this detector is carried out as the same way we do at super-Kamiokande. Obviously, it can detect π° events. Therefore we can reduce the systematic error in the R_{π° by comparing the rate of detected π° and events between the data and the Monte Carlo. K2K experiment uses ν_μ beam so that e-like events are not produced. Therefore the π°/μ ratio is will be studied.

At the 1 kton front detector, ν_μ's emitted for the Super Kamiokande do not oscillate into ν_τ(or ν_s) due to the short neutrino path length. Therefore we can obtain π°/μ ratio without the effect of neutrino oscillation. We can observe so many μ and π° events at 1 kton detector that the statistical error in R_{π° is negligible. In addition, the detection method at K2K is the identical to that of the Super Kamiokande detector, so that the systematic error related to the event reconstruction is almost canceled. There are several minor differences in the π°/μ ratio between the front detector and the Super Kamiokande detector: the difference of the neutrino flavor and the energy distribution of the primary neutrino, and the detection efficiency due to the detector size and so on. However we expect the systematic error in π°/e to go down to $\lesssim 10\%$, and this study will distinguish the two oscillation hypotheses independent of the methods described in this thesis.

Bibliography

[1] W.Pauli, in *Letter open to the participants of the conference in Tubingen*, 1930.

[2] F.Reines and C.L.Cowen, Nature **178**(1956) , 446.

[3] G.Danby *et al.*, Phys. Rev. Lett. **9**(1962) , 36.

[4] T.D.Lee and C.N.Yong, Phys. Rev. **104**(1956) , 254.

[5] C.S.Wu *et al.*, Phys. Rev. **105**(1956) , 1413.

[6] S.L.Glashow, Nucl. Phys. **22**(1961) , 579.

[7] S.Weinberg, Phys. Rev. lett. **19**(1967) , 1264.

[8] A.Salam, in *Elementary Particle Theory, Proc. of the 8th Nobel Symposium*, p. 367, 1968.

[9] T.Yanagida, in *Proc. of the Workshop on the Unified Theory and Baryon number in the Universe*, p. 95, KEK report 79-18(1979).

[10] M.Gell-Mann *et al.*, *Supergravity* , (North Holland, Amsterdam, 1979).

[11] Y.Fukuda *et al.*, Phys. Rev. Lett. **81**(1998) , 1562.

[12] W.R.Webber and J. Lezniak, Astrophys. Space Sci **30**(1974) , 361.

[13] M.Honda *et al.*, Phys. Rev. **D52**(1995) , 4985, Private Commnuication with M.Honda.

[14] V.Agrawal *et al.*, Phys. Rev. **D53**(1995) , 1314, Private Commnuication with T.K.Gaisser.

[15] K. Hirata *et al.*, Phys. Lett. **B205**(1988) , 416.

[16] K.S.Hirata *et al.*, Phys. Lett. **B278**(1992) , 217.

[17] E.W.Beiser *et al.*, Phys. Lett. **B283**(1992) , 446.

[18] Y.Fukuda *et al.*, Phys. Lett. **B335**(1994) , 237.

[19] Y.Fukuda *et al.*, Phys. Lett. **B388**(1996) , 397.

[20] R.Becker-Szendy *et al.*, Phys. Rev. **D46**(1992) , 3720.

[21] R.Clark *et al.*, Phys. Rev. Lett. **79**(1997) , 345.

[22] W.Allison *et al.*, Phys. Lett. **B391**(1997) , 491.

[23] M.Aglietta *et al.*, Europhys. Lett. **8**(1996) , 1989.

[24] K.Daum *et al.*, Z.Phys. **B391**(1997) , 611.

[25] Y.Fukuda *et al.*, Phys. Lett. **B436**(1999) , 33.

[26] B.Pontecorvo, Sov. Phys. JETP. **6** (1957) , 429.

[27] Z.Maki *et al.*, Prog. Theor. Phys. **28** (1962) , 870.

[28] CHOOZ, M. Apollonio *et al.*, Phys. Lett. **B420**, 397 (1998),

[29] LSND, C. Athanassopoulos *et al.*, Phys. Rev. Lett. **77**, 3082 (1996),

[30] LSND, C. Athanassopoulos *et al.*, Phys. Rev. **C58**, 2489 (1998),

[31] K.Eitel and B.Zeitnitz, Nucl. Phys. Proc. Suppl. **77**(1999) , 212.

[32] B.T.Cleveland *et al.*, Astrophys. J. **496**(1998) , 505.

[33] W.Hampel *et al.*, Phys. Lett. B **447**(1999) , 127.

[34] J.M.Abdurashitovv *et al.*, Phys. Rev. Lett. **77**(1996) , 4708.

[35] Y.Fukuda *et al.*, Phys. Rev. Lett. **82**(1999) , 1810.

[36] L.Wolfenstein, Phys. Rev. **D17**(1978) , 2369.

[37] S.P.Mikheyev and A.Yu.Smirnov, Yad. Fiz. **42**(1985) , 1441.

[38] S.P.Mikheyev and A.Yu.Smirnov, Nouvo Cim. **9C**(1986) , 17.

[39] D.Notzold and G.Raffelt, Nucl. Phys. **B307**(1988) , 924.

[40] K.Enqvist *et al.*, Nucl. Phys. **B349**(1991) , 754.

[41] D.L.Anderson, *Theory of the Earth* (Blackwell scientific publicatons, 1989).

[42] M.Srednicki, Phys. Rev. **D54**(1996) , 116.

[43] R.E.Lopez *et al.*, Phys. Rev. Lett **82**(1999) , 3952.

[44] The CHORUS Collaboration, nucl-ex 9907015.

[45] J.J.Gomez-Cadenas, in *Neutrino'98*, 1998.

[46] H.Burkhardt and J.Steinberger, Ann. Rev. Nucl. Part. Sci **41**(1991) , 55.

[47] D.Schrmm and M.Turner, Phys. Mod. Phys. **70**(1998) , 303.

[48] A.Dolgov *et al.*, Sov. J. Nucl. Phys. **33**(1981) , 700.

[49] R.Barbieri and A.Dolgov, Phys. Lett. **B237**(1990) , 440.

[50] R.Barbieri and A.Dolgov, Nucl. Phys. **B349**(1991) , 743.

[51] K.Enqvist, K.Kainulainen, and M.Thomson, Phys. Rev. **D68**(1992) , 744.

[52] K.Enqvist, K.Kainulainen, and M.Thomson, Nucl. Phys. **B373**(1992) , 498.

[53] J.Cline, Phys. Rev. Lett. **68**(1992) , 3137.

[54] X.Shi, D.N.Sscramm, and B.B.Fields, Phys. Rev. **D48**(1993) , 2568.

[55] R.Foot and R.R.Volkas, Phys. Rev. **D56**(1997) , 6653.

[56] A.Geiser, hep-ph/9901433.

[57] F.Vissani and A. Smirov, Phys. Lett. B **432**(1998) , 376.

[58] L.J.Hall and H.Murayama, Phys. Lett. B **436**(1998) , 323.

[59] P. Lipari and M. Lusignoli, Phys. Rev. **D58**(1998) , 73005.

[60] Q.Y.Liu and A. Smirov, Nucl. Phys. **B524**(1998) , 505.

[61] Q.Y.Liu and A. Smirov, Phys.Lett. **B440**(1998) , 319.

[62] H.Kume *et al.*, Nucl. Instr. and Meth., **205**(1983) , 443.

[63] A.Suzuki *et al.*, Nucl. Instr. Meth., **A329**(1993) , 299.

[64] H.Ikeda *et al.*, Nucl. Instr. Meth., **A320**(1992) , 310.

[65] P.Hanggi *et al.*, Phys. Lett. **B51**(1974) , 119.

[66] M.Nakahata *et al.*, Nucl. Instr. Meth. **A421**(1999) , 113.

[67] M.Nakahata *et al.*, J. Phys. Soc. Jpn. **55**(1986) , 3786.

[68] A.Hasegawa, Master's thesis, Tohoku University, 1997.

[69] C. H. L. Smith, Phys. Rept. **3**, 261 (1972),

[70] H.J.Grabosch *et al.*, Z. Phys. Rep. **3C**(1989) , 527.

[71] S.J.Barish *et al.*, Phys. Rev. **D16**(1977) , 3103.

[72] S. Bonetti *et al.*, Nuovo Cim. **38A**, 260 (1977),

[73] S.V.Belikov *et al.*, Z. Phys. **A320**(1985) , 625.

[74] A.S.Vovenko *et al.*, Yad. Fiz. **30**(1979) , 1014.

[75] C.H.Albright *et al.*, Phys. ReV. **D14**(1976) , 1780.

[76] L. A. Ahrens *et al.*, Phys. Rev. Lett. **56**, 1107 (1986),

[77] D.Rein, Z. Phys. **C35**(1987) , 43.

[78] G.M.Radecly *et al.*, Phy. Rev. **D25**(1982) , 1161.

[79] M.Hirata *et al.*, Ann. Ry. (N.Y.) **108**(1977) , 116.

[80] S.Adler, Phys. Rev. **B135**(1964) , 963.

[81] C. Piketty and L. Stodolsky, Nucl. Phys. **B15**(1970) , 571.

[82] D.Rein and L.M.Shegal, Nucl. Phys. Bwwe(1983) , 29.

[83] P.Marage *et al.*, Z. Phys. **C31**(1986) , 191.

[84] CERN-HERA 79-01 (1979).

[85] M. Gluck, E. Reya, and A. Vogt, Z. Phys. **C67**, 433 (1995),

[86] P. Messet and J.-P. Vaille, Phys. Rep. **C39**(1978) , 1.

[87] J.E.Kim *et al.*, Rev. Mod. Phys. **53**(1981) , 211.

[88] H.Sarikko, Neutrino 1979 , 507.

[89] S.Barlag *et al.*, Z. Phys. **C31**(1982) , 283.

[90] T.Sjostrand, CERN-TH.7112/93 W5035/W5044.

[91] T.Eichten *et al.*, Phys. Lett. **46B**(1973) , 274.

[92] S.Ciampolillo *et al.*, Phys. Lett. **84B**(1979) , 281.

[93] J.G.Morfin *et al.*, Phys. Lett. **84B**(1981) , 235.

[94] D.S.Baranov *et al.*, Phys. Lett. **81B**(1979) , 255.

[95] D.C.Colley *et al.*, Z. Phys. **C2**(1979) , 187.

[96] A.S.Vovenko *et al.*, Yad. Fiz. **30**(1979) , 1014.

[97] V.N.Anikeev *et al.*, Z. Phys. **C70**(1996) , 39.

[98] L.L.Salcedo *et al.*, Nucl. Phys. **A484**(1988) , 557, Private Commnuication with H.Toki.

[99] G.Rowe *et al.*, Phys. Rev. **C18**(1978) , 584.

[100] D.Asher *et al.*, Phys. Rev. **C23**(1981) , 2173.

[101] C.H.Q.Ingram *et al.*, Phys. Rev. **C27**(1983) , 1578.

[102] T.A.Gabriel *et al.*, IEEE Trans. Nulc. Sci **36**(1989) , 14.

[103] J.Arends *et al.*, Nucl. Rev. Lett. **A526**(1991) , 479.

[104] T.Fujii *et al.*, Nucl. Phys. **B120**(1977) , 395.

[105] CERN Program Library Report No., 1993 (unpublished).

[106] T.A.Gabrel *et al.*, in *Detector research and development for the Superconduction SuperCollider*, p. 608, 1990.

[107] E.Bracci *et al.*, CERN/HERA 72-1(1972) .

[108] A.S.Carrol *et al.*, Phys. Rev. **C14**(1977) , 635.

[109] E.Eichler *et al.*, JADE-Note **65**(1980) .

[110] S.Hatakeyama, PhD thesis, Tohoku University, 1998.